Quasi-Static, Cyclic, and Fracture Characteristics of Plasma Transferred Wire Arc (PTWA) Thermal Sprayed AlSi Cylinder Bores

by

Jessica Zhang

A thesis
presented to the University of Waterloo
in fulfillment of the
thesis requirement for the degree of
Master of Applied Science
in
Mechanical and Mechatronics Engineering

Waterloo, Ontario, Canada, 2022

Author's Declaration

This thesis consists of material all of which I authored or co-authored: see Statement of Contributions included in the thesis. This is a true copy of the thesis, including any required final revisions, as accepted by my examiners.

I understand that my thesis may be made electronically available to the public.

Statement of Contributions

The research detailed in this thesis was supported by Natural Sciences and Engineering Research Council of Canada (NSERC) with contributions from Stellantis (previously Fiat Chrysler Automobiles (FCA)) under grant CRDPJ 536219-18. Furthermore, the content presented partially in Chapters 3 and 4 have been taken from a manuscript which has been published. The candidate is the primary author of the manuscript and was responsible directly in data collection or coordinating it, as well as analysis of results. A number of individuals have contributed to the current work (including the published manuscript) and are detailed below:

Prof. Hamid Jahed: supervised and mentored all work and provided technical and editorial feedback for both the manuscript (published and future) and the thesis document.

Dr. Dulal Saha: acted to provide both technical and editorial feedback in the preparation of the individual manuscript in Chapters 3 and 4, as well as manuscripts to be published in the future. He also conducted the work involving the TEM/FIB analysis, residual stress analysis using the XRD, and SEM analysis of fracture mechanisms for all bending work (i.e., quasi-static and bending) with his expertise in these areas.

Dr. Seyed Behzad Behravesh: provided training and support for experimental work including adhesion and 3 point bending, as well as guidance on finite element method analysis via ABAQUS.

Stellantis (Jim Chen, Martin Kramer, Yi Liu, Gianni Lamonaca, Marie Mills, Dean Weed) and Comau (Andrea Muzio, Paulo Rosa): acted as a source of guidance for the research and development of the project, lending their expertise of the industry standards and the application towards the engine system.

Abstract

This study examines the microstructure and mechanical properties of plasma transferred wire arc (PTWA) coating of typical alloyed steel, deposited on diecast aluminum alloy cylinder bores. The coating surface and microstructure were characterized in terms of surface roughness, features (i.e., defects, splats formation mechanisms, distribution of oxides, re-solidified particles, and interfacial metallurgical bonding) using laser scanning confocal microscope, scanning and transmission electron microscope (SEM and TEM). Residual stress through the thickness of the coating was measured using x-ray diffraction (XRD) and hole-drilling method. In post-processed samples, compressive residual stress was measured throughout the coating with a value close to 100 MPa at the interface, resulting from the thermal mismatch between coating and substrate materials. In terms of mechanical properties, coating hardness was estimated at both the micro- and nanoscale and examined the influence of microstructure inhomogeneity on the mechanical performance and failure modes.

The PTWA coating of typical alloyed steel deposited on diecast aluminum alloy cylinder bores is investigated via experimental pull tests for three types of samples of varying interface pattern and/or substrate material and finite element model (FEM) simulations. FEM simulations account for the portion of adhesion attributed to solely mechanical interlocking, whereas the experimental results rely on the adhesion at the interface due to mechanical interlocking, potential metallurgical bonding, and/or other factors at play. Experimental results show that differences in interface pattern and/or substrate material will result in varying degrees of adhesion failure at the interface and cohesion failure within the sprayed coating itself. The average bonding strength across the three types of samples was found to be 37.59, 27.55, and 33.15 MPa (for D319, W319, and W356 sample types).

Monotonic three-point bending tests of curved samples extracted from trial cylinder bores and consequent analysis using the equivalent section method yielded stress-strain properties for both the substrate and coating materials. SEM observation of fracture surfaces showed three modes of failure involving coating delamination and breakage, which is related to the deposition process and the various features within the coating. Further bending tests of flat samples were performed for four combinations of interface pattern orientation and substrate material. Bending tests were conducted at three temperatures within an environmental chamber (room temperature, 100°C, and 250°C) to simulate the relevant thermal conditions within the engine during operation. Results show that differences in interface pattern and/or substrate material will result in differing failure mechanisms and strengths as well as the trends associated with increasing operating temperatures. It was found that the A356 substrate generally performed better than the corresponding A319, and the samples with dovetail rows running along the length were stronger than the opposing orientation.

Cyclic three-point bending tests were performed for four combinations of interface pattern orientation and substrate material. The Basquin parameters were obtained for all twelve combinations of substrate, orientation, and temperature. The fatigue strength predicted by Basquin parameters are more conservative compared to what is seen in experimental data. Results show that differences in the interface pattern and/or substrate material will result in differing failure mechanisms and fatigue properties, as well as trends associated with increasing temperatures. It was found that the A356 substrate generally performed better than the corresponding A319 and the dominating failure mechanism was specific to the sample orientation (i.e., delamination and interlock breakage/separation). An increase in temperature is generally associated with reduced fatigue properties and increased delamination/separation due to the thermal coefficient mismatch during expansion between the coating and substrate materials. Overall, it was found that the combination of A356 substrate in the H-orientation with the interfacial wave pattern surface activation is a candidate with high potential towards the application of cylinder bores.

Acknowledgements

I would like to acknowledge the support I received from the members of our research group for the valuable discussions and support. The ongoing small remarks and suggestions made in passing by most of my colleagues were exceedingly helpful in both my experimental work and analysis. I am very thankful for all those who had a part in what I have accomplished in my thesis and during my degree.

I have had the privilege of working with my supervisor, Professor Hamid Jahed – without his distinct impression on me during an undergraduate course, I would not have found myself looking up his research group, discovering my interest in research, or even considering graduate studies in applied science. His passion and involvement throughout both my undergraduate and graduate degrees have been motivating and inspiring. I have always been especially grateful for his discussions, which were always very concise and how he made difficult concepts easy to understand.

Dulal Saha started working on this project immediately after he joined our research group and has provided invaluable advice and direction. Sometimes the smallest setbacks are the most frustrating, and he was an unceasing support in providing his practical knowledge. He also lent his expertise to the SEM/TEM analysis. Seyed Behzad Behravesh has been especially involved in my experimental growth in research, training me on several pieces of equipment in the laboratory, collaborating on test plans and methods, as well as always ensuring experiments were being executed smoothly and safely. His detailed and thorough support finite element analysis is greatly appreciated. Lastly, Bahareh Marzbanrad trained me for hole drilling tests and analysis, and Kevin Musselman and Marco Alfano contributed significantly to the completion of this thesis document with their valuable feedback.

I would like to acknowledge the support of the Natural Sciences and Engineering Research Council of Canada (NSERC) Collaborative and Development with contributions from Stellantis (previously Fiat Chrysler Automobiles, FCA) under grant CRDPJ 536219-18. I thank Dr. Yi Liu, Martin Kramer, Dr. Jim Chen, Gianni Lamonaca, Marie Mills, and Dean Weed of Stellantis, and Andrea Muzio and Paulo Rosa from Comau, for the highly constructive discussions and valuable suggestions.

Finally, I would like to acknowledge the support of my family and friends who have always challenged me and remained confident in my abilities. This was especially appreciated for the completion of my thesis work during the time of the pandemic.

Table of Contents

Author's Declaration ii

Statement of Contributions iii

Abstract iv

Acknowledgements vi

List of Figures x

List of Tables xvi

Chapter 1 Introduction 1

1.1 Motivation 1

1.2 Objectives 2

1.3 Thesis Overview 2

Chapter 2 Background and Literature Review 5

2.1 Thermal Spray Coatings 5

2.2 PTWA Spray 7

2.3 Microstructure 10

2.4 Residual Stress 12

2.5 Hardness and Bonding Strength 14

2.6 Quasi-Static and Fatigue Properties 15

Chapter 3 Materials and Experimental Methods 18

3.1 Coating Characterization Samples and Methods 18

3.2 Interface Characterization Samples and Methods 20

3.3 Surface Roughness Samples and Methods 20

3.4 Residual Stress Samples and Methods 21

3.5 Coating Hardness Samples and Methods 22

3.6 Adhesion Testing Samples and Methods 23
    3.6.1 Adhesion Test Setup 25
    3.6.2 Adhesion Simulation 28
3.7 Quasi-Static Bending Samples and Methods for Curved Cylinder Specimen 29
3.8 Quasi-Static and Cyclic Bending Samples and Methods for Flat Plate Specimen 30
    3.8.1 Bending Samples 30
    3.8.2 Bending Experimental Methods 35
    3.8.3 Bending Analysis 38
Chapter 4 Characterization of PTWA Coating on Cylinder Bores 39
4.1 Coating Characterization 40
    4.1.1 Splat Structure 41
    4.1.2 Resolidified Particles and Pores 42
    4.1.3 Oxides 45
4.2 Interface Characterization 45
4.3 Surface Roughness 47
4.4 Residual Stress 48
4.5 Coating Hardness 51
Chapter 5 Adhesion Properties of PTWA Coating 54
5.1 Experimental Bonding Strength 54
5.2 Coating Strength Simulation 58
5.3 Fracture Mechanisms 61
Chapter 6 Quasi-Static Characteristics of PTWA Coating at Room and High Temperatures 72
6.1 Quasi-Static Properties of Cylinder Samples at Room Temperature 72
    6.1.1 Quasi-Static Properties of Cylinder Samples 72

6.1.2 Quasi-Static Fracture Mechanisms of Cylinder Samples 72

6.2 Quasi-Static Properties of Flat Samples at Room and High Temperatures 77

6.2.1 Quasi-Static Properties of Flat Samples 77

6.2.2 Quasi-Static Failure Mechanisms of Flat Samples 81

Chapter 7 Fatigue Behaviour and Fracture Mechanisms of PTWA Coating at Room and High Temperatures 86

7.1 Fatigue Properties 86

7.2 Fatigue Failure Mechanisms 92

Chapter 8 Conclusions 98

8.1 Concluding Statements 98

8.1.1 Microstructural Characterization Conclusions 98

8.1.2 Bonding (Adhesion/Cohesion) Property Conclusions 98

8.1.3 Quasi-Static Bending Conclusions 99

8.1.4 Fatigue Bending Conclusions 101

8.2 Future Research 102

Letter of Copyright Permission 104

References 105

Appendix A Anton Paar Data 110

List of Figures

Fig. 1 Formation of thermal sprayed coating highlighting three areas of interest in microstructural analysis: coating (red), interface (yellow), and substrate near interface (white) [7]. 5

Fig. 2 Picture of PTWA system (left) and a schematic of the PTWA process (right) [4]. 7

Fig. 3 Geometry of dovetail profile surface activation pattern [17]. 9

Fig. 4 Mises stress during/after deformation for 10 um peak width, 200 um peak height, 15 um crush and different profile parameters (a), (b), and (c) with FEA shape predictions [18]. 10

Fig. 5 Thorough-thickness residual stress distribution for four high RS specimens (WC-Co on 6061 Al with high compressive residual stress in coating) [29]. 13

Fig. 6 As-sprayed, diahon, and machined cylindrical sleeves with PTWA coating. 19

Fig. 7 Cross-sectional Backscattered-Electron (BSE) SEM image of dovetail profile with inset cut sample location along (a) longitudinal direction, and (b) circumferential direction. 20

Fig. 8 Experimental set-up for RS measurements using (a) XRD method, and (b) hole drilling method. 22

Fig. 9 Micrographs of two interface patterns showing (a) dovetail pattern with as-deposited coating, (b) dovetail pattern geometry, (c) wave pattern with as-deposited coating, and (d) close-up of wave pattern. 25

Fig. 10 Coupon samples (a) as-received and before machining, and (b) post-machining to smooth the coating surface, and adhesion testing (c) setup, and (d) coupon geometry with threaded hole. 26

Fig. 11 Alignment fixture for adhesive curing. 27

Fig. 12 Basis of the three finite-element models: (a) dovetail drawing, (b) wave drawing, and (c) wave SEM image. Perspective view of models for (d) dovetail drawing, (e) wave drawing, and (f) wave SEM image. Perspective view of stress distribution for models based on (g) dovetail drawing, (h) wave drawing, and (i) wave SEM. Two-dimensional separation view for models of (j) dovetail drawing, (k) wave drawing, and (l) wave SEM image. Boundary conditions are shown for the (m) Applied displacement is shown at the (m) top face and boundary conditions are shown for the (n) bottom face. 28

Fig. 13 SEM images of the interface region with wave pattern that was cut into the substrate at the bottom showing (a) as-deposited coating, and (b) after machining to smooth the coating surface...... 31

Fig. 14 Photograph of bending samples at various stages of preparation: (a) as-deposited coating, (b) machining shown in Fig. 13(b), (c) final product after grinding, and (d) sample extracted from coated cylinder bores. 31

Fig. 15 Coating surface of cylinder bore samples using (a) SEM and (b) scanning optical microscope. 32

Fig. 16 SEM images of the coating surface of (a) cylinder bore samples, (b) bending samples grinded to 800-grit, and (c) bending samples grinded to 1200-grit. 32

Fig. 17 Schematic with coating side indicated in red showing (a) bending specimen dimensions (b) three-point bending loading diagram, and (c) the two bending sample orientations extracted perpendicular to each other from the flat plates where the W-orientation shows the wave pattern on the long edge and the H-orientation with the pattern on the short edge and rows of wave that run vertically. 33

Fig. 18 Diagram of extraction from flat coated plates at two orientations: (a) W-orientation and (b) H-orientation. 34

Fig. 19 Speckled samples for strain measurements in quasi-static tests and white samples without for crack initiation detection in cyclic tests 35

Fig. 20 Test plan showing the twelve combinations of the two substrates, two orientations, and three temperature conditions. 37

Fig. 21 MTS test setup for quasi-static elevated temperature testing including three-point bending fixture installed within the environmental chamber. The DIC device cameras are required to operate outside the chamber and through the chamber's glass window. 37

Fig. 22 J. Zhang, D.C. Saha, H. Jahed, Microstructure and mechanical properties of plasma transferred wire arc spray coating on aluminum cylinder bores, Surf. Coatings Technol. 426 (2021) 127757 [45]. 39

Fig. 23 BSE SEM microstructural images showing (a) the coating cross-section and (b) the same image with various features and defects outlined. 40

Fig. 24 BSE SEM microstructural images of coating cross-section showing various features and defects such as (a) coating penetration into the substrate, (b) pores/voids, (c) inter-splats gap and boundary oxides, and (d) oxides and re-solidified particles. 41

Fig. 25 BSE SEM image of as-deposited coating, showing three different splats formation regions. . 42

Fig. 26 Optical images showing the morphology and locations of the (a) re-solidified particles, (b) voids, and (c) the size range distribution of re-solidified particles.. 44

Fig. 27 (a) Interface selection for TEM membrane preparation using FIB method, (b) bright-field TEM image of steel coating and Al substrate interface, and (c) enlarged view of the rectangular area on (b). 46

Fig. 28 Bright-field TEM image of the interface with EDX elemental mapping of Fe, Al, Cr, O, and Si.. 47

Fig. 29 EDX line scanning across the steel coating and Al substrate interface................................. 47

Fig. 30 Comparison of as-deposited, diahon, and machined samples in terms of (a) surface roughness, (b) average surface roughness (R_a), (c) difference between tallest peaks and deepest valleys at the surface (R_z), and (d) trace of surface roughness line profiles excluding large pores. 48

Fig. 31 XRD residual stress distribution across the machined and diahon coatings. 49

Fig. 32 XRD residual stress distribution across the as-deposited coating. 49

Fig. 33 Residual stress distribution across the coatings using hole-drilling method and XRD methods, and substrate using hole-drilling for machined and diahon samples.. 51

Fig. 34 Vickers micro-hardness distribution across the coating thickness of the post-processed samples. 52

Fig. 35 Comparison of micro- and nano-hardness ranges on oxide, oxide/splat, and splat regions..... 53

Fig. 36 Camera images comparing the fracture surfaces of (a) D319-03, (b) D319-04, (c) W319-09, and (d) W356-13. 55

Fig. 37 SEM images at x50 magnification comparing the fracture surfaces of (a) D319-03, (b) D319-04, (c) W319-09, and (d) W356-13, with examples of coating remains highlighted. 56

Fig. 38 SEM images comparing the side cross sectional view of (a) D319-03, (b) D319-04, (c) W319-09, and (d) W356-13, with examples of coating remains indicated in yellow. 56

Fig. 39 SEM images highlighting the degrees of mechanical deformation of (a) dovetail, and (b) wave interface patterns. 57

Fig. 40 EDX elemental analysis of the textured regions showing Fe, Al, Si, and O distribution. 58

Fig. 41 Plots showing (a) stress versus separation curve for dovetail drawing (red) and wave SEM (blue) models, and (b) parametric study where the static friction coefficient is varied. 59

Fig. 42 Cross-sectional SEM image comparison with (a) dovetail model, (b) wave model, and (c) fracture face SEM image showing the orientation of cross-sectional image AA’.............................. 60

Fig. 43 SEM images with experimental breakage highlighted in yellow for (a) dovetail and (b) wave patterns. 60
Fig. 44 Dovetail pattern model with expected coating breakage regions highlighted in yellow dashes, and location of embedded coating on substrate highlighted in white dots for (a) complete side view, (b) separate fracture surface view, and (c) separate side view. 61
Fig. 45 Wave pattern model with expected coating breakage regions highlighted in yellow dashes, and location of embedded coating on substrate highlighted in white dots for (a) complete side view, (b) separate fracture surface view, and (c) separate side view. 62
Fig. 46 Wave pattern (a) model showing expected breakage paths, and (b) SEM image of test sample with various breakage identified: breakage at interface (green dash-dotted line), breakage within coating while close to the interface (white dotted line), and breakage within the coating while further from the interface (yellow dashed line). 63
Fig. 47 Wave model stress concentration (a) locations in coating (red) and substrate (orange), and (b) stress concentration plotted with separation. 65
Fig. 48 Dovetail model stress concentration (a) locations in coating (red), and (b) stress concentration plotted with separation. 66
Fig. 49 SEM images showing common locations of (a) voids and (b) resolidified particles. Model representations of (c) particle inclusions and (d) void feature. Simulations showing the (e) original dovetail model, (f) model with particles, and (g) model with void. 69
Fig. 50 Simulations showing the substrate side of the (a) original dovetail model, (b) model with particles, and (c) model with void. The simulations are also shown for the coating side of the (d) original dovetail model, (e) model with particles, and (f) model with void. 70
Fig. 51 Various models plotted against separation showing (a) pull strength, and (b) stress values at concentrated locations in the substrate. 71
Fig. 52 Three-point bending tests using DIC and video camera system showing (a) the sample before failure, (b) the sample at the time of failure, (c) strain distribution along x-direction before failure, (d) strain distribution along x-direction at the time of failure, (e) side view of the fracture location, and (f) bottom view of the fracture location. 73
Fig. 53 Monotonic three-point bend test results showing (a) transformed bending stress vs. strain curves at three different locations (coating surface, interface at coating side, and interface at substrate side), and (b) maximum bending stress across six samples at three different locations. 74

Fig. 54 Detailed view of the fracture surface on both Al substrate and steel coating sides. 76
Fig. 55 The three-point bend test results showing (a) a schematic of three different failure modes identified in the fractured samples, (b) a plot of failure load as a function of fracture modes; and SEM micrographs of each mode of fracture. 77
Fig. 56 True stress strain curves of RT quasi-static bending testing with A319-W in orange, A319-H in blue, A356-W in yellow, and A356-H in green at (a) RT, (b) 100°C, and (c) 250°C. 80
Fig. 57 Stress strain plot comparing the effects of three temperatures for (a) A319-W, (b) A319-H, (c) A356-W, and (d) A356-H. 81
Fig. 58 SEM images of the RT fracture surfaces with the coating, region where interlock occurs (interface pattern height), and substrate for (a) A319-W, (b) A319-H, (c) A356-W, and (d) A356-H specimen. 83
Fig. 59 SEM images of the RT fracture surfaces in the W-orientation showing (a) breakage in the A319-W pattern, (b) coating cohesion failure in A319-W, (c) coating cohesion failure in A356-W, and (d) interlock damage in A356-W specimen. 84
Fig. 60 SEM images of the RT fracture surfaces in the H-orientation showing (a) coating cohesion failure in A319-H, (b) delamination in A319-W, (c) delamination in A356-W, and (d) coating cohesion failure in A356-W specimen. 84
Fig. 61 Fracture surface SEM images of (a) A356-W at 100°C, (b) A356-H at 100°C, (c) A356-W at 250°C, and (d) A356-H at 250°C. 85
Fig. 62 S-N (stress amplitude and coating life) curves showing the RT, 100°C, and 250°C results for (a) A319-W, (b) A319-H, (c) A356-W, and (d) A356-H. 87
Fig. 63 Plots of A356-W RT sample results showing (a) the S-N (stress amplitude and coating life) curve with uncorrected ($R = 0.1$) and Morrow/SWT corrected values ($R = 1$), and (b) the linear relationship between the equivalent stress amplitude for fully reversed loading and coating cycles to failure on a log-log scale for both Morrow and SWT correction methods. 88
Fig. 64 S-N curves predicted by the Basquin equations showing the RT, 100°C, and 250°C results for (a) A319-W, (b) A319-H, (c) A356-W, and (d) A356-H. Specimen in experimental cyclic tests that reached runout at 1,000,000 cycles are included in the plots. 90
Fig. 65 Low-cycle fracture surface images of A356 substrate samples in the W-orientation at (a) RT (25,600 cycles), (b) 100°C (26,460 cycles), and (c) 250°C (25,300 cycles). 94

Fig. 66 High-cycle fracture surface images of A356 substrate samples in the W-orientation at (a) RT (209,200 cycles), (b) 100°C (164,000 cycles), and (c) 250°C (192,000 cycles). 94

Fig. 67 Low-cycle fracture surface SEM images of A356 substrate samples in the H-orientation at (a) RT (10,050 cycles), (b) 100°C (7,850 cycles), and (c) 250°C (12,800 cycles). 95

Fig. 68 High-cycle fracture surface SEM images of A356 substrate samples in the H-orientation at (a) 100°C (96,320 cycles) and (b) 250°C (163,950 cycles). 96

Fig. 69 Close-up SEM images of low-cycle fracture (25,300 cycles) surface of A356 substrate samples in the W-orientation at 250°C showing (a) the degree of coating/substrate interfacial separation, and (b) fatigue microcracks on the wave pattern wall surfaces. 96

Fig. 70 Close-up SEM images of low-cycle fracture (12,800 cycles) surface of A356 substrate samples in the H-orientation at 250°C showing (a) the degree of coating/substrate interfacial separation and pattern deformation, and (b) breakage through pattern rows and the ductile nature of the substrate. 97

Fig. 71 Close-up SEM images of high-cycle (163,950 cycles) fracture surface of A356 substrate samples in the H-orientation at 250°C showing (a) the degree of coating/substrate interfacial separation and pattern deformation, and (b) the ductile nature of the substrate. 97

List of Tables

Table 1 Comparison of thermal spray processes for coating deposition in engine cylinder bores [10] . 6
Table 2 Chemical composition of the materials used in this investigation (in wt.%). 18
Table 3 Chemical composition of the materials used in this investigation (in wt.%). 24
Table 4 Maximum load and stress results of bending testing with qualitative failure description....... 54
Table 5 Mechanical Properties from Quasi-Static Bending Testing 78
Table 6 Basquin Parameters (Morrow, SWT) from cyclic three-point bending tests 89

Chapter 1

Introduction

1.1 Motivation

Climate change has unveiled several serious environmental concerns related to the automotive industry where efforts have diverged into two approaches: the introduction of hybrid/electric vehicles, and improved fuel economy. Fuel consumption and greenhouse gas (GHG) emissions are some of the most critical challenges faced in the automotive industry. The transportation sector was responsible for almost 30% of Canada's annual energy consumption and over 37% of Canada's GHG emissions in 2015. Passenger fleets accounted for more than 50% of the emissions from transportation. Similar trends across the world indicated the need for global and local environmental legislation targeted towards automotive fuel efficiency. A 50% improvement over 2008 vehicles is required by the U.S. CAFÉ standards by 2025 [1], while Canada is aiming to reduce overall GHG emissions by 30% between 2005 and 2030 [2]. This is indicative that more aggressive efforts towards emission reduction are crucial. The new standards and global competitivity amongst original equipment manufacturers (OEM) drive the strong motivation for technological innovation in this front.

These emissions regulations have consequently resulted in drastically improved fuel economy as a key constraint in the design of new generation transportation vehicles. Improved fuel economy by vehicle light weighting saw earlier initiatives with the replacement of the grey cast iron in the engine block with cast AlSi and iron/steel cylinder bore liners in the 1970's [3]. This resulted in up to 50% weight reduction in the engine [4]. The research around plasma transferred wire arc (PTWA) thermal sprayed aluminum-silicon alloy (AlSi) cylinder bores is motivated by the ongoing initiative to improve fuel economy through automotive light weighting efforts and the challenges surrounding cylinder bore liners. Liners can account for over 10% of the total weight of a typical six-cylinder engine block and have a thickness of over 2 mm, lowering engine volume and efficiency. Relative to these traditional liners, thermal sprayed coatings are significantly thinner, can increase cylinder volume, improve engine efficiency and tribological properties, and potentially resolve the aforementioned issue of deformation [5]. Sprayed coatings also have the potential to be more time and cost efficient regarding both automotive manufacturing and repairs. The high deposition efficiency and high feed rate of PTWA has made it appealing at the mass production level since complete cylinder processing can be completed in less than 60 seconds [6]. The technology can be applied to older cast iron or aluminum blocks, or worn engines that would have been scraped otherwise during remanufacturing [7]. Remanufacturing is a major benefit of coating technology: compared to manufacturing a brand-new engine, remanufacturing can have a significant effect on GHG emission reduction and sees over 85% savings on raw material and 55% less energy to produce. A study by Automotive Parts Remanufacturers Association reports the results of remanufacturing auto parts in the European automotive industry, showing that only among the 28 European Union members a potential CO_2 emissions reduction of 0.4Mt can be realized by allowing the remanufacturing of old/worn automotive parts. This study shows sizable natural resources savings of 88% in raw material, and 56% in energy can be made as compared to manufacturing a new part. It also suggests that the market can offer 32,000 additional job in EU [8].

1.2 Objectives

The objective of this project is to investigate the key PTWA coating candidates towards cylinder bore applications. While the coating is superior to the lining in many ways, there is a need to address the key challenges related to understanding the coating/substrate interaction under both quasi-static and cyclic thermo-mechanical loads. The local properties of the coating alone and coating/substrate interface, fracture mechanisms causing delamination, and coating cracking are of particular interest because they have not been addressed in the existing literature. The importance lies in determining the coating structure and properties, and their effects on the coating performance.

The objectives of this present work are to (1) characterize the microstructure and bonding mechanisms of the coating, substrate, and interface of steel PTWA coating on AlSi substrate, and (2) obtain quasi-static properties of the coating, and (3) obtain the cyclic properties of the coating under the appropriate operating conditions. The results from these objectives can be used to establish the coating structure and property relationship for the steel PTWA coated AlSi substrate.

1.3 Thesis Overview

The upcoming contents of this thesis are organized as a manuscript-based thesis. Chapter 2 highlights and reviews the key topics and literature that are relevant to the current research. Chapter 3 describes the materials, samples, and experimental methods involved in each stage of analysis, which extracted from the corresponding manuscripts and manuscript drafts.

Chapter 4 is a manuscript which has been published to Surface & Coatings Technology reporting the key research findings of the coating microstructure. These studies made key discoveries on the coating structure and features, interface, residual stress, and coating hardness and serve as an important prerequisite to understanding the quasi-static and cyclic properties, as well as the relationship between the structure and resulting failure mechanisms.

Chapter 5 is a manuscript draft that is to be published. It discusses the adhesion study of the coating, which is a necessary standard procedure in understanding the bonding of the coating to the substrate. The analysis is done using the experimental results and finite element modelling in tandem to determine the properties of the coating under a pull load, as well as the separation and failure mechanisms. In particular, the focus is divided among types of samples to determine the better candidate for bonding due to mechanical interlocking and/or metallurgical bonding.

Chapter 6 is partially the published manuscript from Chapter 4 and a second manuscript draft to be published, both discussing monotonic three-point bending testing. The published manuscript describes the quasi-static bending properties and failure mechanisms of samples extracted from the cylinder bore, which are consequently curved. This study poses limitations due to the constraints of both the extraction process and curved geometry but serves as the best representation of the given application geometry. The second study outlined by the manuscript draft describes the quasi-static bending properties and failure mechanisms of flat substrate sheets that are coated. While these samples are not curved like cylinder bores, they offer much more flexibility and breadth to experimental studies. The testing of flat samples was able to cover two substrate materials, two extraction orientations, and three temperatures (room temperature and elevated temperatures). This allowed for the comparison analysis of these key variables which affect the properties and more substantially, the failure mechanisms of the coated samples.

Chapter 7 is a third manuscript draft to be published. It discusses the fatigue behaviour and fracture mechanisms of the flat samples in Chapter 6 under three-point bending load. The behaviours are monitored for the same three variables (i.e., substrate material, orientation, temperature) and offer important insights into the performance of PTWA coated cylinder bores under typical engine operating conditions.

Finally, Chapter 8 outlines the conclusions of the studies pertaining to PTWA spray technology for engine cylinder bore application as well as future work recommendations. The letter of copyright permission and references follow.

The candidate is the primary author of all manuscripts and was responsible directly in data collection or coordinating it, as well as analysis of results. A detailed description of contributions of co-authors is provided in the Statement of Contributions. The modifications made to each article include an introduction, reorganizing sections, tables, figures, and references for appropriate integration into the thesis document.

Chapter 2

Background and Literature Review

2.1 Thermal Spray Coatings

Thermal spray technology has been used in various applications such as in turbines, engines, pumps, valves, industrial plants, and have been subject to different temperatures and operating conditions. They are used as both protective coatings and a means of part repairment. As a result, considerable work has been conducted on a wide array of spray applications. Common thermal spray processes include various plasma, PTWA, high velocity oxygen fuel (HVOF), high velocity air fuel (HVAF), and cold spray. Each process involves the heating (to different degrees) of a feedstock material to be deposited on a substrate material. Thermal sprays are an effective way to provide thick or thin coatings at efficient deposition rates to change the properties of the surface. The range of coating materials is vast, including metals, ceramics, composites, and plastics. The general concept behind the deposition is the application of successive particles on the substrate surface, which flatten to form splats, shown in Fig. 1. The coating structure and bonding at the interface will depend on the thermal spray process and deposition parameters.

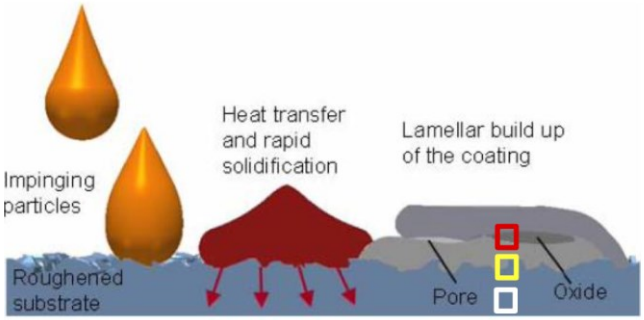

Fig. 1 Formation of thermal sprayed coating highlighting three areas of interest in microstructural analysis: coating (red), interface (yellow), and substrate near interface (white) [7].

The general advantages of thermal spray processes include their diversity and flexibility. As previously mentioned, a wide range of choices is available as feedstock material, and it can be used to coat intricately machined parts effectively as well as restore damaged parts or coatings without greatly affecting the properties. The most common uses of thermal spray technology pertain to improved wear resistance, corrosion resistance, thermal insulation and electrical conductivity in aerospace, automotive, power, and chemical industries. However, the choice of material is specific to the given application. The flexibility in thermal spray processes allow for many variables to be custom tailored to address specific needs including coating thermal properties (i.e., coefficient of thermal expansion), density, heat conductivity, and particle shape and size distribution [9].

For the application towards cylinder bores, the system must accommodate the small diameter and rotate coaxially to the bore (i.e., systems with a rotating spindle). Several thermal spray processes fit this setup, including rotary atmospheric powder plasma (APS), rotating twin wire arc (TWA), HVOF, and PTWA. The preferred feedstock is wire, which is easier to handle than powder feedstocks that require specific feeding equipment [4]. As a result, thermal spray technology development uses wire-based feedstock materials in order to meet the automotive industry's cost and process stability requirements [7]. Combined with the desired coating material, the PTWA process has been predominantly used for this application and engine remanufacturing/repairs due to its high wear resistivity. A comparison of thermal spray processes in terms of various engine bore coating criteria is outlined in Table 1.

Table 1 Comparison of thermal spray processes for coating deposition in engine cylinder bores [10]

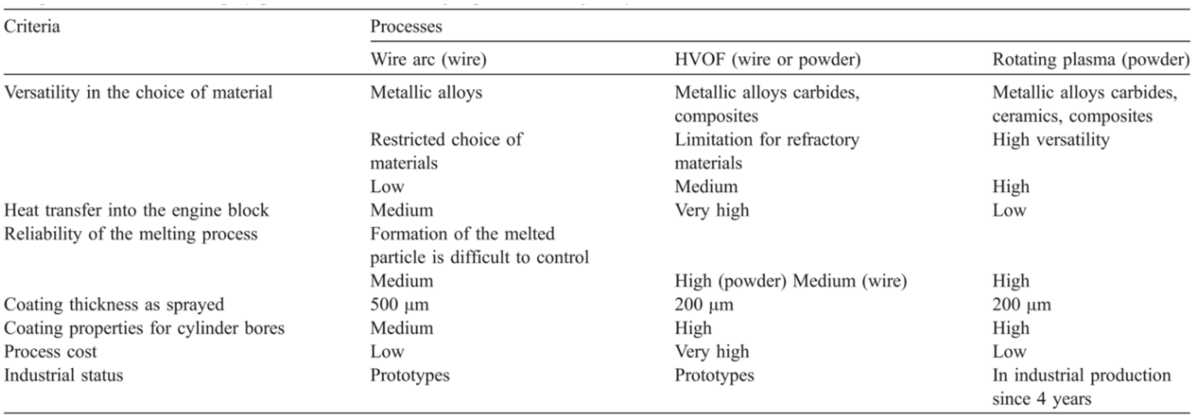

Criteria	Processes		
	Wire arc (wire)	HVOF (wire or powder)	Rotating plasma (powder)
Versatility in the choice of material	Metallic alloys	Metallic alloys carbides, composites	Metallic alloys carbides, ceramics, composites
	Restricted choice of materials	Limitation for refractory materials	High versatility
	Low	Medium	High
Heat transfer into the engine block	Medium	Very high	Low
Reliability of the melting process	Formation of the melted particle is difficult to control		
	Medium	High (powder) Medium (wire)	High
Coating thickness as sprayed	500 µm	200 µm	200 µm
Coating properties for cylinder bores	Medium	High	High
Process cost	Low	Very high	Low
Industrial status	Prototypes	Prototypes	In industrial production since 4 years

Previous studies of wire-based systems showed that the best results have been achieved by the PTWA process which produces a low cost and high-quality coating with a reliable system for engine bores. Due to the high speed of the spray particles, very dense coatings with low porosity (around 2%) can be applied to the bores. Additionally, PTWA systems have also been used in production at Caterpiller Inc. to repair engine and power train components with worn out surfaces [7].

2.2 PTWA Spray

The PTWA thermal spray process (Fig. 2) was first developed by Flame Spray Industries and is a common method of thermal spray application to liner-less cylinders. The process involves propelling the molten coating material (in this case, alloyed steel) to the substrate (diecast aluminum alloy) using a stream of atomizing gas at extremely high temperatures (~15,000°C) and velocities (200 to 300 m/s) to form splats on a substrate surface [11]. In the typical plasma spray process, the cooling rate is approximately within the 10^7 to 10^8 K/s range [12]. The plasma gun performs melting between tungsten cathode and copper anode nozzle. When molten particles are accelerated in the air, they are mixed with oxygen to produce wüstite (FeO) which is 70% harder than the coating steel matrix and thereby increases the wear resistance of the cylinder bore [5,13]. It has been previously shown that the hardness and roughness of the coating have a direct correlation to the coating wear performance [9].

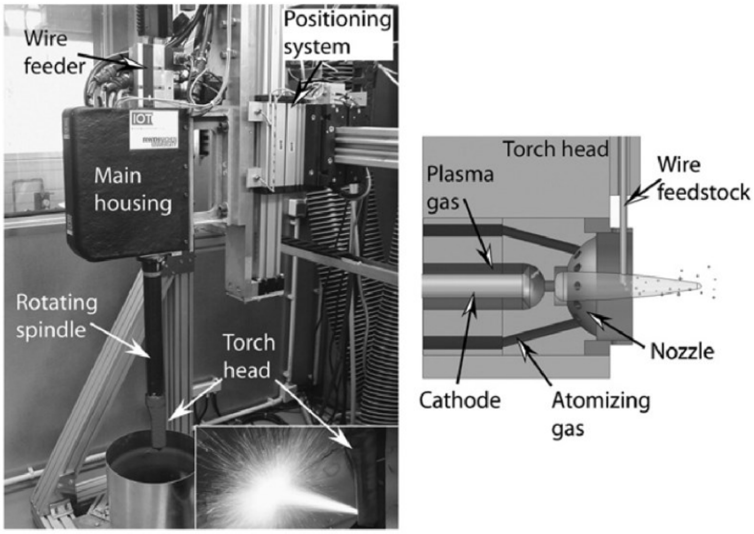

Fig. 2 Picture of PTWA system (left) and a schematic of the PTWA process (right) [4].

In vehicle engines, the steel liners in combination with the aluminum engine block introduced in the 1970's [3] resulted in a considerable weight reduction (up to 50%) in the previously cast iron block [4]. The liners undergo deformation that may lead to the development of a heat pocket, which increases oil and fuel consumption. To achieve high wear resistant hypereutectic AlSi alloys, the manufacturing (i.e., casting) process becomes difficult. Otherwise the low hardness and poor wear resistance properties of hypoeutectic AlSi alloys does not satisfy the contact tribological requirements between the piston ring and cylinder bore wall, making the liners a necessary addition [14]. This called for the necessary grey cast iron liners with embedded graphite lamellae that served as a natural solid lubricant. However, the required heat transfer during engine cycles was not satisfied due to the low conductivity of cast iron in high power level conditions. Thermal sprayed systems with aluminum substrates have the potential to pull generated heat away and allow engines to generate higher power levels, as well as alleviates the issues related to hypoeutectic and hypereutectic alloy substrates.

The topography obtained after the finishing process of PTWA sprayed liner-less bores significantly decreases both the coefficient of friction and fuel consumption by 2 to 4% [15]. The successful use of PTWA sprayed cylinder coatings is used in NASCAR and Formula 1 engines to achieve better performance and cost benefits [10]. These engines are typically rebuilt more often than consumer vehicles hence there is a need for a better understanding of the mechanical adhesion at the coating/substrate interface, as well as metallurgical bonding for this application. Further discoveries in the failure mechanisms due to coating/substrate interactions under various loadings are also necessary.

Prior to deposition of the PTWA sprayed coating, the substrate often requires a surface activation process to facilitate better mechanical interlocking of the sprayed material. This process is necessary in creating a rough surface that allows for more bonding strength between the substrate and the splats close to the interface. Finite element analysis has also been previously performed to determine the optimal profile dimensions of the dovetail geometry [19]. It was found that the bond strength between the coating and substrate was 48 MPa for grit blasted substrates and 58 MPa for surface activation involving dovetail pattern profiles [4]. The bonding strength resulting from surface activation is further discussed in Section 2.5 Hardness and Bonding Strength. Furthermore, the effects of dovetail profile height on adhesive tensile strength between substrate and coating was investigated. For heights as low as 25 to 45 μm, almost no interlocking between the surface activated substrate and coating was observed in adhesive tensile strength tests. However, the adhesive tensile strength increased from 38 MPa to 53 MPa with an increase of height from 75 μm to 105 μm [16]. Typically, an undercutting angle of 20° guarantees an interlocking between substrate and coating and fills undercuts with coating material. It was also found that in addition to interlocking, there were also diffusion effects between components. With increasing number of dovetail elements per length, higher coating/substrate connection strength was observed [17]. The variables in the dovetail profile geometry are shown in Fig. 3.

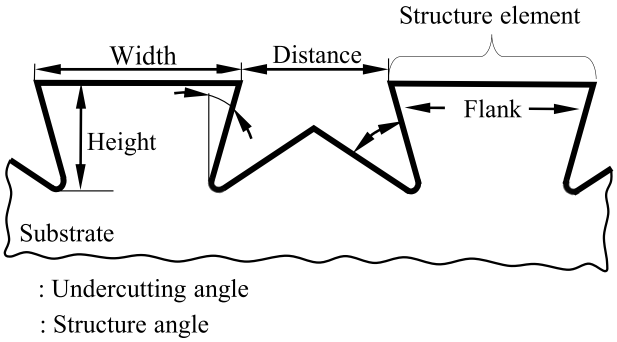

Fig. 3 Geometry of dovetail profile surface activation pattern [17].

In the case of thermally sprayed engine bores, interpolated selective area mechanical roughening can be used and is based on circular interpolation. The produced result is equivalent or higher in bond strength compared to other surface activation methods. The advantages lie in its ability to allow for roughening and coating of only a particular portion of the cylinder bore, reduced steel wire and energy consumption, and elimination of a bimetallic cut on the joint face of the block. The procedure involves the use of a peripheral milling tool and a rotary tool. These two tools are used to cut concentric grooves in the bore walls through interpolation, and deforms the grooves to produce an undercut, respectively. The optimal groove dimensions, primarily dependent on ratio of peak height (h) to crush (Δh), were investigated using finite element analysis (Fig. 4). This process was implemented reliably at low volume and has also be adapted for the purpose of roughening aluminum brake rotors [18].

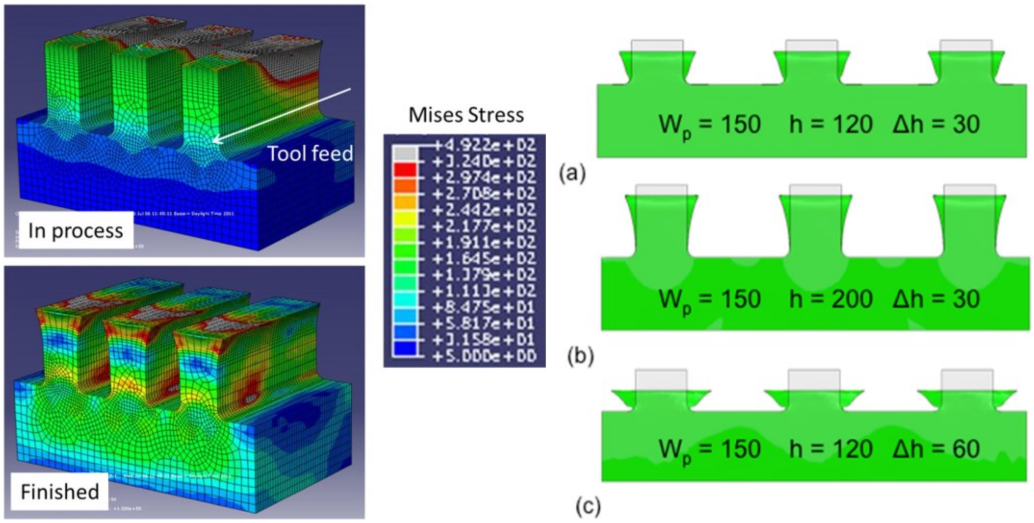

Fig. 4 Mises stress during/after deformation for 10 um peak width, 200 um peak height, 15 um crush and different profile parameters (a), (b), and (c) with FEA shape predictions [18].

After the process of surface activation is complete and the coating deposition is performed, the surface of the coating is post-processed by a selection of techniques, including machining and/or honing to produce the desired surface roughness and tribological requirements.

2.3 Microstructure

In general, the microstructure of thermal spray coatings can be described as layered structure. However, the inconsistent and irregular nature of the individual splat shapes consist of several smaller grains [19]. This causes the layered microstructure to be uneven in terms of the thickness of each layer and results in a lamellar microstructure with undulations [9].

Even when employing the dovetail profile during substrate surface activation, pores, voids, and oxides exist at both the coating surface and within the coat. In transmission electron microscope (TEM) investigations of PTWA coatings, the coating exhibited underlying microcrystalline (μc) matrix of ferrite (α-Fe) and nanocrystalline (nc) precipitates of cementite (Fe_3C) and wüstite (FeO) [19]. Wüstite is a hard oxide phase which serves as solid lubricant and is responsible for the good tribological properties of Fe/FeO coatings [20].

Previous studies found that due to the high-velocity material deposition process, the coating microstructure is comprised of both amorphous and crystalline structures [12]. However, this means the coating splat morphology that consists of pores and other features will act as locations of stress concentration leading to failure [5]. Generally, it was proposed that the pores between flattened splats were caused by loose packed layer structure or gas porosity phenomenon, while other pores within the particles were caused by volume shrinkage [21]. Open porosity was measured by the mercury intrusion technique (Quantachrome Autoscan 33 porosimeter) with pressure up to 230 MPa [22]. Total porosity was obtained by comparing the difference between density of the coated specimen and theoretical density [23]. Porosity is also affected by impact velocity of the PTWA process: in the case that it is too low, the result is increased porosity which is caused by the inability of the particle to penetrate into all surface cavities [9]. Thicker coatings are also found to have greater porosity, which contributes towards higher crack initiation [24]. Remaining pores caused by casting defects, even post-honing surface smoothing, can lead to an increase of the lubricant consumption during engine operation. As a result, it is important to control defect size at the surface [13].

Generally, structure porosity in coating is a good indication of the coat quality and increased strength can be obtained by reducing porosity [22]. In the case of PTWA, low porosity is the result of high deposition rates and good control over the process. For engine cylinder block requirements, porosity level of the material must be below 1% and the maximum pore size must be below 500 μm on the running surfaces [5]. It was found on coated cylinder bores, that porosity percentage is constant along the cylinder (~1%), but this was not the case for oxides [13]. An increase in Fe content also resulted in increased amount and size of pores. This can be attributed to the increase in β-phase (β-Al_5FeSi) which has platelet morphology that is needle-like and is the most detrimental to the intermetallic phase of cast AlSi alloys. By physically blocking the metal feeding, the β-phase promotes shrinkage porosity during solidification. This phase is more prone to crack linkage and failure when compared to α-iron (α-AlSiFe) that has a more compact morphology that is less detrimental to mechanical properties [25].

Oxidation of the sprayed coating can take place in the vapor phase surrounding the droplet or at the droplet surface in a vein-like configuration. The formation and growth of the oxide film on the metal surface are important as it induces residual stresses (RS) [26]. The low fracture toughness of the interfacial oxides can cause splat delamination upon frictional contact in ferrous coatings. The wear initiated by abrasion is then enhanced by splat separation, which is caused by the propagation of cracks at splat interfaces along the oxides [26]. Thin oxide layers are more prone to cracking, while thicker oxides are relatively resistant. Overall, the low fracture toughness of the interfacial oxide could cause splat delamination upon frictional contact in ferrous coatings. On top of that, wear initiated by abrasive loading is then enhanced by splat separation, which is caused by the propagation of cracks at splat interfaces along the oxides [26].

Pin-on-disk wear tests were performed on a sliding wear apparatus where the sliding speeds were between 0.2 and 2.5 m/s, and load was constant between 10 and 75 N. It was found that high wear rates at high loads/low speeds were due to the fracture of heavily deformed splat tips. However, at high loads/high speeds, surface oxidation was the main wear mechanism. A method was proposed by A. Edrisy to estimate friction induced contact surface temperatures of the thermal spray coatings. Surface temperatures in coatings with high initial iron oxide content would reach higher values during sliding contact, which would consequently promote surface oxidation [27]. Overall, it was found that increasing rotational speed of coating process parameters from 400 to 600 min^{-1} resulted in better oxide distribution, which provides better wear resistance of the coating [4]. Deposition atmospheres containing dust and heat (less ventilated) lead to higher oxidation thus thicker coatings, but it is still possible to manufacture very thick coatings without an effect on the microstructure's oxides [13].

2.4 Residual Stress

One of the factors that influences the fatigue life of thermal spray coated components is the RS of the coating which arises during the thermal spraying process. These stresses are inherent in the coatings because the process makes use of large temperature gradients with varying material mechanical properties. In many cases, the Young's modulus of the coating is only a small percentage of that of the substrate. In the plasma electrolytic oxidation (PEO) coating process, it was found that internal stresses were caused by three components of the process: (1) formation/growth of oxide film on metal surface, (2) thermal effects from surface micro discharges, and (3) phase transformations in oxide films. The degree of each component varies on the temperature level coating process history and impact velocity, and therefore can be controlled by deposition parameters. Thermal effects include stresses caused by differential thermal contractions between coating and substrate, as well as those caused by temperature gradients with the coating during treatment. The phase transformations for PEO coatings on an Al substrate involve a $\gamma \rightarrow \alpha$ transformation, and a similar phenomenon is observed in various other deposition methods [28]. The RS is also related to coating features: when oxides are present, they usually have a larger volume than the metal from which is formed, and if the oxide maintains crystallographic coherency with that metal, it is in compression while the metal is in tension. High compressive residual stress in the coating enhances fatigue life, but it may induce coating separation from substrate, intra-coating spallation, and formation of cracks [28].

Studies of HVOF thermal coating processes found that the distribution of the RS through tungsten carbide-cobalt (WC-Co) coated aluminum samples showed compressive RS at the coating surface with an increase through the coating (compressive), then approached zero while within the substrate material [29]. Three sample types of varying compressive residual stress were studied: high, medium, and low: the through-thickness plot of a high RS sample is shown in Fig. 5. It was found in constant deflection bending fatigue tests (cantilever) of these WC-Co HVOF sprayed coatings that there was a direct relationship – fatigue life can be changed by a factor of ten due to the degree of compressive residual stress in the coating. Increased compressive residual stress resulted in increased life of the specimen but may also introduce an increased likelihood of failure due to spalling [29]. Residual stress can either enhance or decrease adhesion strength, especially in thicker coatings [30]. Tensile residual stress in coated samples was found to induce early crack initiation [24].

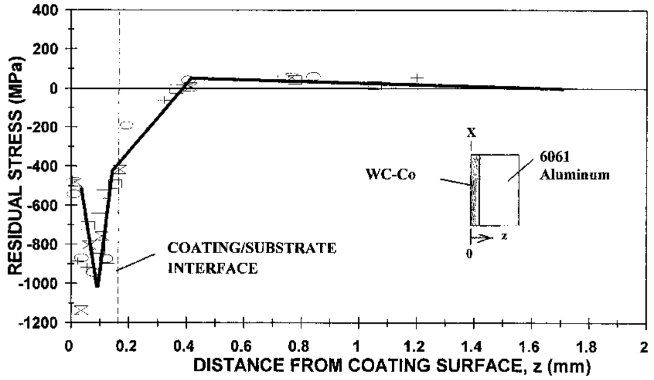

Fig. 5 Thorough-thickness residual stress distribution for four high RS specimens (WC-Co on 6061 Al with high compressive residual stress in coating) [29]**.**

Tests with ceramic thermal boundary coatings found that the adhesion between coating and substrate is mainly influenced by the residual stresses in the interface. Residual stress measurements in HVOF and APS spraying have shown that stresses in coatings strongly depend on the temperature level, coating process history, and particle impact velocity [30]. Grinding is an another process that was found not only to enhance the surface roughness in Cu-Ni-In coatings, but also to increase the magnitude of surface compressive residual stress [31]. Further testing specific to PTWA sprayed steel coatings and the related post-processing techniques are necessary to evaluate the state of RS and how it affects performance for the application of cylinder bores.

2.5 Hardness and Bonding Strength

Hardness is one of the critical parameters to evaluate coating performance – for example, it influences coating failure during fretting fatigue. The micro-hardness of flame-sprayed coatings is lower than that of HVOF sprayed coatings which can be attributed to microstructural changes associated with differences in the particle temperature and the cooling rate of the molten/semi-molten particles after deposition. It is also found in HVOF coatings that the micro-hardness remained almost constant throughout the coating and drastically reduced to the substrate micro-hardness at the interface [32]. The hardness of PTWA sprayed cylinder bores has yet to be comprehensively evaluated. Since adhesion of coating influences mechanical integrity of the coat-substrate interface during service, it is also an important factor to investigate. Additionally, cohesion (the bonding between particles in the coating), controls coating properties and performance [33].

For automotive applications, the bonding strength requirement must be above 30 MPa. When an adequately high surface activation is not achieved in the substrate before deposition, the coating may peel away from the surface. This will cause high thermal flux within the coating that cannot dissipate and lead to overheating with high oxidation in delaminated areas. The surface activation process is necessary in creating this rough surface to have better adhesion between the substrate and coating. This can be achieved by controlling surface roughness by grit-blasting or pressurized water jet or controlling the profile during mechanical roughening. It was found that mechanical roughening using a half circle profile yields low bonding strengths of 15 MPa, whereas creating holes using laser texturization gives a bonding strength of 25 MPa and grit-blasting of 40 MPa [13]. When the mechanical roughening process involves fine cutting using the aforementioned dovetail-like profile (Section 2.2 PTWA Spray) instead of grit blasting, the adhesion strength can be elevated to 60 MPa from 15 MPa, which falls greatly above the commended 30 MPa [7]. Partial delamination has been observed at both the coating-adhesive and coating/substrate interfaces, particularly at the circumference of the specimen.

Spray process, operating conditions, feedstock particle size distribution and morphology, substrate material, residual stress, and the environmental conditions affect the coating adhesion. Coating cohesion is mainly provided by interlocking of splat particles and adhesion strength [19]. It was found that cohesion failure was attributed to the pores and micro-cracks existing in the coated layer [9]. In the case that impact velocity is too low during the deposition process, poor adhesion occurs at the interface and poor cohesion occurs within the coating [9]. However, it was found that bonding strength could be improved by controlling the interfacial microstructures [34]. Lamellar bonding in ceramic coatings was shown to be dominated by particle deposition temperature, where bonding ratio at the lamellar interface can increase with the increase of temperature to over 80% [33]. Quasi-static adhesion tests suggest that coating/substrate failure is mainly due to adhesion failure [4], but failure due to cohesion has also been reported [9]. Due to the limited studies in the literature, supplementary investigations are necessary for monotonic adhesion/cohesion and bending to evaluate related failure modes and strength properties.

As-sprayed coatings have a low elastic modulus, which can be attributed to the weak boundary bonding between splats. The boundaries are weak due to the short splat bonding time during impact with the solid substrate or pre-deposited coating, as well as the surface of the liquid droplet undergoing oxidization for atmospheric spray of low carbon steels [35]. Lastly, in facilitating the creation of metallurgical bonds, conditions for incipient melting of the substrate by the impinging particle are favourable. Greater bond strengths are observed in particle-substrate systems when solidification-melting conditions are easily realized compared to a system where these conditions are not met [36].

2.6 Quasi-Static and Fatigue Properties

Interfacial fracture toughness has previously been investigated using quasi-static four-point bending tests with a saw-notched specimen and modified chevron-notched short-bar specimen, which were found to be a more sensitive means of evaluation in terms of mechanical integrity of coating/substrate interface compared to tensile testing [37]. During these bending tests, the loading caused crack initiation around the notch, and the main crack propagated through the thickness of the coating to the interface. This caused coating delamination along the coating/substrate interface. Cracking of the coating is another potential failure mechanism that is enabled by inconsistency in local coating properties (i.e., presence of pores and other features in the coating microstructure) [5].

Overall, the fatigue behaviour of coatings is dependent on surface properties such as hardness, roughness, coating thickness, and residual compressive stresses. Coating hardness and roughness affects the wear, while thicker coatings with compressive residual stress delay crack initiation and propagation [29]. All these factors have a hand in extending the fatigue life of the coating. Different loading conditions of the cylinder inner bore are induced during engine operation. Combustion pressure and thermal stresses caused by thermal loads contribute to the main loading of hoop stress, which are cyclic. This causes two modes of fatigue: High cycle fatigue (HCF) mode results from the fluctuating combustion pressure with a peak firing pressure as high as 200 bar, while low cycle fatigue (LCF) mode is from the start-stop engine cycle which creates a temperature difference in the cylinder and surrounding temperature of engine peak temperature (250°C). During this thermal cycle, the previously mentioned thermal expansion coefficient mismatch at the coating/substrate interface will cause notable thermal stresses. Further investigation is necessary to better understand the behaviour of PTWA coatings under cyclic thermal loading.

Previous plain fatigue tests showed that on each side of the interface, there are differences in elastic properties, as well as potentially significant Mode II shear from the thermal expansion mismatch between the coating and substrate [34]. Especially under cyclic loading, this mismatch is an area of concern. When fatigue properties were observed at various temperatures, the coating was found to have a higher fatigue resistance at elevated temperatures such as 300°C compared to room temperature [35]. This may be due to the rapidly increasing elastic modulus, which is attributed to annealing of the sprayed microstructure at such elevated temperatures. Additionally, oxide-rich regions were more prone to fatigue crack initiation in coatings [35].

Another factor that influences the fatigue life of the thermal spray-coated components is the RS in the coating, which arises during the spray process or post-processing. Prominent contributors to RS are the differential thermal mismatch between the coating and substrate, as well as stresses caused by temperature gradients within the coating during treatment [38]. Iron oxides are usually present in the coating; these oxides have a larger volume than the metal from which they are formed and if the oxides maintain crystallographic coherency with the matrix, they are in compression while the matrix is in tension. Previous works have found that high compressive RS in the coating delays crack initiation and enhances fatigue life [29]. However, compressive RS also facilitates coating delamination from the substrate, intra-coating spallation, and crack formation, which reduces wear resistance [28,39]. On the other hand, tensile RS in the coating has been found to induce early crack initiation [24].

Previous bending fatigue studies report that coating cohesion is mainly provided by the interlocking of splat particles and adhesion strength [19], while cohesion failure is attributed to the pores and micro-cracks existing in the coating layer [9]. Studies in fretting fatigue of thermally sprayed Al_2O_3 coatings on AA6063 substrate reported fretting fatigue behavior depended on coating hardness, roughness, thickness, and RS [40]. Wear resistance was found to be influenced by hardness and roughness, while thicker coatings with compressive residual stress delay crack initiation and propagation leading to extended fatigue life [29]. Of the limited comprehensive studies that are available in the literature, few reported PTWA coatings specifically, and many involve sample materials that are not relevant to engine bore applications. As a result, there is a need to evaluate the fatigue properties of PTWA coatings, specifically related to the cylinder bore application. Additionally, due to the thermal mismatch of the coating and substrate materials that are present in this application, testing at elevated temperatures is also an area of interest and potential research.

Chapter 3

Materials and Experimental Methods

3.1 Coating Characterization Samples and Methods

The materials used in this study include a typical mild steel alloy that is PTWA coated on diecast AlSi alloy substrate. All samples were prepared by Comau LLC USA in Michigan using PTWA process and deposition parameters for application in engine block bores similar to parameters reported in [13]. The chemical compositions of the substrate and coating materials are reported in Table 2.

Table 2 Chemical composition of the materials used in this investigation (in wt.%).

Cast Aluminum	**Si**	**Cu**	**Mg**	**Mn**	**Fe**	**Zn**	**Ni**	**Others total**	**Al**
	7.5-9.5	3.0-4.0	<0.3	<0.5	0.8-1.3	<3.0	<0.3	<0.5	bal.

Steel Alloy	**Fe**	**Cr**	**Mn**	**C**	**Si**	**Mo**	**S**	**P**	**-**
	97.3-98.22	0.8-1.1	0.4-0.6	0.28-0.33	0.15-0.35	0.15-0.25	<0.04	<0.035	-

Since it is not possible to obtain the properties of the coating by traditional tensile testing, results from Anton Paar instrumented cyclic indentation were used. In this process, a spherical indenter is used to successively indent a single location to obtain representative stress-strain curves. Based on properties from Anton Paar analysis, the yield stress is 785.5 MPa in the coating, and 322 MPa in the substrate. Both coating and substrate values from the Anton Paar results were considered in analysis since the ratio of the two relative to each other is important. The data from Anton Paar results is shown in Appendix A.

The substrates used in this investigation were mechanically roughened. The dovetail geometry is very similar to those used in other studies and was chosen due to its superior bond strength (up to 60 MPa) compared to other activation methods, such as grit or water jet blasting (as low as 15 MPa, which is lower than the recommended 30 MPa), and differing profile geometries [9,24]. The dovetail-like surface profile is achieved by interpolated selective area based on circular interpolation with two tools: (1) a side cutting end mill with peripheral grooves that cuts concentric grooves through interpolation, and (2) a rotary tool that deforms grooves to produce an undercut [18]. As a result, this surface activation approach and geometry is chosen as a prime candidate by automotive manufacturers due to its potential application to cylinder bore coatings.

The samples were in the form of cylindrical sleeves with PTWA coating deposited on the inner surface (Fig. 6). Due to the orientation of the surface roughening process, the dovetail cut profile is only visible along longitudinal cross-sections of the cylinder sleeve (Fig. 7(a)). Rectangular samples were extracted from the cylinder sleeves for microstructure analysis (Fig. 7 inset) hot mounted in two different orientations using conductive resin, and polished. The face along the longitudinal direction with a visible dovetail profile is shown in Fig. 7(a). The face along the circumferential direction in Fig. 7(b) is parallel to the rows of dovetails, and therefore does not show the profile. Secondary electron (SE) and back-scattered electron (BSE) SEM imaging from the FEI Quanta Feg 250 ESEM with EDX (20 kV) was used to reveal microstructural features and determine elemental composition for both etched and non-etched conditions. Another set of SEM samples were prepared using 1 μm diamond paste polishing followed by argon ion milling for 30 mins at 8 kV with 3 degrees gun tilt in a Gatan Precision Etching Coating system (PECS™ II) [41] in order to obtain images that better feature re-solidified particles.

Fig. 6 As-sprayed, diahon, and machined cylindrical sleeves with PTWA coating.

Coatings in their original as-deposited state are post-processed to achieve a smooth mirror-like surface finish. After the coating deposition, the samples were subjected to the machining or diahon process. Machined samples have the as-deposited coating that is subjected to conventional cutting insert rough machining. Diahon samples have the as-deposited coating that is subjected to quasi-hone grinding (20-30 μm particle size) rough machining. Based on a preliminary microstructure study, it was found that the as-deposited samples have a coating thickness of roughly 800 μm, varying due to the roughness at the surface, and post-processed coatings were 300 μm thick (reduced by ~500 μm). Imaging of the coating surface also revealed that the honing step for both processes produced a cross-hatched surface texture. The main purpose of the post-processing, regardless of the method, is to smoothen the surface of the as-deposited coating. This is a necessary step that reduces stress concentrations and failures that occur directly due to the surface roughness. The two methods are investigated in order to confirm that post-processing differences do not affect the various properties that are studied, and rather the only notable difference lies in the properties between as-deposited samples and post-processed samples (regardless of method).

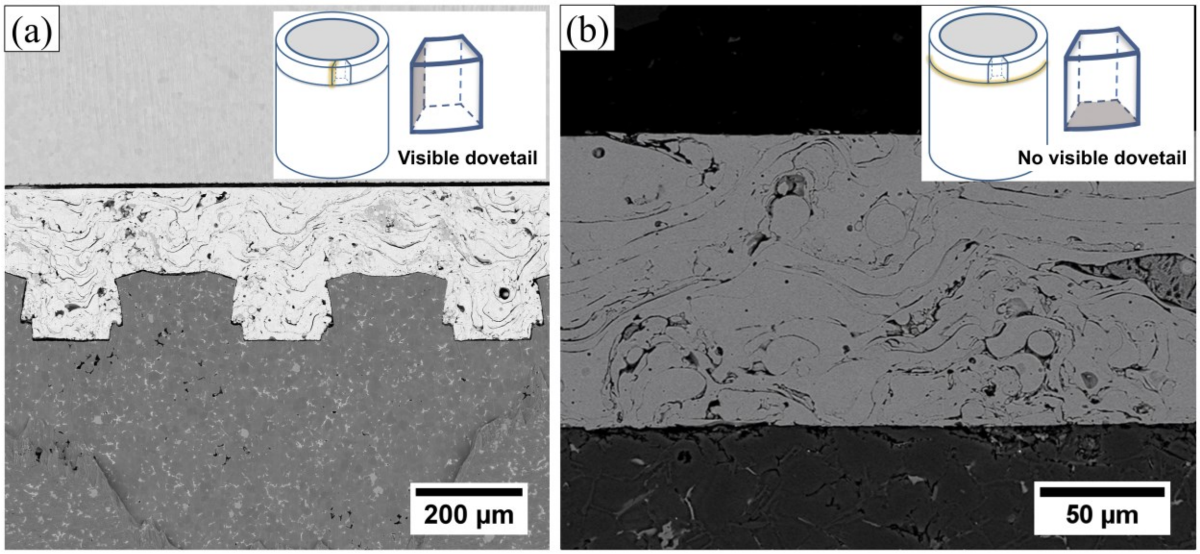

Fig. 7 Cross-sectional Backscattered-Electron (BSE) SEM image of dovetail profile with inset cut sample location along (a) longitudinal direction, and (b) circumferential direction.

3.2 Interface Characterization Samples and Methods

The same specimen extracted from the coated cylinder bores described in Section 3.1 Coating Characterization (material composition in Table 2) were used to characterize the coating/substrate interface. The TEM sample lamella was prepared from a mounted and polished sample using the focused ion beam (FIB) method and then observed under TEM (JEOL 2010F) operated at 200 kV.

3.3 Surface Roughness Samples and Methods

As a preliminary study, the surface roughness of the coating surface was evaluated. In order to better understand the surface differences between as-deposited and post-processed samples, the surface roughness of the varying states of coatings were measured from 2 × 2 mm^2 area using the Keyence laser scanning confocal microscope. The specimen and materials are identical to those described in Section 3.1 Coating Characterization and Table 2.

The evaluation of the cylinder coating surface roughness is also critical in order to match the surface preparation of bending samples, further discussed in Section 3.8.1 Bending Samples.

3.4 Residual Stress Samples and Methods

The RS through the coating, interface, and substrate were measured by both the XRD and the hole drilling methods. The XRD method measures surface residual stresses whereas the hole drilling method provides through the depth measurements. Electropolishing method was used to remove layers of the surface for successive XRD residual stress measurement to obtain residual stresses through the coating thickness. The XRD measurements involved ring samples that were cut laterally from the cylinder sleeve (described in Section 3.1 Coating Characterization and Table 2) to preserve stress in the hoop direction. The thickness of these cuts was approximately 10 mm, and the rings had an inner sleeve diameter of 84 mm (Fig. 8(a)). Through-thickness RS of the coating and substrate was measured using a Bruker D8-Discover XRD equipped with a VÅNTEC-500 two-dimensional area detector at an operating condition of 30 kV and 45 mA. The Cr-K_α (λ=2.2897 Å) was used on the Fe [211] plane (2θ=156.08°) with the $\mathrm{Sin}^2\psi$ method [42]. The measurements were taken from the inner coated surface of the rings as shown in Fig. 8(a). To determine the RS through the coating thickness, successive layers were removed electrolytically. The layer removal was conducted by electropolishing using the PROTO Electropolisher (Model 881). PROTO Electrolyte A was used with a 6 mm diameter round probe and 20-59 V for 10 seconds. Each sample was evaluated at three different locations on the ring at 120° apart to obtain multiple measurements per sample.

The SINT Technology RESTAN-MTS-3000 device was used for the RS evaluation by the hole drilling method. 1-SINTD2/1 diamond inverted cone endmills were used due to the high hardness of the material. To accommodate the installation of strain gauges, rings with wider dimensions (15 to 20 mm) were cut from the sleeve (Fig. 8(b)). The laterally cut cylinder rings were partitioned into three samples, each encompassing 120° of the rings, using waterjet cutting to reduce the amount of induced stresses and released hoop stress before measurement (Fig. 8(b)). Tokyo Measuring Instruments Lab FRAS-2-23-1LJB strain gauges with 2 mm gauge length were installed using Micro-Measurements M-Bond 200 adhesive to measure the strain released during drilling. The drilling begins on the coating side, through the interface, and into the substrate. Each drilling depth increment was 20 μm with a nominal hole diameter of 1.8 mm and advancing speed of 0.1 mm/min with a 5 second pause between each measurement. The SINT EVAL software was used in post-processing the micro-strain measurements and calculating the RS in the hoop direction using the Integral method which is an isotropic linear elastic model. In the case of hole drilling, its advantages lie in the resolution that can be obtained through the depth of the coating, as well as the accuracy of the depth measurement.

The advantages of the XRD measurements lie mainly in the fact that full ring samples can be tested and stress in the hoop direction can be preserved. However, the successive removal of the coating by electropolishing does not allow for as many measurements through the coating depth compared to the hole drilling method, and the accuracy of each 10 second removal is less precise compared to each hole drilling depth interval. The hole drilling method allows for more resolution through the depth of the coating, but due to the limitations in accommodating sample shapes, the cylinder ring sample must be cut, potentially releasing hoop stresses which are of particular interest.

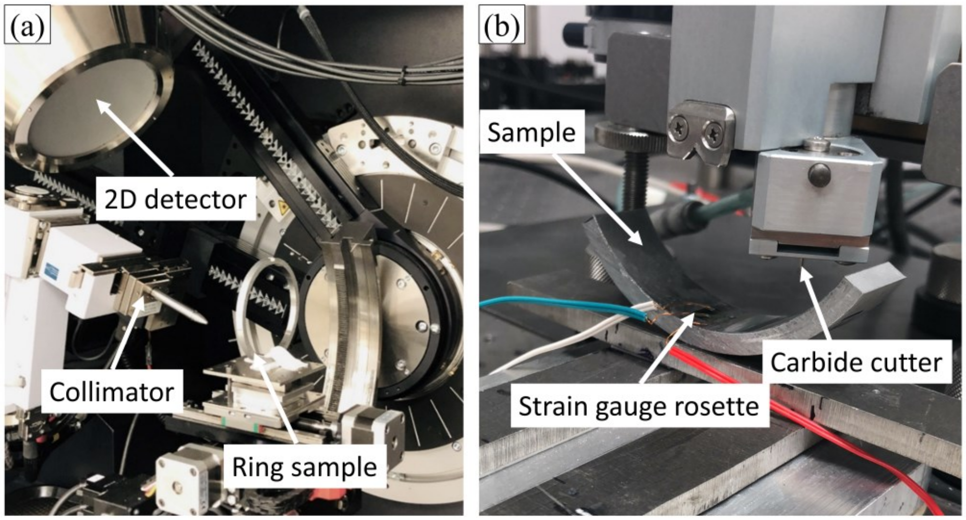

Fig. 8 Experimental set-up for RS measurements using (a) XRD method, and (b) hole drilling method.

3.5 Coating Hardness Samples and Methods

The hardness of the coating and substrate was measured using both Vickers micro-hardness and nano-indentation tests. The same samples from microstructural analysis (described in Section 3.1 Coating Characterization and Table 2) were used in this study. Samples were also prepared in the same manner as SEM characterization – hot mounted in resin and polished. The Clemex JS-Tango (100 gm load and 10 second dwell time) was used for micro-harness measurements. The Anton Paar NHT^3 with Berkovich indenter (50 mN and 100 mN load, 5 second dwell time) was used nano-scale hardness measurements. Vickers micro-hardness measurements were taken starting from the coating, passing through the interface, and then to the substrate side at a 45° angle to obtain more indentations within the coating depth. Nano-indentation tests targeted more localized areas of interest, such as specific coating features (e.g., re-solidified particles, splats, boundaries), which is beyond the achievable resolution of micro-hardness testing. A 100 mN load was used for nano-scale measurements within re-solidified particles, large oxide-rich regions, and splats areas. A 50 mN load was used to create a smaller indentation within areas that required higher precision where 100 mN indentations would include regions outside the area of interest (i.e., oxide boundaries between splats).

3.6 Adhesion Testing Samples and Methods

Adhesion pull testing will offer insight into the adhesion strength and allow evaluation of failure modes and trends related to interface adhesion and coating cohesion. It also provides a better understanding of the differences between varying surface activation techniques when subjected to this type of loading. However, the physical pull test report results that encompass both the mechanical interlocking, as well as possible metallurgical bonding or other factors at play. Alternatively, finite element modelling (FEM) can be used to investigate the adhesion strength provided solely by mechanical interlocking. By coupling this experimental work with finite element simulations, the role of mechanisms besides mechanical interlocking can be determined. The other aspects of loading that cannot be monitored during experimental testing (i.e., stress concentrations, separation behaviour) can also be observed using FEM.

The adhesion study is a key part of addressing the challenges related to understanding the coating/substrate interaction under both quasi-static and cyclic thermo-mechanical loads. The importance lies in determining the various coating properties and their effects on the coating performance. The objectives of this present work are to (1) obtain adhesion properties and behaviour of steel PTWA coating on AlSi substrate, and (2) determine the relationship between these results and the coating microstructure/properties. The results from these objectives can be used to establish the overall coating structure and property relationship for the steel PTWA coated AlSi substrate. Future work is required to determine fatigue properties, including those at elevated temperatures.

The materials used in this study vary slightly from the previous microstructural studies (Sections 3.1, 3.2, 3.3, 3.4, and 3.5) and include a typical mild steel alloy that is PTWA coated on diecast AlSi alloy substrate (A319 and A356). All samples were prepared by Comau LLC USA in Michigan using the PTWA process and deposition parameters for application in engine block bores similar to parameters reported in [13]. The chemical compositions of a typical diecast AlSi alloy substrate and coating materials are reported in Table 2.

Table 3 Chemical composition of the materials used in this investigation (in wt.%).

A319	**Si**	**Cu**	**Mg**	**Mn**	**Fe**	**Zn**	**Ni**	**Others total**	**Al**
	5.5-7.5	3.0-4.0	<0.5	<0.5	<1.0	<3.0	<0.5	<0.5	bal.
A356	**Si**	**Cu**	**Mg**	**Mn**	**Fe**	**Zn**	**Ti**	**Others total**	**Al**
	6.5-7.5	<0.25	0.25-0.45	<0.35	<0.5	<0.35	<0.25	<0.15	bal.
Steel Alloy	**Fe**	**Cr**	**Mn**	**C**	**Si**	**Mo**	**S**	**P**	**-**
	97.3-98.22	0.8-1.1	0.4-0.6	0.28-0.33	0.15-0.35	0.15-0.25	<0.04	<0.035	-

The substrates used in this investigation were mechanically roughened – two interface geometries were chosen and are like those used in microstructural analysis studies: a dovetail and a wave pattern. Fig. 9(a) and (b) show the dovetail pattern, while (c) and (d) show the wave pattern. The dovetail was chosen due to its superior bond strength (up to 60 MPa) compared to other activation methods, such as grit or water jet blasting (as low as 15 MPa, which is lower than the recommended 30 MPa). Industry development has recognized that this is a particular surface activation pattern of interest. Note that the dovetail profile in this analysis varies slightly from the one seen in cylinder bore samples for microstructural analysis (Fig. 7(a)). The wave pattern is a lesser known and more newly introduced pattern that has a high potential to resolve the bonding issues seen in typical dovetail patterns (i.e., disturbed splat structure), as well as a candidate that may yield more successful mechanical interlocking. Finite element analysis has also been previously performed to determine the optimal profile dimensions of the dovetail geometry [18]. To further improve the effectiveness of mechanical interlocking, the wave pattern was selected for consideration.

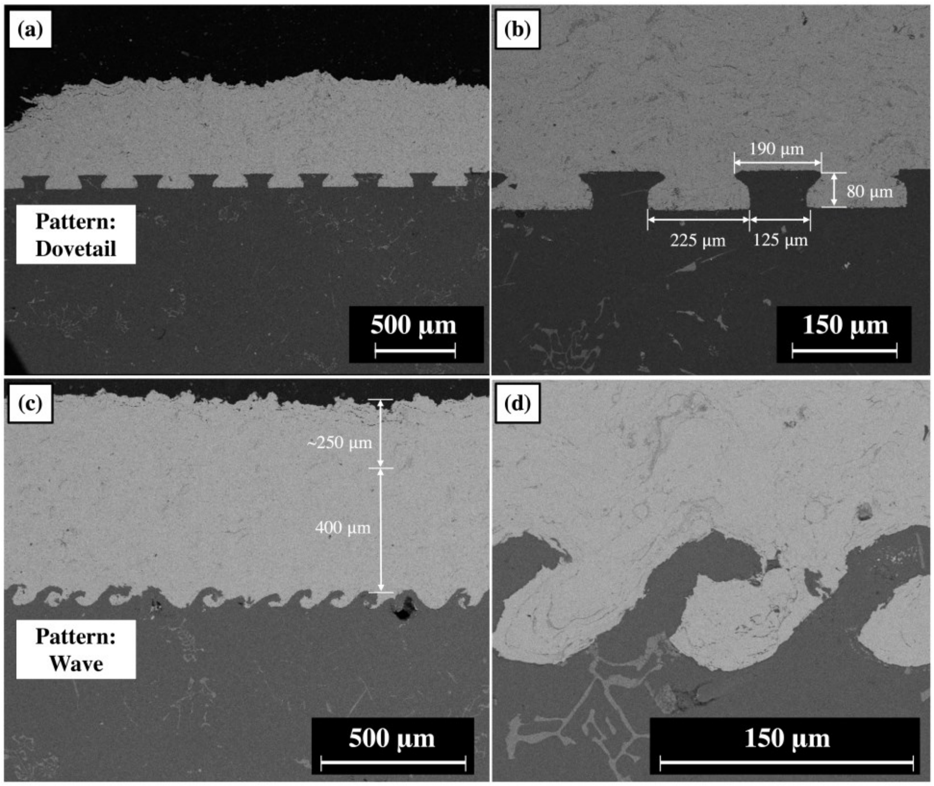

Fig. 9 Micrographs of two interface patterns showing (a) dovetail pattern with as-deposited coating, (b) dovetail pattern geometry, (c) wave pattern with as-deposited coating, and (d) close-up of wave pattern.

3.6.1 Adhesion Test Setup

ASTM C633 standard test method for adhesion or cohesion strength of thermal spray coatings was used for testing. ASTM C633 is appropriate for thermal sprayed coatings of thickness greater than 380 µm. Based on a preliminary microstructure study, it was found that the as-deposited samples have a coating thickness of roughly 650 µm, varying due to the roughness at the surface. The coating surface was machined to produce a smoother surface and post-processed coatings were 400 µm thick (reduced by ~250 µm). The samples were in the form of coupon aluminum samples, resembling short cylinders with steel PTWA coating deposited on the top circular face. This coating reduction region is shown in Fig. 9(c) and Fig. 10(a) and (b) show the preparation of the samples before and after machining. In this case, the coupon and counterpart both had a radii of 12 mm. The test setup and coupon geometry are shown in Fig. 10(c) and (d), respectively.

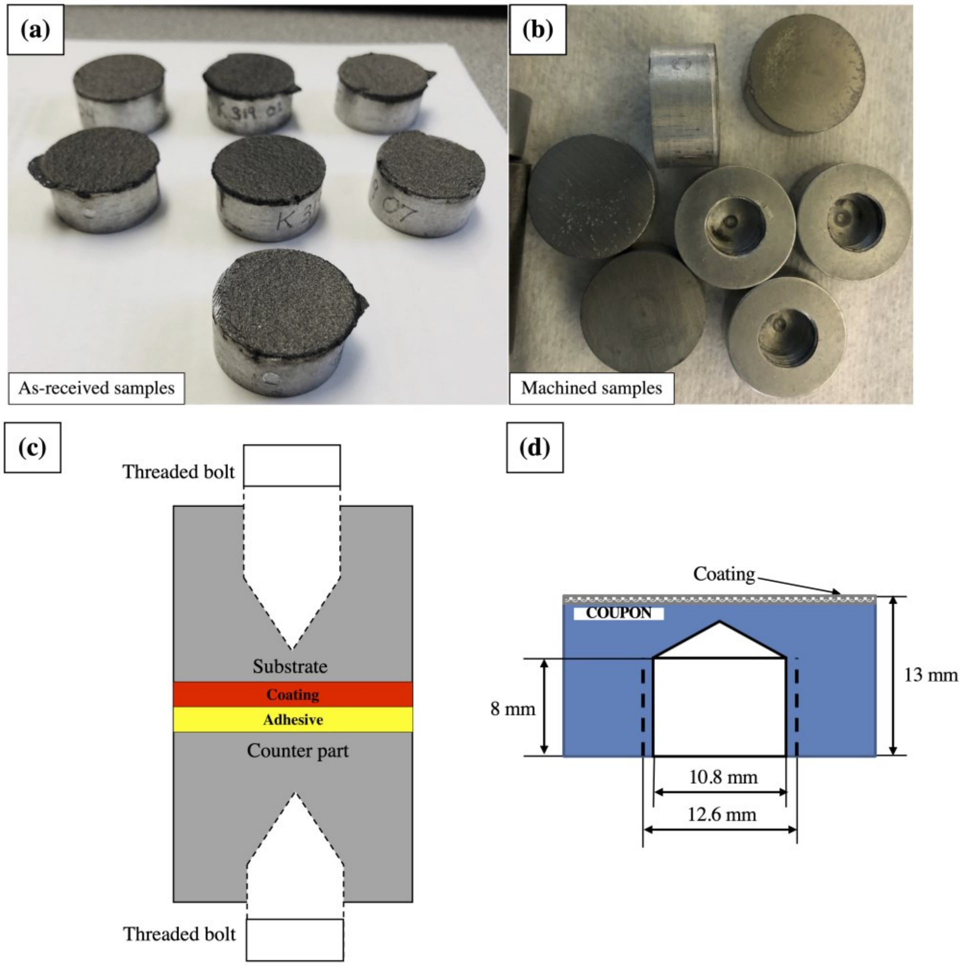

Fig. 10 Coupon samples (a) as-received and before machining, and (b) post-machining to smooth the coating surface, and adhesion testing (c) setup, and (d) coupon geometry with threaded hole.

Three types of samples were tested: (1) D319: dovetail pattern with A319 substrate, (2) W319: wave pattern with A319 substrate, and (3) W356: wave pattern with A356 substrate. Coating and counterpart mating surfaces were cleaned and degreased prior to the application of Master Bond EP15ND-2 adhesive, which was used to join the two surfaces with a bond line thickness of 50-127 µm. In alignment with the ASTM C633 strain rates (0.013 mm/s to 0.021 mm/s), a rate of 0.015 mm/s was used (monotonic tension), and five repetitions are recommended. The 25 kN 8874 Instron Biaxial tensile frame was used for uniaxial tensile testing. Coupon samples and counterparts were secured and aligned in the Instron using a fixture (Fig. 11), adhesive was applied, and grips were lowered to specify the bond line thickness. The two parts were clamped together using an alignment fixture to ensure no eccentric load or bending moment to the specimen during testing. The adhesive was cured within the Thermo Scientific Lindberg/Blue M oven with the alignment fixture at a temperature of 300-350°F (150-177°C) for 60 to 90 minutes. Maximum load is recorded at the point of rupture and the corresponding pull strength is calculated by dividing the maximum pull load by the circular cross-sectional area. Each specimen failure is described as to whether failures occurred at the coating/substrate interface (i.e., adhesion), in the coating (i.e., cohesion), in the bonding agent (i.e., epoxy), or a combination of these. Average stress of each of the three sample types (D319, W319, W356) is reported, along with the standard deviation.

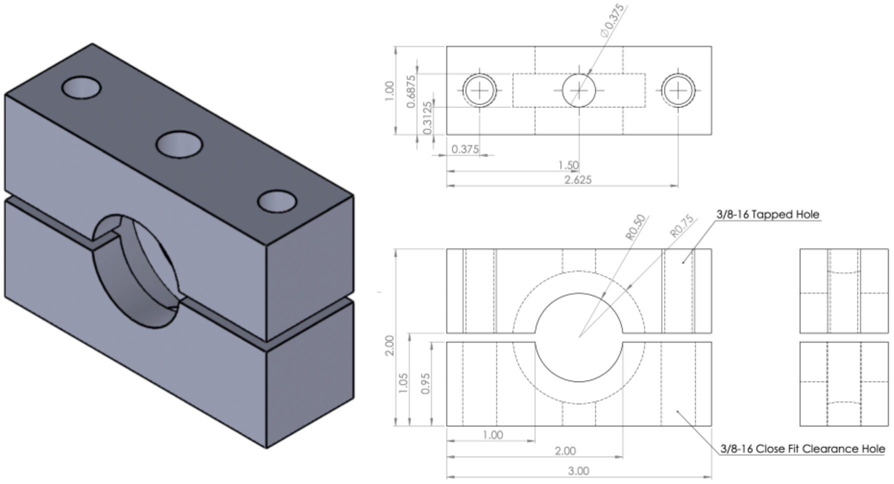

Fig. 11 Alignment fixture for adhesive curing.

SEM analysis was performed using the FEI Quanta Feg 250 ESEM (with EDX) in high vacuum mode (20 kV beam). The samples were cut perpendicular to the rows of the surface activation dovetail/wave pattern to observe two specimen orientations: at the fracture surface, and the side cross-sectional view such that the dovetails are visible. The fracture surface will provide a qualitative representation of the type of failure and amount of coating remaining across the coating surface. The cross-sectional view shows the layers and depth of coating removed, as well as deformation from the interfacial interlocking.

To determine possible intermetallics at coating/substrate interface, an exposed three-point bend tested fracture surface was observed under SEM (Zeiss LEO 1530). Elemental distributions were evaluated using the EDX for Fe, Al, Si, and O.

3.6.2 Adhesion Simulation

ABAQUS finite element modelling was used to simulate the pull tests of the two varying surface activation geometries. Three models were devised based on the dovetail and wave drawings, shown in Fig. 12(a) and (b). Since the wave pattern had many discrepancies from its ideal drawing, a model was also created using an SEM image of the pattern (Fig. 12(c)) by digitizing the points of an SEM image using MATLAB.

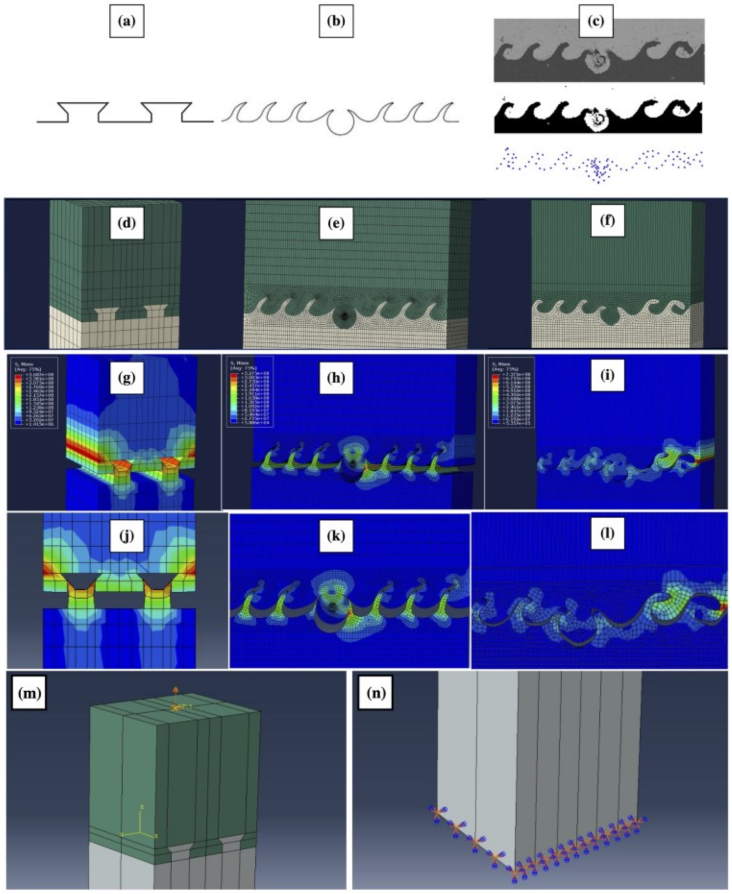

Fig. 12 Basis of the three finite-element models: (a) dovetail drawing, (b) wave drawing, and (c) wave SEM image. Perspective view of models for (d) dovetail drawing, (e) wave drawing, and (f) wave SEM image. Perspective view of stress distribution for models based on (g) dovetail drawing, (h) wave drawing, and (i) wave SEM. Two-dimensional separation view for models of (j) dovetail drawing, (k) wave drawing, and (l) wave SEM image. Boundary conditions are shown for the (m) Applied displacement is shown at the (m) top face and boundary conditions are shown for the (n) bottom face.

Three-dimensional models were created, as opposed to two-dimensional, in order to best obtain pull strength results that matched the experimental values. The pull strength is obtained by dividing the applied load by the contact area of the coating and substrate. The three-dimensional model allows the contact area to be considered more accurately and consider the locations where stress concentrates. Sub-size models were used to reduce the complexity of the models – varying views are shown in Fig. 12(d) through (l). The interface region was modelled as a surface-to-surface contact with an interaction property static friction coefficient of 0.61 for unlubricated mild steel on aluminum [43]. At the bottom surface, the model is constrained in all directions. Specified displacement is applied at the top surface. Structured hex (i.e., C3D8R) elements were used for the mesh. While a mesh analysis is more difficult for the intricate wave pattern model (18,576 nodes, 14,568 nodes), a mesh convergence study was performed to show that the intricacy of the mesh used in the dovetail pattern converged quickly and the moderately coarse mesh shown (2637 nodes, 1904 elements) could be used effectively.

A main limitation of the models is that they closely resemble the interface pattern of the test specimen, but the occasional irregularities are not accounted for along the dovetails. In the models based off drawings the irregularities through the depth of the dovetail rows are also not accounted for, which would affect the mechanical deformation of the interface pattern observed in experiments. Additionally, the layered splat structure and various features of the coating (i.e., splat boundaries, re-solidified particles, voids) are not represented. Cohesive breakage within the coating would be heavily dependent on the coating structure and features, which is not reflected in the stress distribution of the model. Lastly, only mechanical bonding is modelled (metallurgical bonding and other mechanisms omitted).

3.7 Quasi-Static Bending Samples and Methods for Curved Cylinder Specimen

Rectangular samples for quasi-static three-point bending tests were machined (dimensions 12 × 70 × 5 mm^3) from the cylinder bores used for microstructural analysis studies (Section 3.1 Coating Characterization) with the same material composition (Table 2). Samples were extracted along the longitudinal direction to include both the substrate and coating material. Due to the original cylindrical shape, the machined samples contained a slight curvature along the width (12 mm dimension). ASTM D5947 standard test methods for physical dimensions of solid plastic specimen was used as a basis to dimension the PTWA coated samples, though samples in this case were curved.

To visualize the crack initiation and propagation during testing, the reflective coating surfaces were painted white.

ASTM E290-14 standard test methods for bend testing of material for ductility was used for testing. Three-point bend tests were performed using the 8873 Instron uniaxial machine and monitored with a Digital Image Correlation (DIC) system. The load was applied on the substrate side to facilitate cracking on the coating side at a loading rate of 1 mm/min. Using the equivalent section analysis method [44], stress at various points can be calculated; the maximum tensile stress (coating surface) and both sides of the interface (substrate and coating) are the locations of interest. A bottom and side view of the loading process was captured using the DIC. A total of six samples were tested and fracture surfaces were observed under the Zeiss Leo 1530 FESEM. The displacement-controlled tests used a ramp loading path with a rate of 1.00 mm/min.

The force data recorded from the tensile frame allowed the stress to be obtained using the equivalent section analysis method [44]. By transforming the composite material (i.e., a combination of hard steel coating and soft Al substrate) to a single material for calculations, the stress at the coating surface can be calculated from three-point bending test results.

3.8 Quasi-Static and Cyclic Bending Samples and Methods for Flat Plate Specimen

ASTM E290-14 standard test methods for bend testing of material for ductility was used for testing. ASTM D5947 standard test methods for physical dimensions of solid plastic specimen was used to dimension the PTWA coated samples.

3.8.1 Bending Samples

The same flat plates are used for quasi-static and bending samples. The plates have the same surface activation profiles as the adhesion studies (Section 3.6 Adhesion Testing Samples and Methods), and material composition (A319 and A356, specified in Table 3). The substrate material is mechanically activated at the interface using the wave pattern, shown in Fig. 13. The as-deposited coating in Fig. 13(a) was machined to eliminate the roughness at the surface, shown in Fig. 13(b). All bending specimen must be prepared to match the coating surface that is found in its application to the engine cylinder bores.

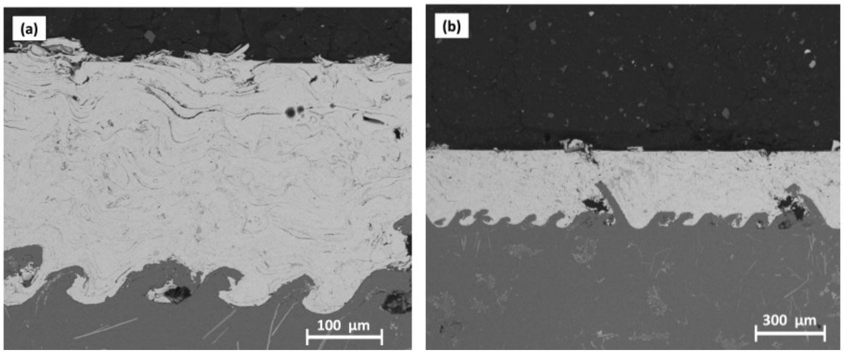

Fig. 13 SEM images of the interface region with wave pattern that was cut into the substrate at the bottom showing (a) as-deposited coating, and (b) after machining to smooth the coating surface.

A specimen extracted from a coated cylinder bore is shown in Fig. 14(d) which is used to match the desired surface of the bending samples to the cylinder bores. The specimen with as-deposited coat in Fig. 14(a) is machined to achieve the smooth surface shown in Fig. 14(b). The surface must then be subjected to various successive grinding processes to achieve engine bore surface quality. The image of the specimen post-grinding is shown in Fig. 14(c), where the grinding process has achieved a mirror finish on the coating.

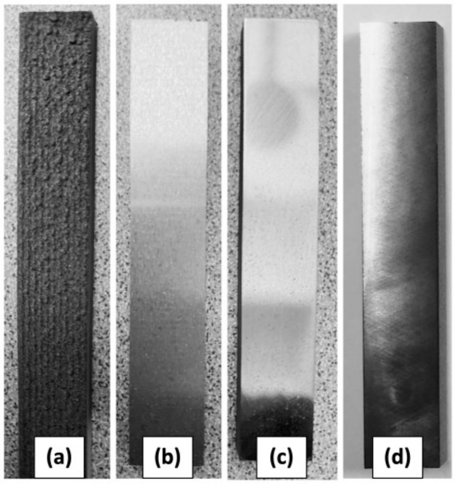

Fig. 14 Photograph of bending samples at various stages of preparation: (a) as-deposited coating, (b) machining shown in Fig. 13(b), (c) final product after grinding, and (d) sample extracted from coated cylinder bores.

To determine the appropriate surface quality of bending samples, images of the engine bore coating were evaluated and shown in Fig. 15. A similar image shown in Fig. 16(a) can be used for comparison with Fig. 16(b) and (c), which show the bending sample coating surface after being ground to 800-grit and 1200-grit, respectively. It can clearly be seen that the 800-grit surface better represents what is seen at the surface of coated engine bores. Keeping the bending sample coating in an as-deposited or as-machined state (Fig. 14(a) and (b)) will result in early crack initiation and failure of the coating, and the coating in its intended application will not be well-represented in testing.

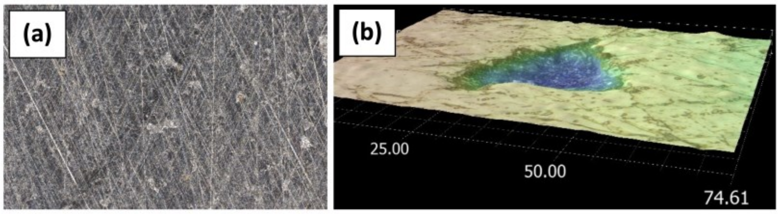

Fig. 15 Coating surface of cylinder bore samples using (a) SEM and (b) scanning optical microscope.

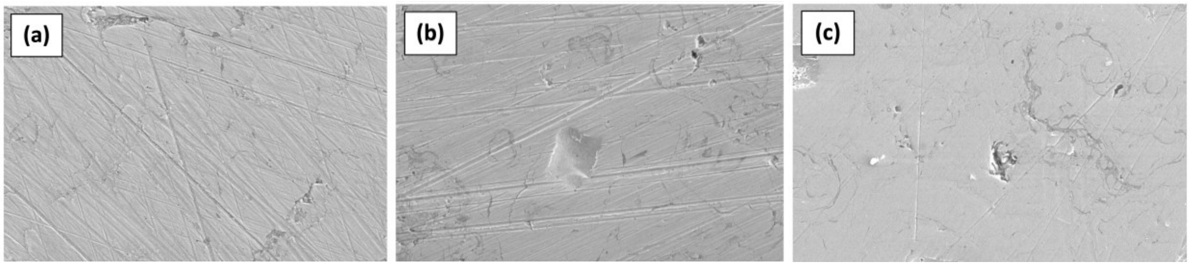

Fig. 16 SEM images of the coating surface of (a) cylinder bore samples, (b) bending samples grinded to 800-grit, and (c) bending samples grinded to 1200-grit.

The quasi-static and cyclic bending specimen dimensions are roughly 70 mm × 12 mm × 4 mm and shown in Fig. 17(a). It should be noted that the dimensions of each specific test specimen vary slightly from the prescribed dimensions. After testing, each fracture surface was evaluated using a microscope to determine the exact cross-sectional dimensions and coating thickness pertaining to each specimen. The samples are extracted from flat coated sheets in two orientations perpendicular to each other described as the W- and H-orientations, shown in Fig. 18(a) and (b) respectively. Fig. 17(c) highlights the rows and interface pattern location of the two orientations: in the W-orientation, the interface pattern can be seen on the long edge, while the rows of waves run along the shorter width of the sample, indicated in the red dotted lines. The H-orientation shows the pattern on the shorter width and rows run along the length of the sample.

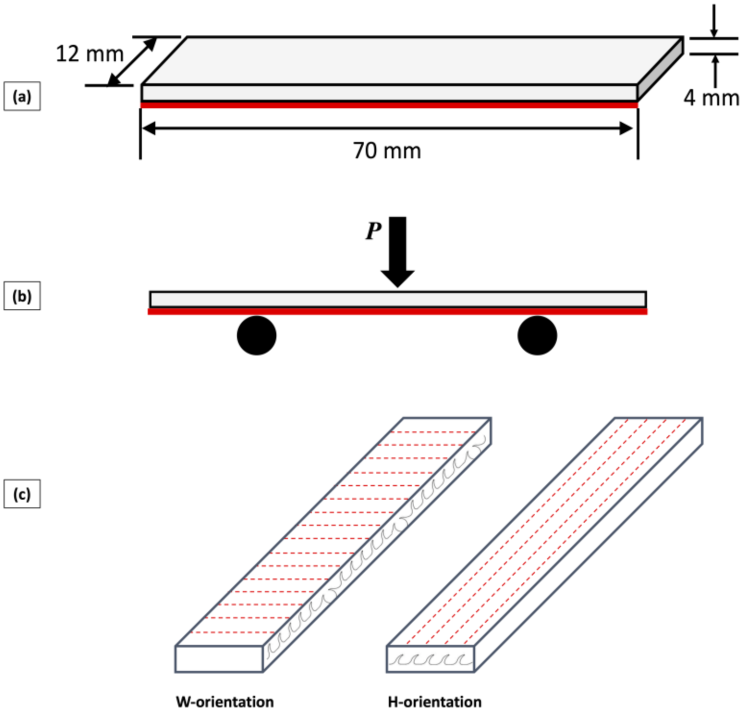

Fig. 17 Schematic with coating side indicated in red showing (a) bending specimen dimensions (b) three-point bending loading diagram, and (c) the two bending sample orientations extracted perpendicular to each other from the flat plates where the W-orientation shows the wave pattern on the long edge and the H-orientation with the pattern on the short edge and rows of wave that run vertically.

Fig. 18 Diagram of extraction from flat coated plates at two orientations: (a) W-orientation and (b) H-orientation.

This is to pinpoint the properties of the coating specific to the orientation of the mechanical roughening in the engine bore and the relevant loading that occurs during operation. The samples extracted in the two orientations are then painted to accommodate analysis using the digital image correlation (DIC) system. Quasi-static specimen were subjected to a white paint job with a black speckled pattern in order to accommodate strain measurements, whereas cyclic specimen are painted plain white Fig. 19. Very High Temperature (VHT) brand flame proof spray paint was used, which is appropriate for applications up to 1093°C.

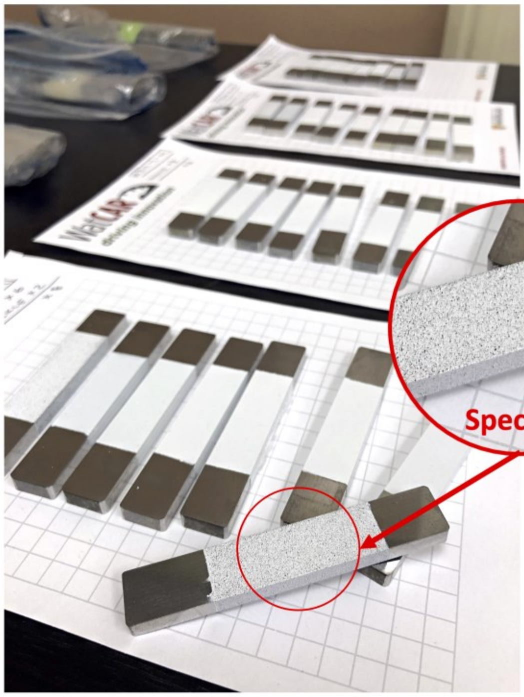

Fig. 19 Speckled samples for strain measurements in quasi-static tests and white samples without speckles for crack initiation detection in cyclic tests.

3.8.2 Bending Experimental Methods

The comprehensive testing plan includes all combinations available across the two substrate materials and two sample orientations (W, H), and the three temperatures of interest. This results in a total of twelve test categories, shown in Fig. 20. For quasi-static testing, two test repetitions within an acceptable variance range were performed for each category for a total of 24 tests, producing result values that average the two tests. Quasi-static testing was displacement-controlled using a ramp loading path with a rate of 1.00 mm/min.

Cyclic tests were force-controlled with a load ratio of R = 0.1 with a sinusoidal wave shape. While test continues to run until the entire sample (i.e., combination of coating and substrate) fails, the cycle where a visible crack initiates in the coating is identified by DIC is recorded as the life of the coating, which is the main area of interest. Lifespans of 1,000,000 cycles were considered run-out. Four to six load levels based off failure strength were used for each specimen category with two repetitions within an acceptable variance range for each load level. The failure strength was based off the results of quasi-static three-point bending studies on the same specimen categories and under the same testing conditions.

For all bending experiments, the Instron 8872 uniaxial (load capacity 25 kN) and Instron 8874 biaxial (load capacity 25 kN, torque capacity 100 N·m) test frames were used for RT testing. The MTS 810 (load capacity 50 kN) was used for elevated temperature testing with the Instron 3119-609 environmental chamber which is temperature rated for -100°C to 350°C. The three-point bending fixture was installed within the heated chamber and the GOM-ARAMIS 3D 5MP DIC device with two high resolution CCD cameras of 2448×2048 (5M) pixels resolution and frame rate 15 fps was used for quasi-static testing to capture the strain. For cyclic testing, the Correlated Solutions DIC device with two high resolution (5M pixel) CCD cameras (13 fps at full resolution) was used to determine the cyclic and location of crack initiation. The DIC's were required to operate outside the chamber during elevated temperature testing, with cameras pointed through the chamber's glass window for high temperature conditions. The complete quasi-static setup is shown in Fig. 21 (a different DIC for the cyclic setup). It is important to note that the two supports are on the coating side, while the load is applied to the non-coated substrate side of the sample to facilitate cracking on the coating side. The loading schematic is shown in Fig. 17(b), where the coated side of the specimen is indicated in red. SEM analysis was performed using the Zeiss Leo 1530 and UltraPlus FESEM (with EDX/OIM).

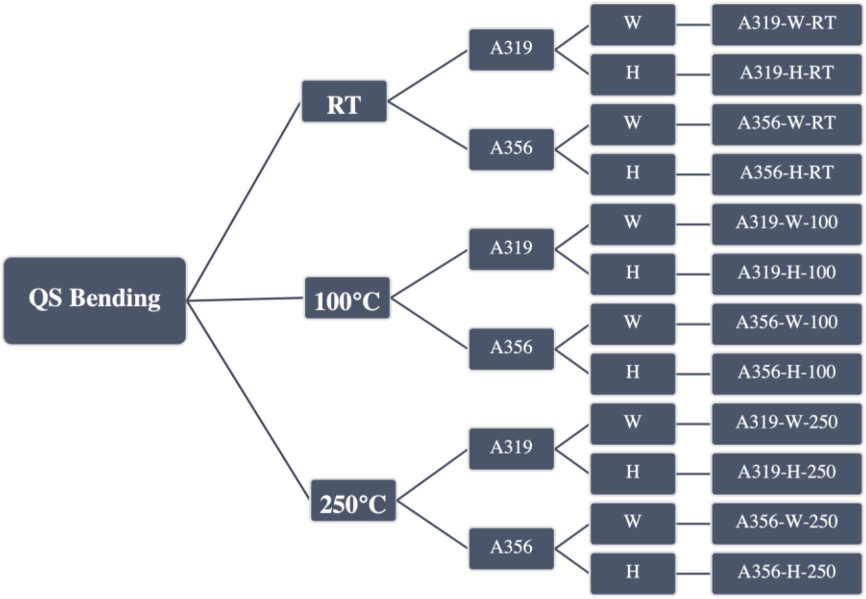

Fig. 20 Test plan showing the twelve combinations of the two substrates, two orientations, and three temperature conditions.

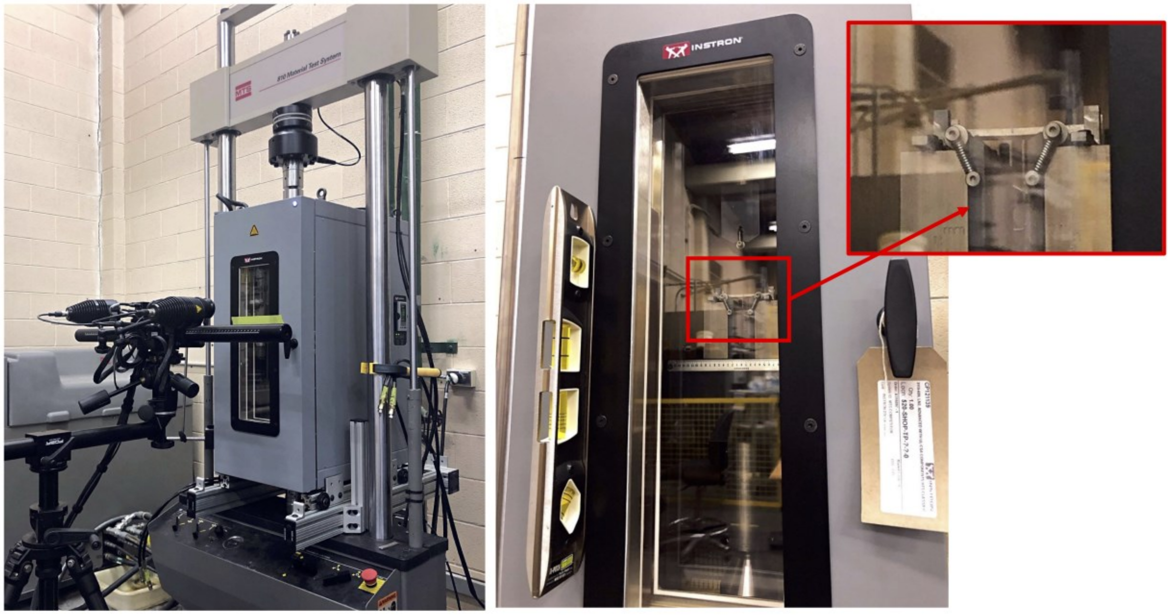

Fig. 21 MTS test setup for quasi-static elevated temperature testing including three-point bending fixture installed within the environmental chamber. The DIC device cameras are required to operate outside the chamber and through the chamber’s glass window.

3.8.3 Bending Analysis

The equivalent section method described in Section 3.7 Quasi-Static Bending Samples and Methods for Curved Cylinder Specimen is used to determine the maximum tensile bending stress at the coating surface from the maximum load in quasi-static tests. The same method is used to convert load levels in cyclic testing to stress at the coating surface. This is based on the cross-sectional dimensions measured of the fracture surface for each specimen.

Since the testing was not fully reversed (load ratio of R = 1) due to the nature of testing (i.e., bending), mean stress correction is necessary to transform the stresses to equivalent stress values with zero mean stress. Two mean stress correction methods were used for this conversion: Morrow and Smith Watson Topper (SWT). The Morrow method uses stress amplitude (σ_a), and failure stress in its conversion (σ_f) to determine the equivalent stress amplitude for fully reversed loading (σ_{ar}), shown in Equation 1. Stress amplitude is obtained from the aforementioned conversion from load amplitude to stress amplitude, while failure stress is obtained from the quasi-static study results for the particular specimen category (specific to the material, orientation, and temperature combination) [45]. The advantage of the SWT mean stress correction method (Equation 2) lies in the absence of material properties (i.e., σ_f in Morrow) as it uses only stress amplitude and maximum stress (σ_{max}) values, which are directly from the test loading.

$$\boldsymbol{\sigma_{ar} = \frac{1}{1-\frac{\sigma_a}{\sigma_f}}} \quad \textbf{(Equation 1)}$$

$$\boldsymbol{\sigma_{ar} = \sqrt{\sigma_{max}\sigma_a}} \quad \textbf{(Equation 2)}$$

The Basquin equation (power law relationship) can be used to describe the relationship between the fully reversed stress amplitude and coating life (which is linear on a log-log scale). Proceeding the mean stress calculation, the regression analysis yields the stress-life model, described in Equation 3 by the Basquin parameters $\sigma_f{}'$ and b, for each of the twelve specimen categories. Note that the life (N_f) in this model corresponds to the life of the coating as recorded by DIC crack initiation as opposed to the life of the coating and substrate together (i.e., entire sample).

$$\boldsymbol{\sigma_{ar} = \sigma'_f\left(2N_f\right)^b} \quad \textbf{(Equation 3)}$$

Chapter 4

Characterization of PTWA Coating on Cylinder Bores

The results presented in the current chapter are published as a journal paper in Surface & Coatings Technology in Volume 426, November 2021, 127757 (Fig. 22).

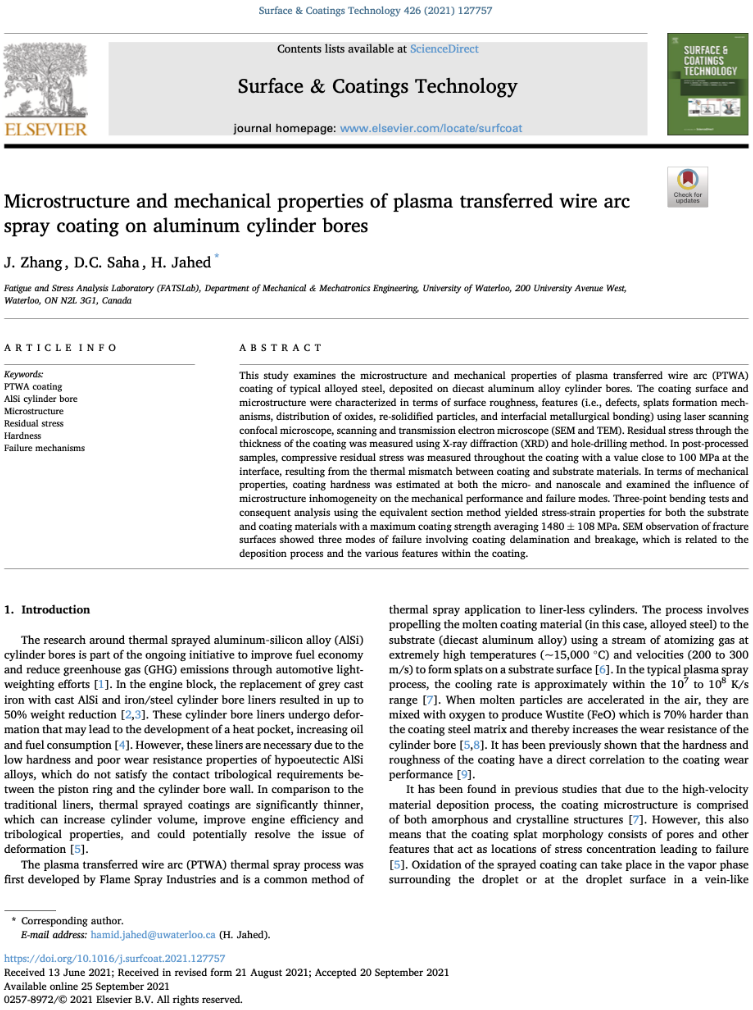

Surface & Coatings Technology 426 (2021) 127757

Contents lists available at ScienceDirect

Surface & Coatings Technology

journal homepage: www.elsevier.com/locate/surfcoat

Microstructure and mechanical properties of plasma transferred wire arc spray coating on aluminum cylinder bores

J. Zhang, D.C. Saha, H. Jahed [*]

Fatigue and Stress Analysis Laboratory (FATSLab), Department of Mechanical & Mechatronics Engineering, University of Waterloo, 200 University Avenue West, Waterloo, ON N2L 3G1, Canada

A R T I C L E I N F O

Keywords:
PTWA coating
AlSi cylinder bore
Microstructure
Residual stress
Hardness
Failure mechanisms

A B S T R A C T

This study examines the microstructure and mechanical properties of plasma transferred wire arc (PTWA) coating of typical alloyed steel, deposited on diecast aluminum alloy cylinder bores. The coating surface and microstructure were characterized in terms of surface roughness, features (i.e., defects, splats formation mechanisms, distribution of oxides, re-solidified particles, and interfacial metallurgical bonding) using laser scanning confocal microscope, scanning and transmission electron microscope (SEM and TEM). Residual stress through the thickness of the coating was measured using X-ray diffraction (XRD) and hole-drilling method. In post-processed samples, compressive residual stress was measured throughout the coating with a value close to 100 MPa at the interface, resulting from the thermal mismatch between coating and substrate materials. In terms of mechanical properties, coating hardness was estimated at both the micro- and nanoscale and examined the influence of microstructure inhomogeneity on the mechanical performance and failure modes. Three-point bending tests and consequent analysis using the equivalent section method yielded stress-strain properties for both the substrate and coating materials with a maximum coating strength averaging 1480 ± 108 MPa. SEM observation of fracture surfaces showed three modes of failure involving coating delamination and breakage, which is related to the deposition process and the various features within the coating.

1. Introduction

The research around thermal sprayed aluminum-silicon alloy (AlSi) cylinder bores is part of the ongoing initiative to improve fuel economy and reduce greenhouse gas (GHG) emissions through automotive light-weighting efforts [1]. In the engine block, the replacement of grey cast iron with cast AlSi and iron/steel cylinder bore liners resulted in up to 50% weight reduction [2,3]. These cylinder bore liners undergo deformation that may lead to the development of a heat pocket, increasing oil and fuel consumption [4]. However, these liners are necessary due to the low hardness and poor wear resistance properties of hypoeutectic AlSi alloys, which do not satisfy the contact tribological requirements between the piston ring and the cylinder bore wall. In comparison to the traditional liners, thermal sprayed coatings are significantly thinner, which can increase cylinder volume, improve engine efficiency and tribological properties, and could potentially resolve the issue of deformation [5].

The plasma transferred wire arc (PTWA) thermal spray process was first developed by Flame Spray Industries and is a common method of thermal spray application to liner-less cylinders. The process involves propelling the molten coating material (in this case, alloyed steel) to the substrate (diecast aluminum alloy) using a stream of atomizing gas at extremely high temperatures (~15,000 °C) and velocities (200 to 300 m/s) to form splats on a substrate surface [6]. In the typical plasma spray process, the cooling rate is approximately within the 10^7 to 10^8 K/s range [7]. When molten particles are accelerated in the air, they are mixed with oxygen to produce Wustite (FeO) which is 70% harder than the coating steel matrix and thereby increases the wear resistance of the cylinder bore [5,8]. It has been previously shown that the hardness and roughness of the coating have a direct correlation to the coating wear performance [9].

It has been found in previous studies that due to the high-velocity material deposition process, the coating microstructure is comprised of both amorphous and crystalline structures [7]. However, this also means that the coating splat morphology consists of pores and other features that act as locations of stress concentration leading to failure [5]. Oxidation of the sprayed coating can take place in the vapor phase surrounding the droplet or at the droplet surface in a vein-like

---

[*] Corresponding author.
E-mail address: hamid.jahed@uwaterloo.ca (H. Jahed).

https://doi.org/10.1016/j.surfcoat.2021.127757
Received 13 June 2021; Received in revised form 21 August 2021; Accepted 20 September 2021

Fig. 22 J. Zhang, D.C. Saha, H. Jahed, Microstructure and mechanical properties of plasma transferred wire arc spray coating on aluminum cylinder bores, Surf. Coatings Technol. 426 (2021) 127757 [45].

The porosity, oxide content, surface roughness, and hardness are important factors to consider as they are indicative of the coating quality, and affects coating properties/failure mechanisms. In this section, the microstructure of the coating and its interaction with the substrate at the interface are discussed. Coating properties are also analyzed by considering the residual stress through the coating and coating hardness.

4.1 Coating Characterization

Extensive microstructural characterization revealed various types of defects such as voids and pores, microcracks, re-solidified particles, and inter-splat oxides. Images of the coating with highlighted features is shown in Fig. 23, while detailed features images are shown in Fig. 24. Penetration of the steel coating into the substrate at the interface was also observed (Fig. 24(a)). Other instances showed an accumulation of particles identified at the bottom section of the dovetail geometry that often appear to be fragmented in nature.

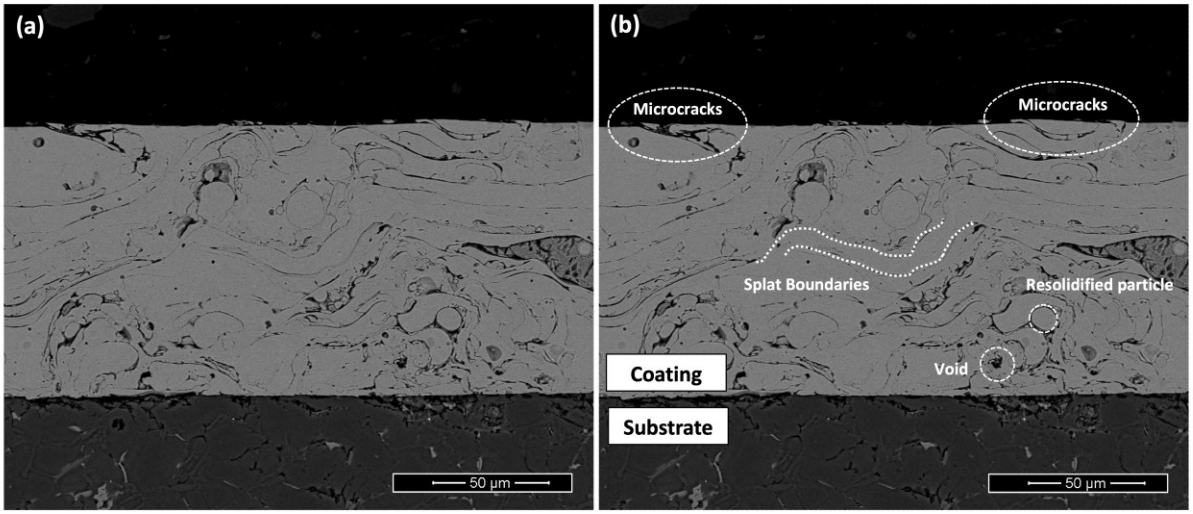

Fig. 23 BSE SEM microstructural images showing (a) the coating cross-section and (b) the same image with various features and defects outlined.

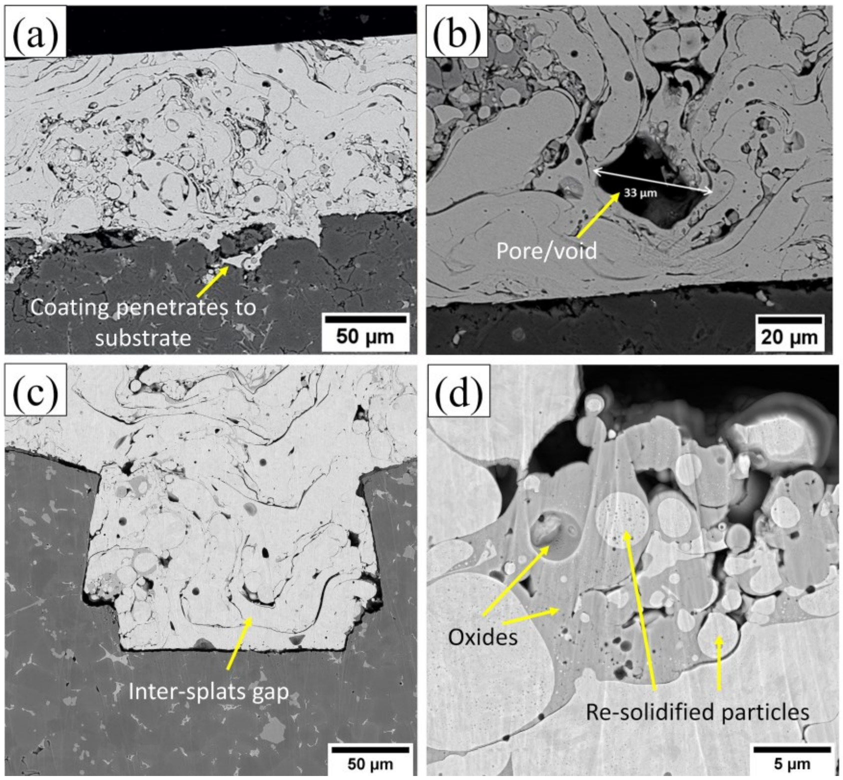

Fig. 24 BSE SEM microstructural images of coating cross-section showing various features and defects such as (a) coating penetration into the substrate, (b) pores/voids, (c) inter-splats gap and boundary oxides, and (d) oxides and re-solidified particles.

4.1.1 Splat Structure

The formation of coating splats is mainly related to the direction of the deposition process. The splat thickness and distribution will affect the adhesion and cohesion strength of the coating which has a prominent role in coating delamination. It was found that initially, the splats have a flat structure, but with the progression of subsequent splat deposition, heat build-up facilitates multiple splats combining to form a larger splat. Based on the splat formation observed in as-deposited samples shown in Fig. 25, three distinct regions within the coating were identified. These regions are mainly a result of the splat proximity to the interface pattern and whether the local effects of the interface are prominent. Adjacent to the substrate interface (Region A), the splats' thickness varies along each splat quite prominently, and splats mainly accumulate together at the bottom area of dovetails. In the middle section (Region B), the splats line up and numerous splats consolidate to form a longer splat. Finally, the top section (Region C), shows an area that is unaffected by local dovetail patterns, the major splats are uniform, and the distance/thickness between splats does not vary like Region A. It should be noted that the upper portion of Region C is typically machined off during the post-processing step.

The varying regions are mainly an artifact of the proximity of splat deposition to the interface pattern during the coating process. The more uniform coat quality described in Regions B and C are ideal; the accumulation of splats causing irregular splat thickness and orientation in Region A will result in the respective oxide boundaries to be irregular in both size and shape. Specifically in Region A, the presence of these irregular oxides has the potential to cause crack initiation, be included in the path of propagation, or cause cohesion failure within the coating.

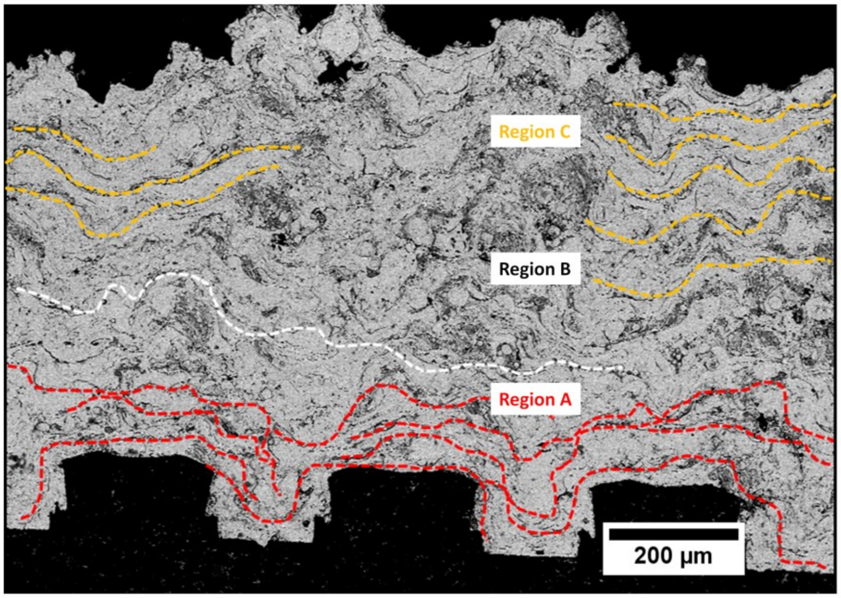

Fig. 25 BSE SEM image of as-deposited coating, showing three different splats formation regions.

4.1.2 Resolidified Particles and Pores

While it was determined that pores or voids were uncommon, few were still present within the coating and interfacial area. Fig. 24(b) shows an example of a larger void within the coating which measures 33 µm, diagonally. Voids were identified as regions lacking in notable elemental composition during EDX analysis. These regions can be recognized easily by the darker shades in SEM images, but also being irregular in their shape. Dark shapes that are more circular are artifacts of the sample preparation method (i.e., hot mounted resin), and are not indicative of void features. The concerns regarding voids are related to their role as potential crack initiation sites as well as an indication of poor metallurgical bonding between the splats. Since thermal spray coating is conducted in the air, oxidation and chemical reactions occur during coating deposition.

Re-solidified particles, shown in Fig. 26, are undesirable as they can act as stress concentration sites and facilitate oxide formation at their boundaries. The size distributions and locations of re-solidified particles contribute to the final fracture modes and failure mechanisms under static and dynamic loading. The presence of the re-solidified particles adjacent to the dovetail profile wall (i.e., at the vicinity of coating/substrate interface) represents poor coating/substrate metallurgical bonding and may lead to sharp interface separation. On the other hand, the re-solidified particles at splats and splat boundaries have limited contribution to the final fracture mode. Fig. 26(a) depicts the re-solidified particle size and distribution relative to the position on the dovetail profile, combining five images taken from different locations overlaid. For comparison, Fig. 26(b) shows a similar size and distribution overlay that highlights the voids present in the coating. Most particles, while smaller in size, accumulated at the top location (Region C, as shown in Fig. 25) of the dovetail, and fewer but larger particles are located at the bottom location (Region A). The overall size distribution of the particles is described in Fig. 26(c), where more than 200 particles within the coating were measured, indicating that most particles fall within 6 to 10 μm diameter range. The area fraction that accounts for re-solidified particles is 2.03% of the coating, as estimated by using Keyence VHX-7000 communication software.

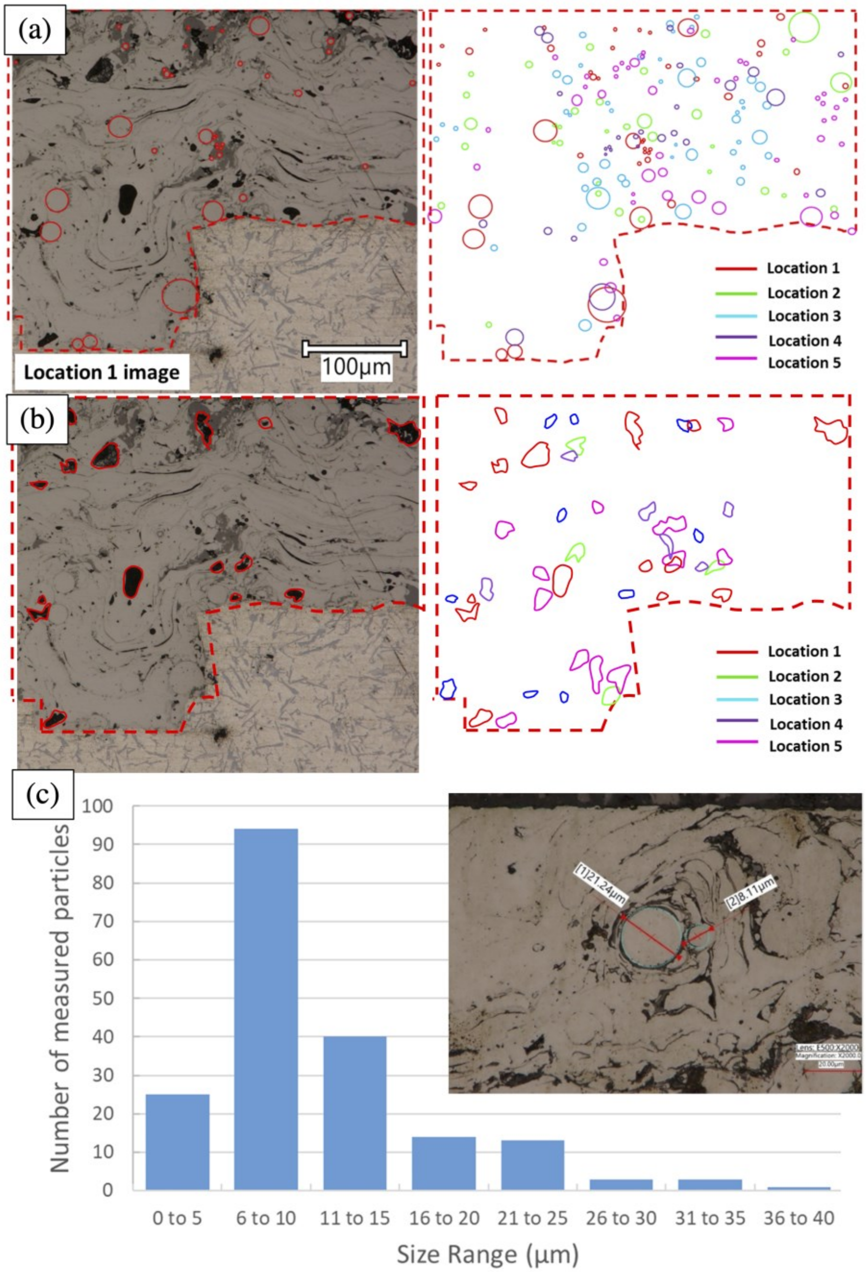

Fig. 26 Optical images showing the morphology and locations of the (a) re-solidified particles, (b) voids, and (c) the size range distribution of re-solidified particles.

4.1.3 Oxides

When the molten metallic particles oxidize in air, oxides shells are formed at the boundaries (Fig. 24(c) and (d)). These areas are identified as regions of oxides due to the high oxygen content in the elemental composition reported during EDX analysis. The inter-splat gap or outline is mostly oxide inclusions or a network of oxides that formed during in-flight oxidation. Additionally, the surface of solidifying splats is further oxidized by surrounding oxygen before being covered by the next arriving droplet particles. Therefore, two types of oxidation occur during the deposition: (a) oxidation of molten droplet shell in-flight before impacting on the substrate, and (b) post-impact oxidation which mainly occurs due to the time lag between each successive splat deposition. The latter oxidation is negligible compared to the former one, as the time lag between the successive splats (10-20 μs) is much shorter than two successive passes (a few seconds) [46,47]. The higher in-flight oxidation time produced a high volume of oxide shell around the re-solidified particles which can be seen in Fig. 24(d) compared to a very thin oxide outline between the splats as shown in Fig. 24(c). A large amount of oxide phase is expected in the thermal spray coating since oxides make the coat harder and more wear resistant. However, the oxides may deteriorate the strength, corrosion, and machinability of the coating. The distribution of the oxide layer is dependent on the coating deposition parameters. For example, a better distribution of oxides has been reported when spindle revolution speed increase from 400 to 600 min^{-1}[4]. Since oxides surround the various features of the coating (i.e., splats, re-solidified particles), the structure and distribution of said features are directly related to that of the oxides.

4.2 Interface Characterization

To investigate the metallurgical bonding between the steel coating and Al substrate, a TEM membrane was prepared using the FIB method from the lower region of the dovetail. Fig. 27(a) shows a SEM image of the region of interest comprised of equal coating and substrate regions. The prepared FIB sample was observed under TEM and a very sharp coating/substrate interface was found without the presence of intermetallic compounds (IMCs), as shown in Fig. 27(b). The enlarged view of the coating/substrate interface (Fig. 27(c)) exhibits several features such as dislocation pile-up at the steel coating due to rapid solidification, and lattice strain because of the phase transformation. On the Al substrate side, several shear bands were identified which are believed to have been induced during the dovetail pattern cutting process. Upon coating deposition, heat build-up occurs very quickly at the Al substrate, which favors the recrystallization process. Therefore, several recrystallized Al grains can be observed as highlighted in Fig. 27(c).

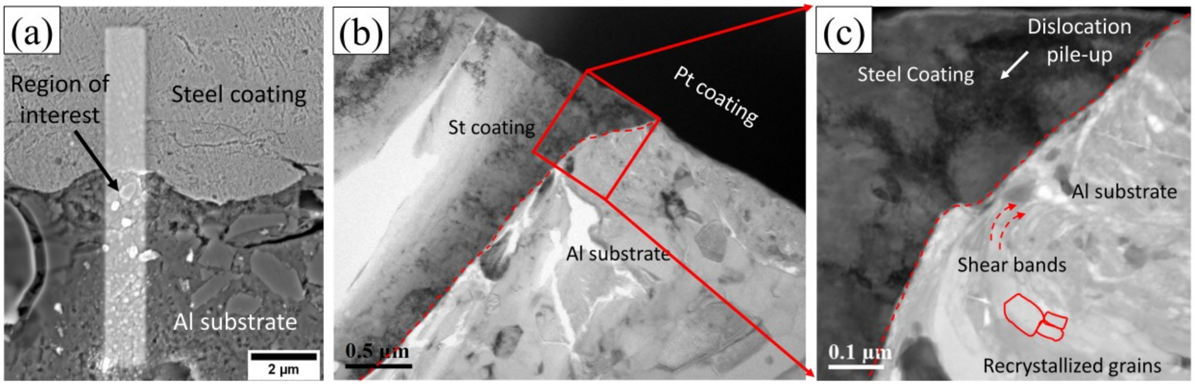

Fig. 27 (a) Interface selection for TEM membrane preparation using FIB method, (b) bright-field TEM image of steel coating and Al substrate interface, and (c) enlarged view of the rectangular area on (b).

The energy dispersive x-ray spectroscope (EDX) analysis of Fe, Al, Cr, O, and Si elemental distributions are presented in Fig. 28. No visible Fe-Al IMC layer was identified, which may suggest that the solidification rate was so rapid that the potential diffusion of Fe and Al atoms was restricted. Usually, the IMCs are brittle and have a low resistance to cracking, leading to early crack initiation under mechanical loading. Although no IMCs were detected, traces of steel coating could be seen on the Al substrate and is likely related to the mechanical interlocking. The absence of an IMC layer was further confirmed by EDX line scanning across the coating/substrate interface as shown in Fig. 29, where no identifiable IMCs were detected. Lack of IMCs may be due to the high solidification rate of the deposited coating which did not provide enough time for diffusional phase transformation.

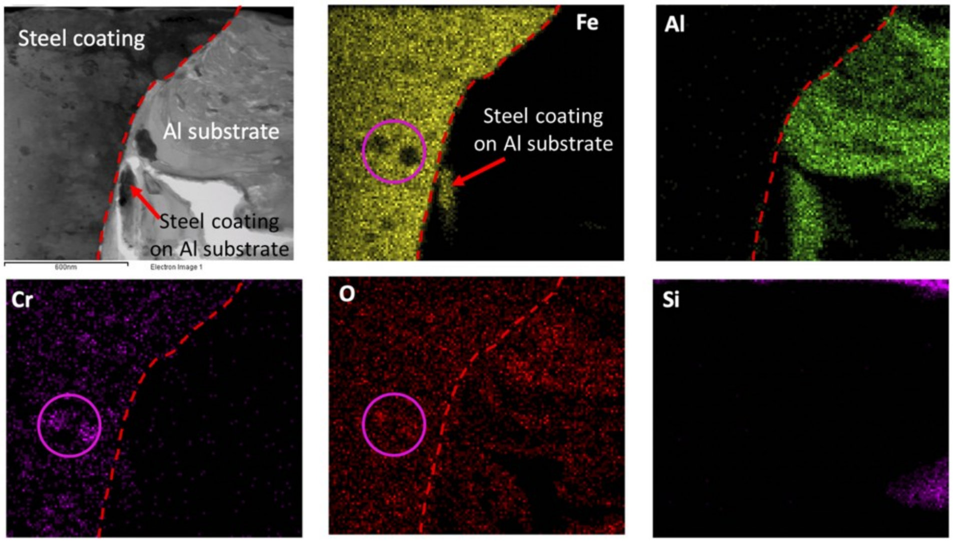

Fig. 28 Bright-field TEM image of the interface with EDX elemental mapping of Fe, Al, Cr, O, and Si.

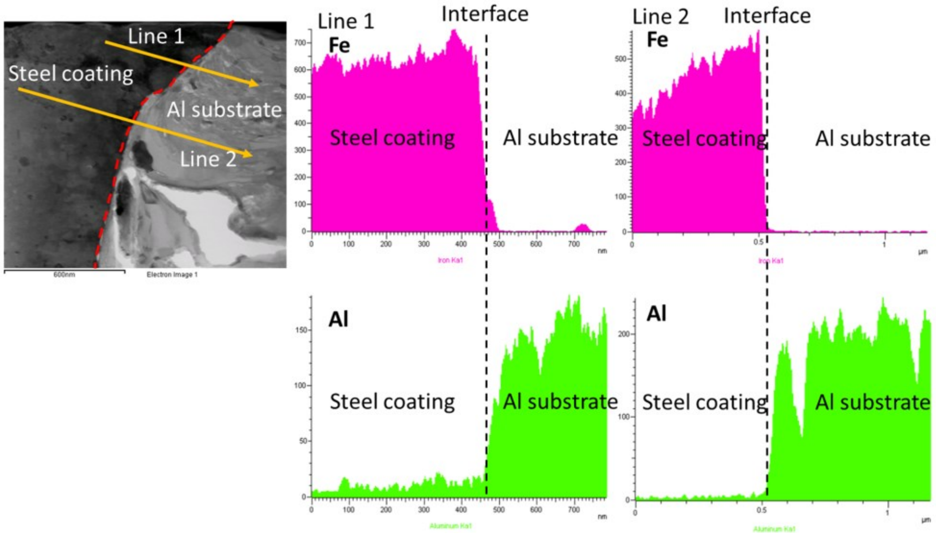

Fig. 29 EDX line scanning across the steel coating and Al substrate interface.

4.3 Surface Roughness

Surface roughness is an important coating property to determine since it plays a crucial role in the wear performance of the coating. As expected, as-deposited coatings, which are rough to the touch, had a considerably higher average surface roughness (R_a) value of 18.5 µm. The roughness significantly decreased after diahon and machining processes since both samples had a mirror-like surface finish: R_a values were 0.17 µm and 0.14 µm, respectively. Similarly, the difference between the tallest peaks and deepest valleys (R_Z) was measured to be 149.3 µm for the as-deposited sample, and 8.44 µm and 6.4 µm for diahon and machined (Fig. 30). As a result, diahon and machined surfaces are expected to have better tribological properties compared to the as-deposited structure.

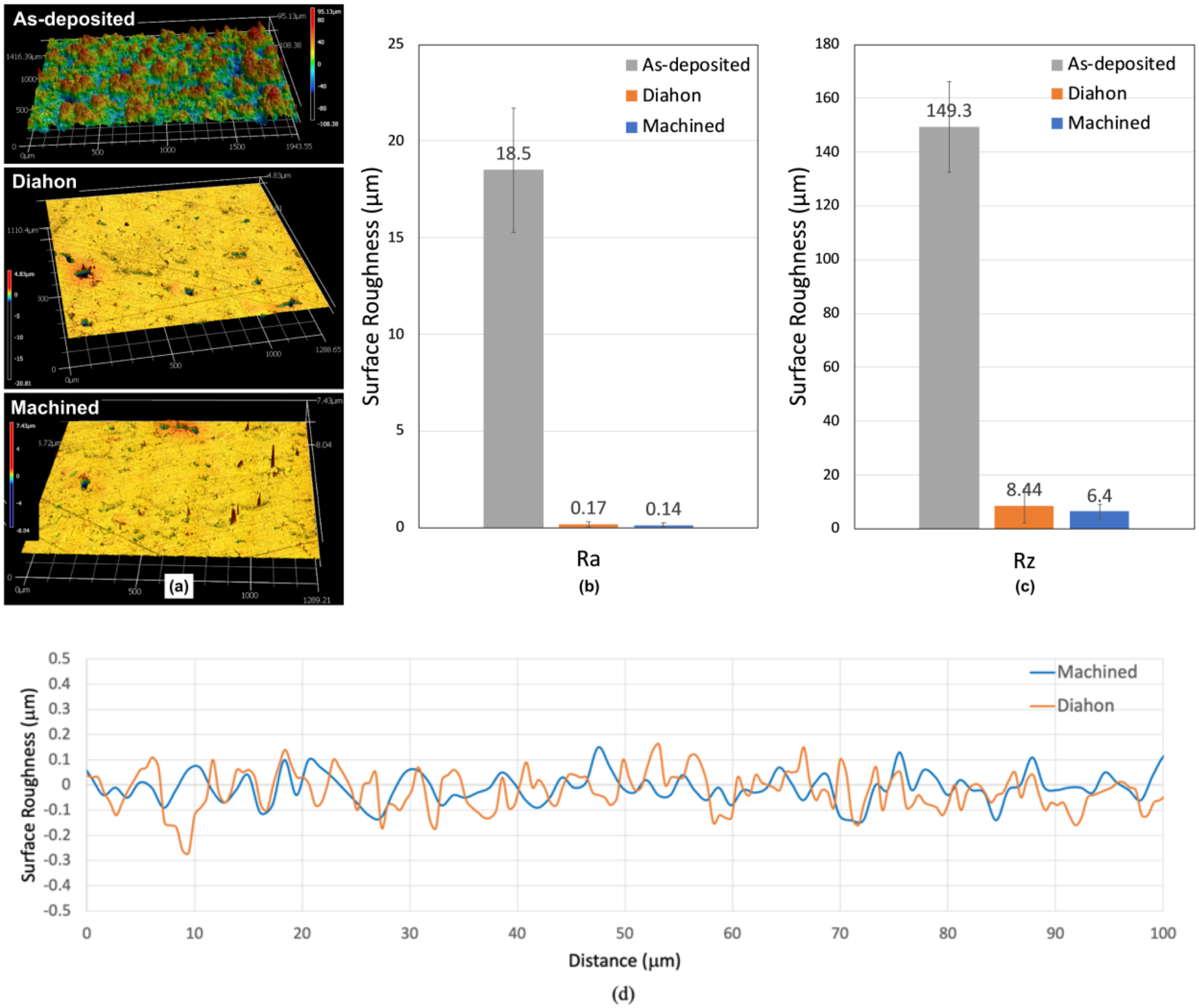

Fig. 30 Comparison of as-deposited, diahon, and machined samples in terms of (a) surface roughness, (b) average surface roughness (R_a), (c) difference between tallest peaks and deepest valleys at the surface (R_Z), and (d) trace of surface roughness line profiles excluding large pores.

4.4 Residual Stress

The RS distribution throughout the coating thickness was measured using the XRD peak broadening method. Results for the two post-processed samples (i.e., machined and diahon) yielded compressive

RS in the range of -500 MPa at the coating surface (Fig. 31). The RS trend approached zero through the thickness of the coating and approaching the interface (Fig. 31). However, for the as-deposited sample shown in Fig. 32, the resulting trend was different: RS at the surface is essentially zero and while the stresses vary between compressive and tensile through the thickness, they are of low magnitudes that can be considered near zero up to 200 μm thickness where it shows a small compressive residual stress. Unlike post-processed samples, the stresses do not reach a value greater than -150 MPa (Fig. 32). This implies that the post-processing (i.e., machining/grinding and honing) induces a considerable amount of compressive RS.

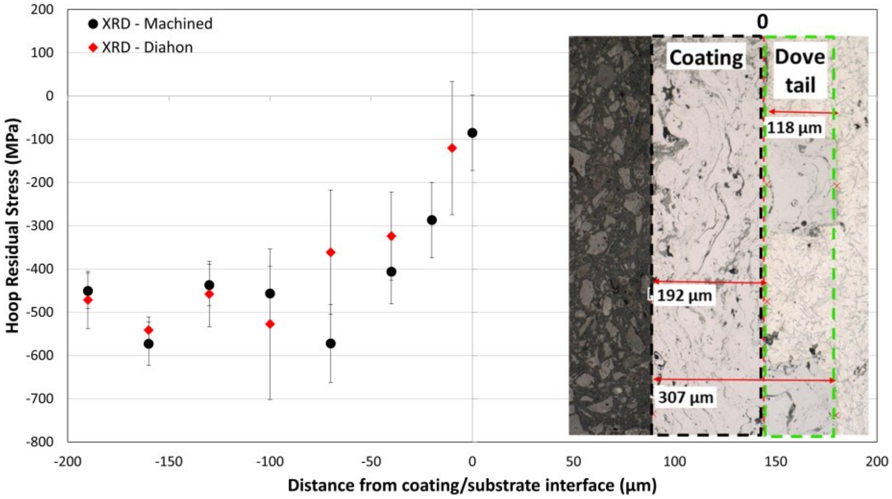

Fig. 31 XRD residual stress distribution across the machined and diahon coatings.

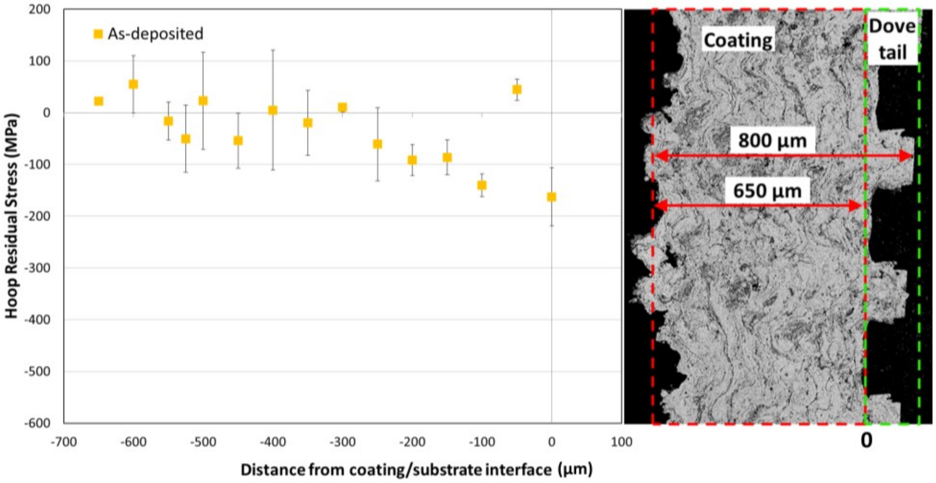

Fig. 32 XRD residual stress distribution across the as-deposited coating.

The results of the RS evaluation using the hole drilling method (machined and diahon) along with the XRD results are plotted together in Fig. 33. Like the XRD results, the coating and substrate regions are divided by the y-axis, but the area right of this represents the height of the dovetail region. At the interface, this region contains both steel and Al, shown in Fig. 33 inset. As a result, within this region where both materials are present and alternating, there are uncertainties in the RS calculations, which are intended for single material consideration. Overall, outside the dovetail region, the following conclusions about RS can be made from the hole-drilling results: (1) RS in the coating is compressive, (2) RS value ranges from -600 to 200 MPa, and (3) beyond the depth of 200 μm in the substrate, there is small RS that can be considered close to zero.

These results are consistent with those obtained by the XRD method, which ensures they are independent of sample preparation and measurement method. The compressive RS at the interface in the as deposited coating can be attributed to the thermal mismatch between steel and aluminum. Due to the extremely high temperature (~15,000°C) of the deposition process, the large thermal deformation of the substrate relative to the coating will cause the surface of the coating to experience compressive stress. Since lower compressive stress values were measured within as-deposited samples, it was found that the compressive RS is accentuated to a higher degree by the post-processing that occurs. It has been identified through extensive High Angular Resolution Electron Backscatter Diffraction and Transmission Electron Microscopy analysis along with XRD $\mathrm{Sin}^2\psi$ technique [48] that the RS value at the substrate immediately below the splats is tensile in nature, which is confirmed in the current investigation. The RS transition from highly compressive at the coating surface to the little tensile at coating/substrate interface was reported to be the combined effect of stress-relieving phenomena (edge curling) and low splat-substrate adhesion due to the heterogeneous nucleation over an oxidized surface [48,49].

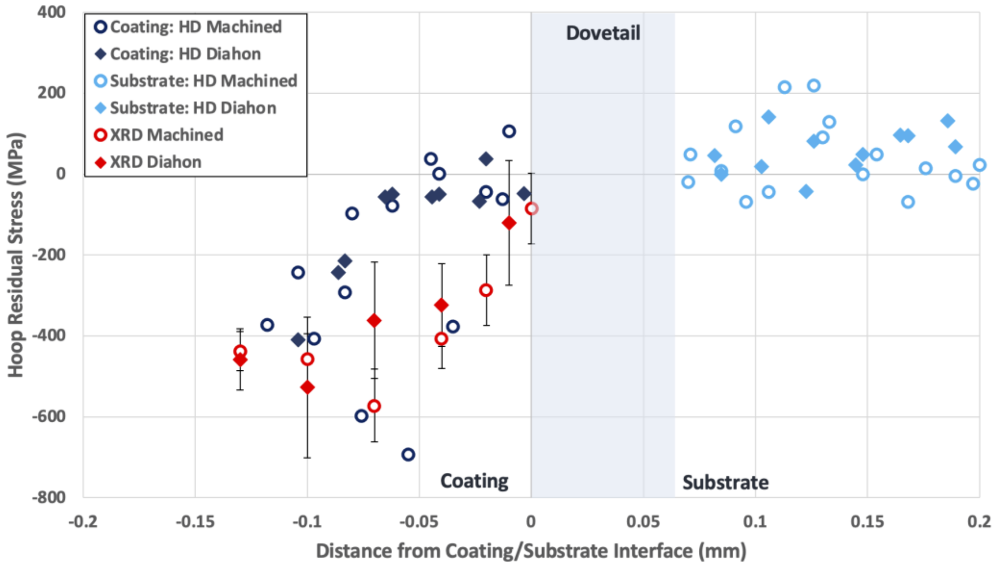

Fig. 33 Residual stress distribution across the coatings using hole-drilling method and XRD methods, and substrate using hole-drilling for machined and diahon samples.

4.5 Coating Hardness

Vickers micro-hardness and nano-indentation studies were conducted to determine the local mechanical properties of the coating, interface, and substrate. Overall coating hardness is important to evaluate as it will directly contribute to the wear resistance properties of the coating. The hardness distribution within the coating is also a crucial consideration since locations of higher hardness surrounded by lower hardness areas can cause failure within the coating, affect the mechanical properties, and potentially change failure modes related to interface bonding. The plot of micro-hardness as a function of distance from the coating/substrate interface for the post-processed samples is shown in Fig. 34. The results showed the average hardness of the Al substrate was around 95 ± 3 HV, while micro-hardness within the coating varied from 200 to 450 HV. The large micro-hardness deviation in the coating can be attributed to the various coating features. The coating has a composite-like structure, featuring a combination of hard and soft phases. Since these microstructural features are much smaller in size than the micro-hardness impressions, the hardness value will differ depending on the combination of features present within the indented region. As a result, three categories of coating hardness were identified as highlighted in Fig. 34: (i) indentation partially or fully within the splats with 200-300 HV, (ii) indentation comprising both splats and oxides with 300-400 HV, and (iii) indentation partially within oxides with 400-500 HV. The hardness within the splat is expected to be relatively low, whereas oxides are expected to have high hardness values, considering FeO (wüstite) is 70% harder than the steel matrix [7].

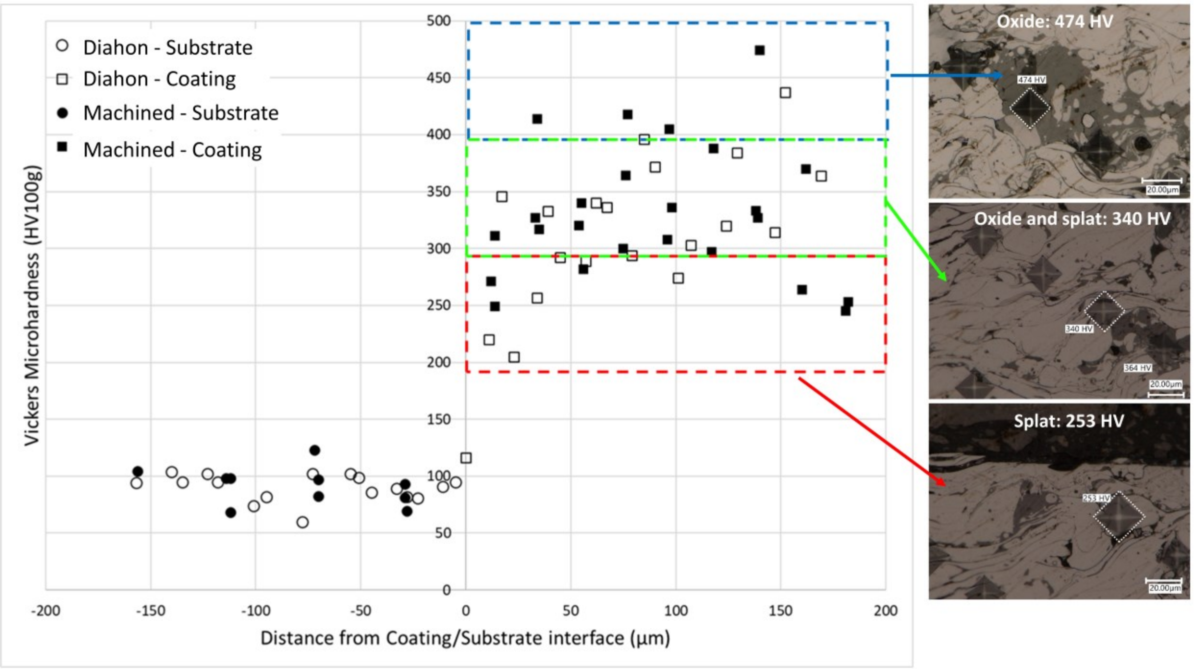

Fig. 34 Vickers micro-hardness distribution across the coating thickness of the post-processed samples.

While micro-hardness testing is important in determining the overall hardness of the materials, the hardness of the microstructural features can be better resolved using nano-indentation techniques due to the nanometer-range indenter size. It was found that the nano-hardness within a re-solidified particle was about 500 HV, and the same three categories evaluated in micro-hardness tests are as follows: (1) 150-250 HV, (2) 250-400 HV, and (3) 400-700 HV. When comparing the results (Fig. 35) of the three regions from micro and nano-indentation, the hardness values are within a more localized region and it can be concluded that these values accurately describe how splats and oxides contribute to the lower and higher hardness values, respectively. Micro-indentation results provide a better representation of hardness values when considering the overall coating and its features as a whole, while localized values obtained by nano-indentation have identified areas of high hardness and potential failure sites. Specifically, the crack initiation and propagation may follow the path of the irregular high hardness values within the coating, which were identified to be oxide-rich regions. Similarly, cohesion issues within the coating will occur when the coating bonding is weaker than interfacial bonding, which is again dependent on the coating microstructure and corresponding hardness.

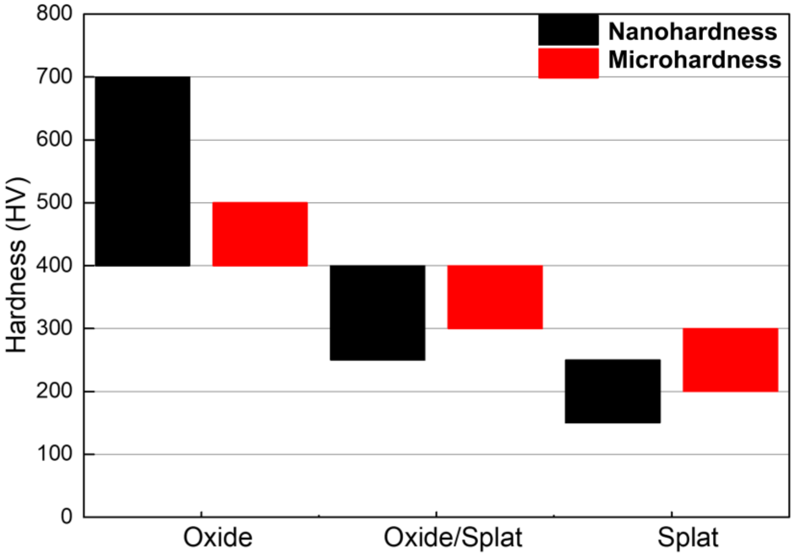

Fig. 35 Comparison of micro- and nano-hardness ranges on oxide, oxide/splat, and splat regions.

Chapter 5

Adhesion Properties of PTWA Coating

5.1 Experimental Bonding Strength

Five tests for each of the interface patterns were conducted on the A319 substrate, with the addition of three supplementary wave pattern tests on the A356 substrate. The load and stress data for each specimen, average stress for each sample type, and standard deviation are shown in Table 4.

Table 4 Stress results of bending testing with qualitative failure description

Pattern/Substrate Type	Test	Stress	Average Stress	Standard Deviation	Failure Description[1]	Fracture Surface
D319	01	1.25	0.96	0.84	A, C	Smooth
	02	-0.13			A, C, E	
	03	-0.58			A, C	
	04	1.57			A, C	
	05	1.55			A, C, E	
W319	06	-0.84	-1.04	-1.11	A, C	Mild cohesion issues
	07	-0.35			A, C	
	08	-0.45			A, C	
	09	-1.50			A, C, E	
	10	-0.72			A, C, E	
W356	11	0.04	0.08	0.26	A, C	Prominent cohesion issues
	12	0.93			A, C	
	13	-0.77			A, C	

[1] Failure observed, including adhesion (A), cohesion (C), and epoxy (E)

In addition to the load and stress data, there were clear qualitative trends observed in the three specimen types. Even when inspected by the naked eye, the fracture surface of the D319 (dovetail dovetail) samples were smooth and shiny (to varying degrees). The W319 and W356 (wave) samples were more similar – splotches of coating remnants were obvious across the fracture face. Fig. 36 shows camera images of the fracture surfaces of four samples. Fig. 36(a) and (b) show D319 substrates which are shiny and smooth relative to the others. Fig. 36(c) and (d) show the W319 and W356 samples, which there is an uneven distribution of coating remaining, indicating that there has been failure within the coating (cohesion failure) as opposed to at the interface (adhesion failure). It is also clear that the W319 sample in Fig. 36(c) has experienced milder cohesion issues when compared to (d), where a more significant amount of coating remains. Previous quasi-static adhesion tests in literature suggested that coating/substrate failure is mainly due to adhesion failure [4], which is what is predominantly seen by the dovetail pattern samples (D319). Other studies in literature reported failure due to cohesion [9], which has been seen by the wave pattern samples (W319 and W356).

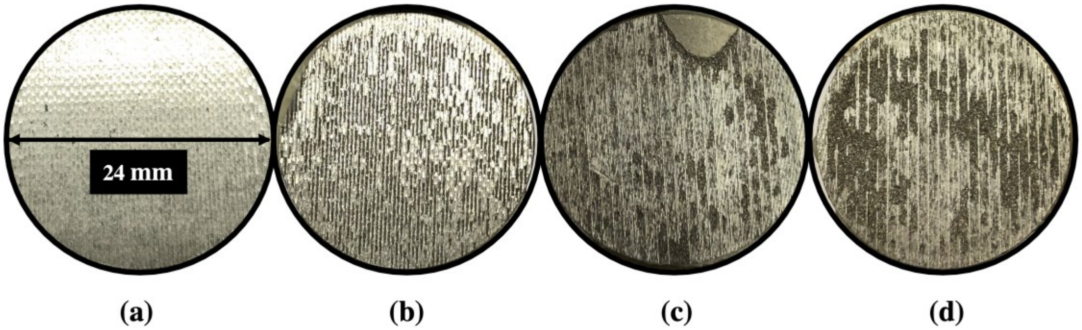

Fig. 36 Camera images comparing the fracture surfaces of (a) D319-03, (b) D319-04, (c) W319-09, and (d) W356-13.

When comparing the two D319 images, Fig. 36(a) shows a sample with the lowest recorded maximum stress, and (b) with the highest maximum stress. The SEM images at ×50 magnification of the same two samples are shown in Fig. 37(a) and (b) where examples of coating remnants are highlighted in yellow. Though both are D319 samples, the degree of cohesion issues is clearly different – Fig. 37(a) D319-03 experiences a lower maximum stress (28.83 MPa) and has only a few spots of coating, whereas Fig. 37(b) D319-04 experiences higher maximum stress (43.18 MPa) and has a considerably amount of coating breakage. The coating thickness and location is better observed in the side cross-sectional images shown in Fig. 38(a) and (b). Lack of interlocking at the interface will result in a relatively clean adhesion breakage at that location. When there are cohesion issues, it is an indication that the interlocking is successful. Since we see more coating breakage and successful interlocking in D319-04, it also experiences a higher maximum stress before failure. It is also clear that effective interlocking of the coating occurs within the lower portion (or "wells") of the dovetail pattern.

Similarly, when comparing the W319 and W356 results from Table 4, the lower average maximum stress of W319 corresponds to the lesser degree of cohesive coating breakage shown in Fig. 37(c) and Fig. 38(c), versus the W356 with higher degrees of coating in Fig. 37(d) and Fig. 38(d). Overall, in W319 samples, the separation due to adhesion failure was greater than coating cohesion breakage. W356 samples experienced similar amounts of adhesion failure and cohesion coating breakage. While mechanical interlocking is successful in both cases of the wave pattern, it is more prominent in the W356 sample.

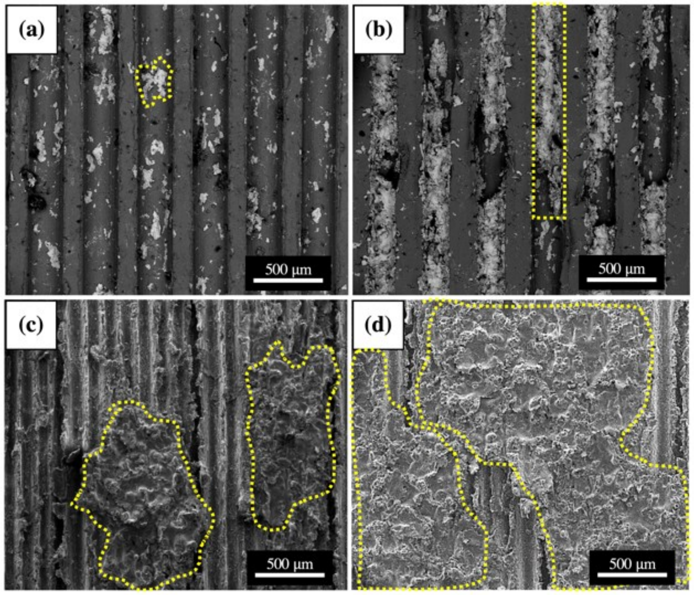

Fig. 37 SEM images at x50 magnification comparing the fracture surfaces of (a) D319-03, (b) D319-04, (c) W319-09, and (d) W356-13, with examples of coating remains highlighted.

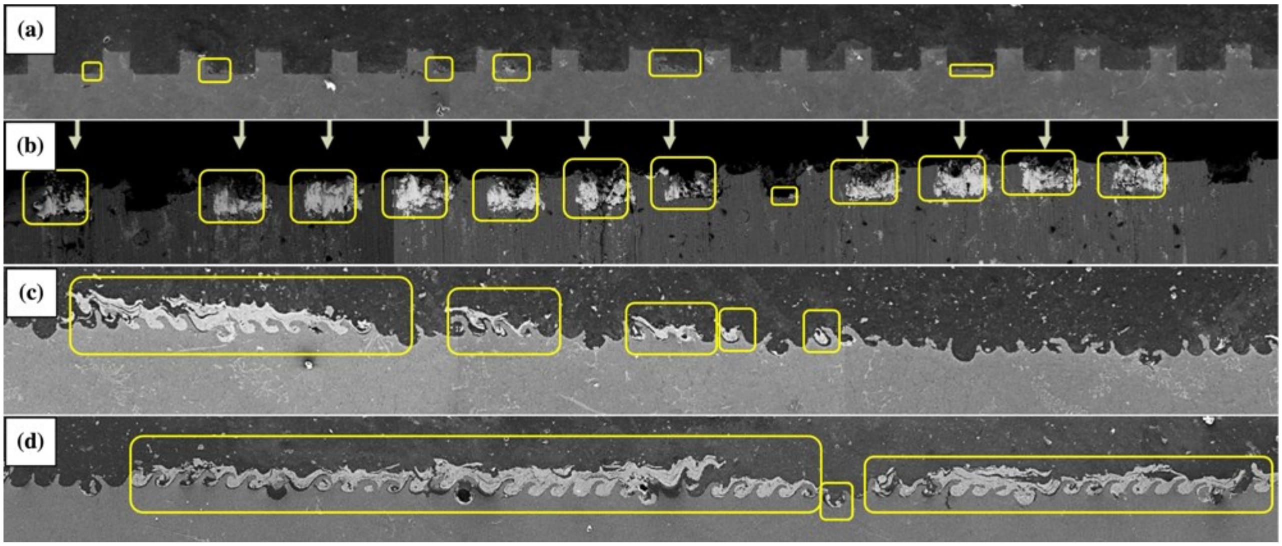

Fig. 38 SEM images comparing the side cross sectional view of (a) D319-03, (b) D319-04, (c) W319-09, and (d) W356-13, with examples of coating remains indicated in yellow.

Based on the severity of deformation, five levels were devised as follows: (D0) No deformation, (D1) Mild deformation, (D2) Medium deformation, (D3) Heavy deformation, and (D4) Fracture. Mainly the heaviest two degrees of deformation, D3 (heavy) and D4 (fracture) were observed in the dovetails, shown in Fig. 39(a). The entire range of deformation severity was identified on wave samples, shown in Fig. 39(b). Generally, the degree of deformation is associated with the failure type – heavier deformation results in adhesion failure since mechanical interlocking is weaker, and milder deformation sees cohesion failure since the coating fails before considerable deformation occurs. The relationship between the degree of deformation seen and the failure mechanisms is discussed in Section 5.3 Fracture Mechanisms.

At the fracture surface of the aluminum substrate, textured areas were found in both the dovetail and wave samples, existing at the bottom region of the geometry. EDX analysis revealed that these areas may indicate the presence of Iron Aluminum intermetallics (Fe-Al IMCs), displayed in Fig. 40.

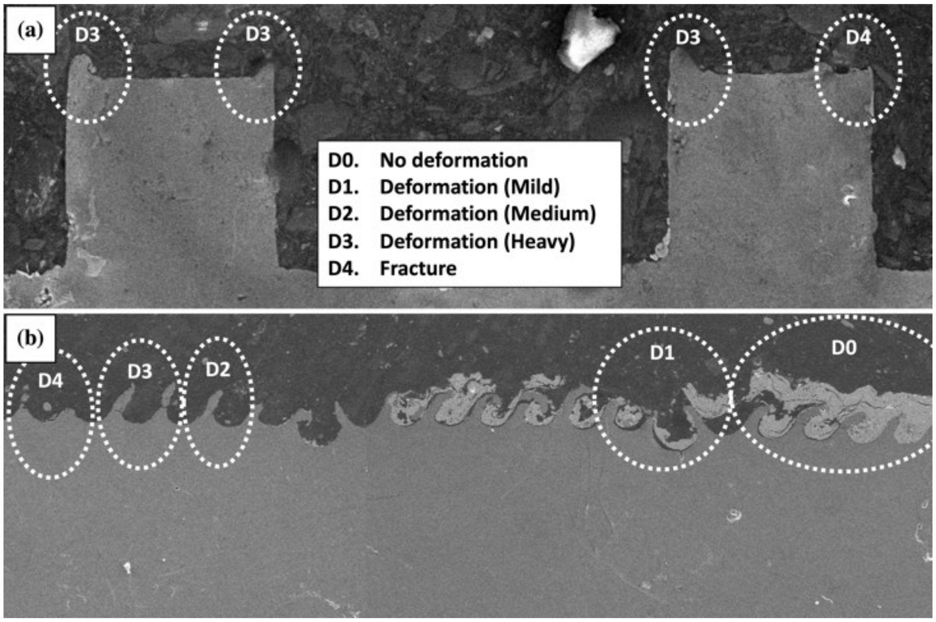

Fig. 39 SEM images highlighting the degrees of mechanical deformation of (a) dovetail, and (b) wave interface patterns.

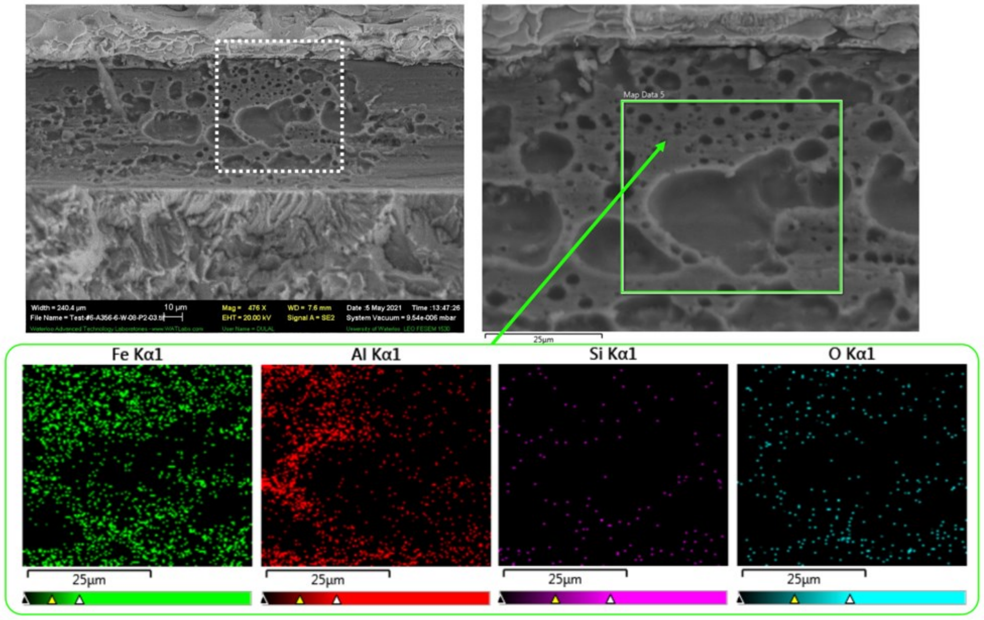

Fig. 40 EDX elemental analysis of the textured regions showing Fe, Al, Si, and O distribution.

5.2 Coating Strength Simulation

Results of the simulations yielded maximum stress values of 50 MPa for the dovetail drawing, 10 MPa for the wave drawing, and 34 MPa for the wave SEM image. Stress is calculated from the maximum force during the applied separation, divided by the adhesion area. Since it is extremely apparent that the ideal wave drawing (Fig. 12(b)) is not an accurate representation of the wave pattern observed on the specimen (Fig. 12(c)), this model was not considered in further analysis. The discrepancies arise from the irregular deformation that the waves are subjected to during the splat deposition process of the coating. This was mirrored in the results of the wave drawing deviated so much from experimental and expected values. The stress versus separation curve is shown in Fig. 41(a).

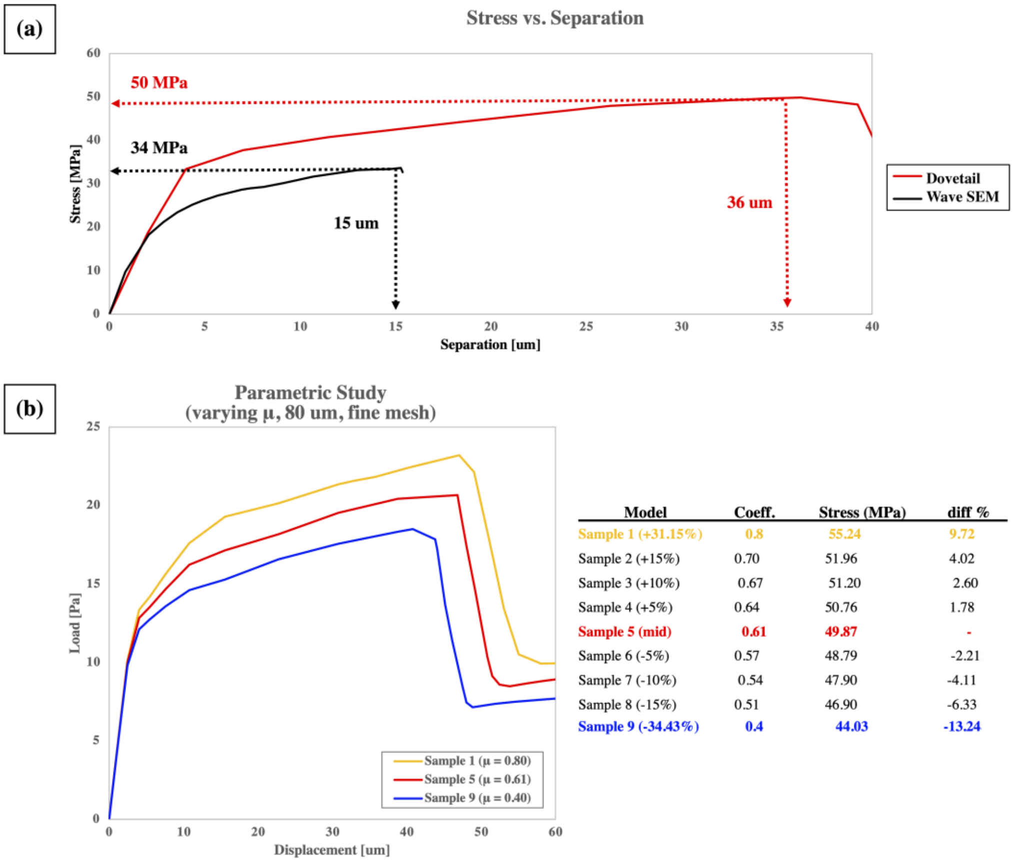

Model	Coeff.	Stress (MPa)	diff %
Sample 1 (+31.15%)	**0.8**	**55.24**	**9.72**
Sample 2 (+15%)	0.70	51.96	4.02
Sample 3 (+10%)	0.67	51.20	2.60
Sample 4 (+5%)	0.64	50.76	1.78
Sample 5 (mid)	**0.61**	**49.87**	**-**
Sample 6 (-5%)	0.57	48.79	-2.21
Sample 7 (-10%)	0.54	47.90	-4.11
Sample 8 (-15%)	0.51	46.90	-6.33
Sample 9 (-34.43%)	**0.4**	**44.03**	**-13.24**

Fig. 41 Plots showing (a) stress versus separation curve for dovetail drawing (red) and wave SEM (blue) models, and (b) parametric study where the static friction coefficient is varied.

A parametric study was performed on the dovetail model to examine the sensitivity of the results particularly to the static coefficient of friction used to describe the interaction between the materials at the interface (Fig. 41(b)). It was found that there is under 0.45% change in maximum stress per 1% change in the coefficient value. Overall, there is a percent difference in maximum stress ranging from -13.24% to 9.72% for coefficient values of 0.4 to 0.8, respectively. This indicates that the model results can change by a considerable amount if the static friction coefficient were to greatly deviate from the value of 0.61 that is used.

The simulated analysis also presents several limitations. The model of the dovetail pattern resembles the SEM interface image shown in Fig. 42(a), but occasional irregularities are not accounted for along and through the dovetails. Similarly, the wave pattern model shown in Fig. 42(b) describes an example of the types of irregularities that occur at the interface (i.e., along the waves), however it also does not account for variance through the depth of each row. The variance through the depth of the rows can be seen in the dovetail fracture face SEM image shown in Fig. 42(c). In both models, the layered splat structure and various features of the coating are not modelled. It has been observed in experimental results that breakage within the coating is varied and heavily dependent on features. Breakage and separation are especially prominent at the splat boundaries, highlighted in Fig. 43, and not reflected in the stress distribution of the model since coating structure is not included. Potential metallurgical bonding at the interface is not considered. IMCs may be present at nano-scale depth (Fig. 40), but previous TEM analysis showed no visible IMCs [45].

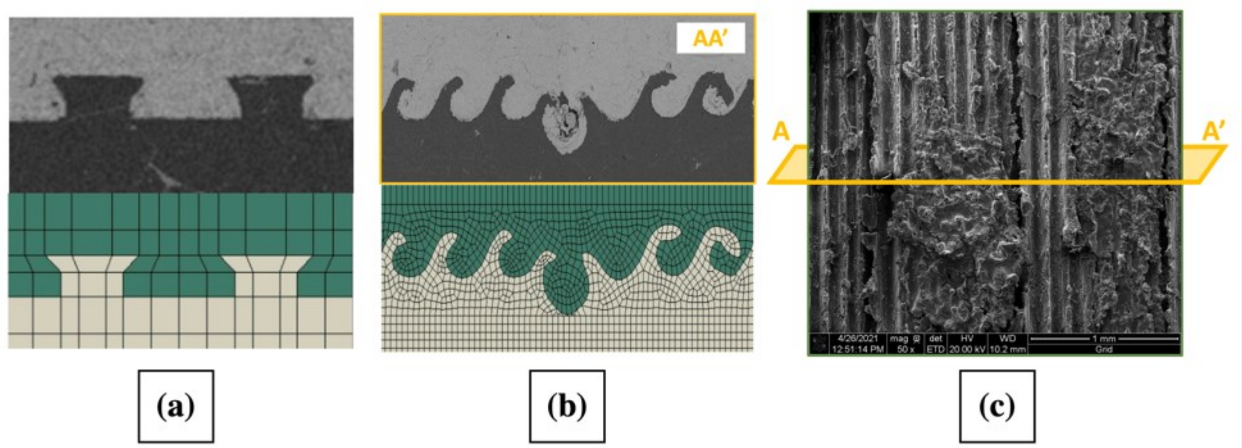

Fig. 42 Cross-sectional SEM image comparison with (a) dovetail model, (b) wave model, and (c) fracture face SEM image showing the orientation of cross-sectional image AA'.

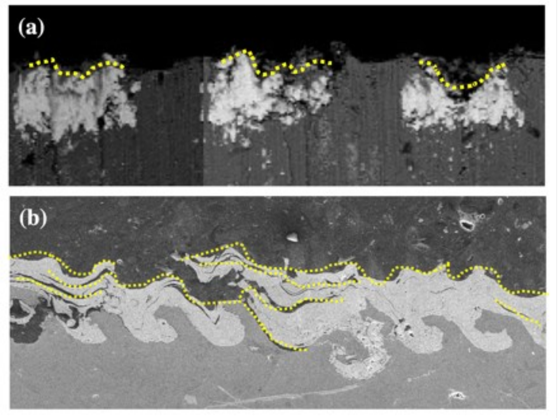

Fig. 43 SEM images with experimental breakage highlighted in yellow for (a) dovetail and (b) wave patterns.

5.3 Fracture Mechanisms

When examining the dovetail model at both the fracture surface and side-view, the stress distribution in Fig. 44 shows that the coating is expected to break in the areas highlighted by yellow dashed lines. Consequently, the model shows that the coating breakage will be embedded in the regions outlined in white dotted lines, between the dovetails and at the "wells".

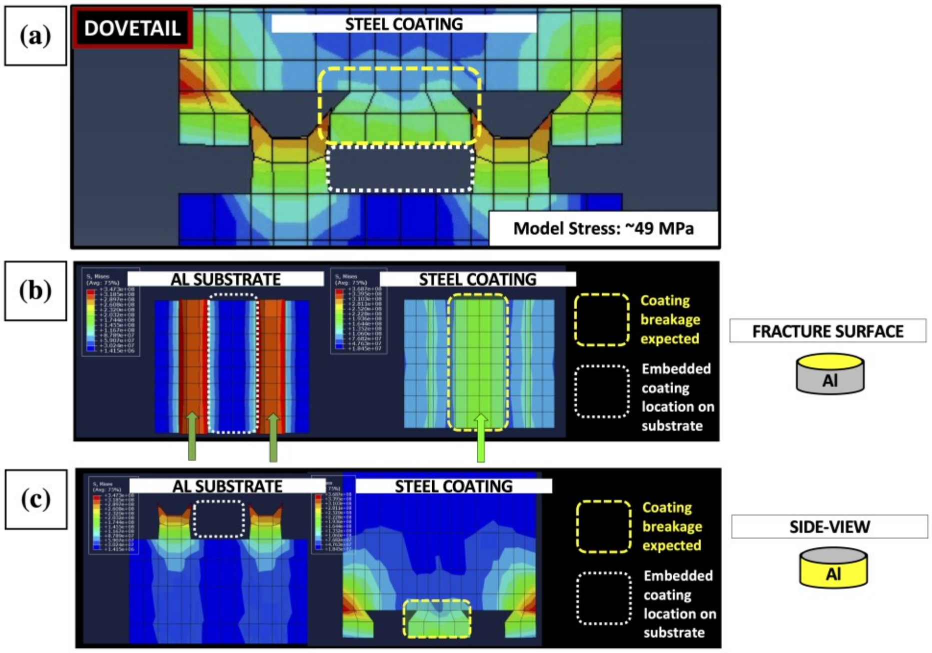

Fig. 44 Dovetail pattern model with expected coating breakage regions highlighted in yellow dashes, and location of embedded coating on substrate highlighted in white dots for (a) complete side view, (b) separate fracture surface view, and (c) separate side view.

Similarly, Fig. 45 shows the stress distribution in the wave pattern at various orientations with coating breakage highlighted in yellow dashed lines and locations of coating embedding in white dotted lines. It can be seen clearly that the breakage is most likely to occur first in the two waves highlighted by yellow, where the stress concentration is indicated in red. In both the interface patterns, we can see that the locations of expected breakage/embedding match what is seen in the SEM images of the tested samples, previously shown in Fig. 37 and Fig. 38.

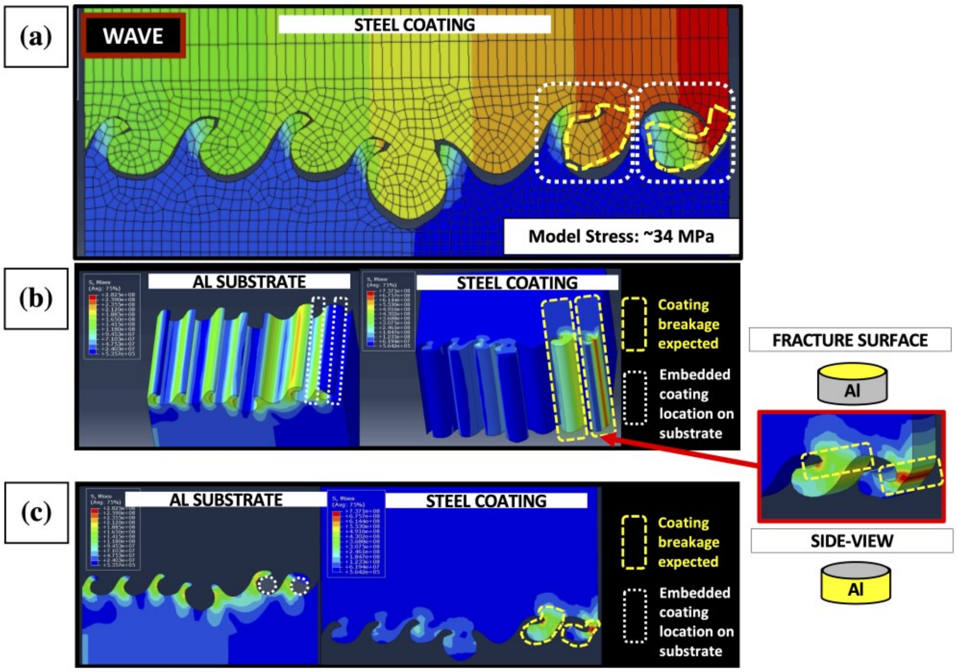

Fig. 45 Wave pattern model with expected coating breakage regions highlighted in yellow dashes, and location of embedded coating on substrate highlighted in white dots for (a) complete side view, (b) separate fracture surface view, and (c) separate side view.

The wave pattern stress concentration is shown again in Fig. 46(a) with a potential fracture path shown. The pink region highlights where the stress concentration is high on the model (i.e., red) and breakage would initiate. The breakage would then propagate to the white path, where the subsequent stress concentration is located. After that point, there is no clear region of concentration, and the breakage path can travel in various ways. Three examples are shown in the yellow (i.e., dashed, dotted, and dash-dotted lines). The dashed line and dotted line show a breakage path at varying distances away from the interface, whereas the dash-dotted line shows breakage at the interface. Both the dashed and dotted lines result in breakage through the coating (cohesion failure) that would cause varying degrees of coating to remain on the substrate. This cohesion failure would result in D0, D1 (no/mild deformation) levels of substrate pattern mechanical deformation, previously described in Fig. 39. This is due to breakage within the coating occurring before the substrate waves are subjected to heavy loading. In contrast, the dash-dotted line shows adhesion failure at the interface which would result in little to no coating remnants at the interface. Adhesion failure also results in D2, D3, D4 (medium/heavy deformation, fracture) levels of substrate deformation. After the initial fracture and early breakage, the path is dependent firstly on if the mechanical interlocking at the interface is weaker than coating cohesion – in which case, adhesion failure will occur along the interface pattern with high substrate deformation and low degree of coating remnants. If coating cohesion is weaker, then the breakage path will follow the features within the coating (i.e., splat and particle boundaries, and voids), with low substrate deformation and high degree of coating remnants. These three paths shown in Fig. 46(a) are all clearly observed in the experimental specimen SEM images, shown in Fig. 46(b). In both the model and SEM images, three lines are highlighted: (1) cohesion coating breakage far from the interface is indicated by dashed lines, (2) cohesion coating breakage close to the interface is indicated by dotted lines, and (3) adhesion breakage is indicated using dash-dotted lines. Studies in literature found that bonding strength could be improved by controlling the interfacial microstructures [34]. It was found through FEM analysis that the fracture path is unclear after a certain point in terms of stress concentrations, hence the three potential lines of failure mentioned above. However, it was confirmed from the SEM analysis of experimental specimen that the fracture path is dictated by the microstructure of the coating (i.e., features) local to the interfacial region after initial breakage.

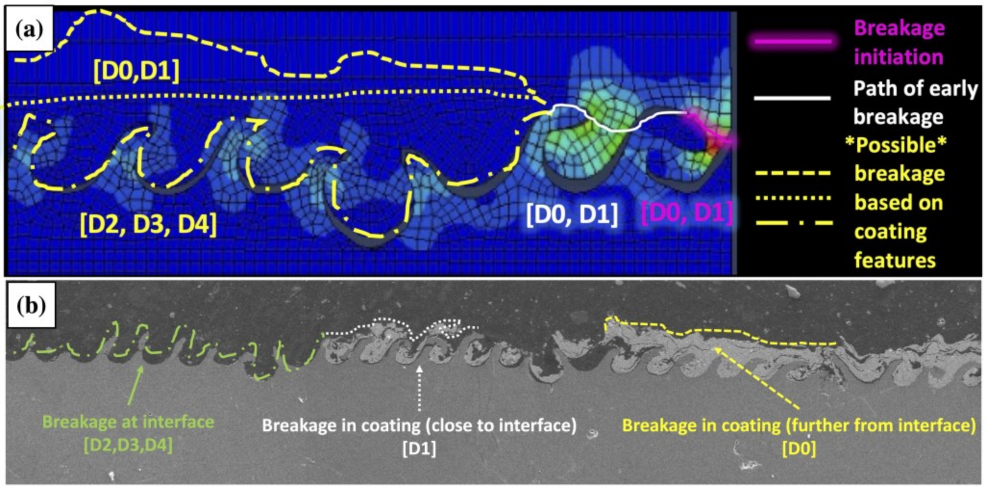

Fig. 46 Wave pattern (a) model showing expected breakage paths, and (b) SEM image of test sample with various breakage identified: breakage at interface (green dash-dotted line), breakage within coating while close to the interface (white dotted line), and breakage within the coating while further from the interface (yellow dashed line).

Overall, the dovetail model pull strength is higher than what is seen in experimental results, which is likely due to the small irregularities that occur within this pattern that have not been considered since it was modelled after the dovetail drawing geometry. While the discrepancy between the drawing and SEM images for the dovetail pattern are not as prominent compared to the wave pattern, the drawing is still not a perfect representation of the interface pattern. The small irregularities in the actual pattern also contribute to the varying degrees of deformation and/or breakage of the side portions of the interface geometry, whereas the model shows the same stress concentration for all these regions. Similarly, the wave model stress is also greater than the average stress of the corresponding experimental results. However, some samples had a pull strength greater than the model. The highly irregular wave pattern can contribute to varying degrees of mechanical interlocking and it is likely that in those samples, mechanical interlocking was more successful than the region of the SEM image that the wave model was based on. It was also found that due to the intricate geometry of the wave pattern, it had a higher likelihood of improper coating deposition which results in unfilled voids at the interface, specifically within the waves. These regions can be seen in the SEM images prior to testing shown in Fig. 9(c).

While maximum pull stress shown in Fig. 41 is calculated using the maximum pull load at failure and the cross-sectional area at the interface, the model shows the stress concentrations at the interface, which are much higher than the resulting pull strength. The stress concentration in the wave model is shown in Fig. 47(a) with orange and red circles for the coating and substrate respectively. The stress at these specific locations is plotted in Fig. 47(b). Based on properties from Anton Paar analysis, the yield stress of the coating is 785.5 MPa (highlighted by the orange circle in Fig. 47(b)) which occurs at a separation of 10.0 μm, where corresponding pull stress is around 31 MPa. Similarly, the yield stress value of the substrate is 322 MPa (highlighted by the red circle in Fig. 47(b)) which also occurs at a separation of 10.7 μm and corresponding pull stress of around 32 MPa. In the wave model, the coating and substrate will both yield around the same point (around 10-11 μm separation, 32 MPa pull stress). A number of these failures within the substrate waves and interlocked coating then occur before the entire sample fails at 15 μm separation, 34 MPa pull stress.

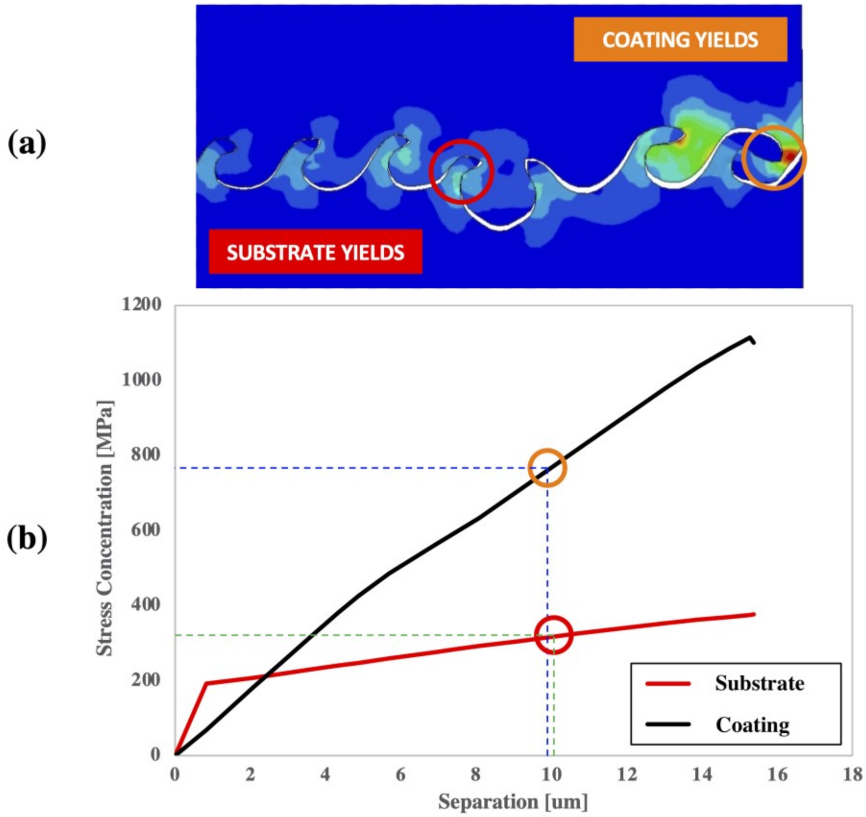

Fig. 47 Wave model stress concentration (a) locations in coating (red) and substrate (orange), and (b) stress concentration plotted with separation.

The stress concentration for the dovetail model is shown in Fig. 48(a). Using the same yield properties, the substrate yielding (highlighted by the red circle in Fig. 48(b)) occurs at a separation of 65 µm and corresponding pull stress of around 27 MPa. However, the coating does not reach its yield. Contrary to the wave model, not only do the substrate and coating not yield at a similar point, the coating also does not experience high enough stresses to cause yielding. This means that in an ideal model, the failure of the sample is solely due to failure within the substrate since coating yielding is not present. However, since the sample failure occurs at 36 µm separation, 49 MPa pull stress, the substrate is not expected to yield before the mechanical interlocking at the interface is compromised due to deformation. This matches what is observed experiments, where the coating does not experience breakage (Fig. 38(a)) and there is deformation that eliminates interlocking (Fig. 39(a)). Again, the reason that experimental results show some yielding in the substrate is seen (Fig. 39(a)), as well as coating remnants due to breakage/cohesion issues (Fig. 38(a)) is rooted in the limitations of the model related to unmodelled irregularities in the geometry and coating microstructure.

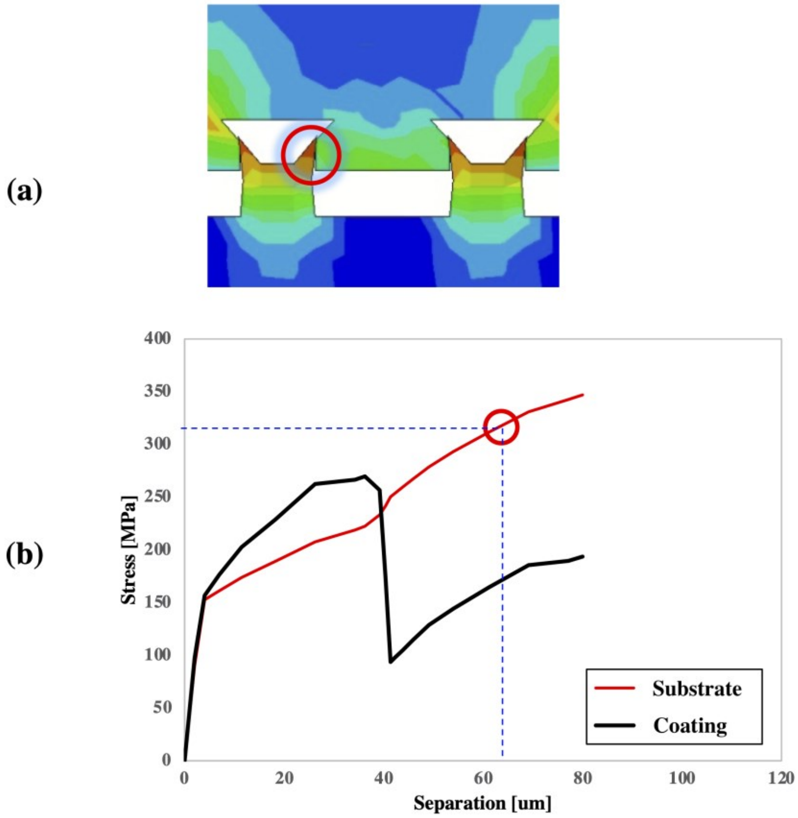

Fig. 48 Dovetail model stress concentration (a) locations in coating (red), and (b) stress concentration plotted with separation.

The locations of stress concentrations within both the coating and substrate (as well as separation behaviour) from the model can be used to predict where they are expected in experimental pull tests. Though we don't have measurements of the stress concentrations occurring in experimental testing, they are likely like those experienced in the finite elements model.

Since the model does not account for the multitude of microstructural intricacies in the thermal sprayed coating, the sensitivity of the model to two common features was briefly investigated. The location of these features was based on previous characterization that identified where these features are most likely to reside (Fig. 49). These features were taken into consideration in modelling representative particles and voids in the dovetail model, shown in Fig. 49(c) and (d) respectively. The simulation of the original model in Fig. 49(e) shows separation that is even across the dovetails, whereas the models with features in Fig. 49(f) and (g) show that the balanced separation is disrupted by the feature. It can also be seen that the particle away from the interface in Fig. 49(f) has little effect when it comes to the type of loading present in adhesion pull tests, and the particle at the interface is causing uneven separation that is greater on the left side. Similarly, the void model in Fig. 49(g) shows larger separation on the left. The stress is not reported in the figure since the modelled values are not necessarily relevant or accurate in the model where only the effects of a few single features are considered. In reality, the entirety of the coating is comprised of features and splats that affect the stress that is experienced.

When inspecting the substrate, it can be seen in Fig. 50(a) that the original model experiences stress concentrations in the aluminum across the two tips of each dovetail. When particles are considered (Fig. 50(b)), a stress concentration is seen at a location that experiences the most interlocking, which is no longer evenly distributed due to the uneven separation. In the case of the void (Fig. 50(c)), the location of heavy interlocking is near the void, but due to the absence of material to facilitate interlocking at this location, the stress concentrates on the other side of the dovetail. A combination of the deformations seen in the simulation are observed in experiment - it is likely that in cases where separation is more balanced, heavy substrate deformation at the dovetail tips is observed (D3 in Fig. 39(a)). When separation is uneven and stress concentrations are not distributed across dovetail tips, fracture is more likely to occur (D4 in Fig. 39(a)). In reality, a combination of all types of deformation (D0, D1, D2, D3 in Fig. 39(a)) is observed because there are an abundance of features within the coating – in many areas the features would result in some balance, and others would result in varying degrees of imbalance in separation across the fracture surface which results in the corresponding array of substrate deformation.

When considering the coating side, the stress is concentrated at the bottom region of each dovetail in the original model without features (Fig. 50(d)). However, it was previously shown in Fig. 48(b) that the coating does not necessarily yield. It is also seen in Fig. 50(e) and (f) that the uneven separation also affects the location of stress concentration in the coating, namely where the lowest degree of separation occurs, and mechanical interlocking is prominent. Consequently, the discrepancy between the model pull strength (Fig. 41) and experimental results (Table 4) is attributed to the effects of the varying types of features as well as the combination of such. The plot of pull strength with separation for various models is shown in Fig. 51(a). The particle model (grey) follows the original model (blue) until 15 μm separation before it begins to deviate where it likely experiences the effects of the particle close to the interface. The models with the void (yellow), and an additional model including the particles and void (orange) show lesser pull strength at the corresponding separation. Overall, the pull strength reduction is much greater with the addition of a void compared to particles. A similar stress concentration analysis that was performed on the original models in Fig. 47 (wave) and Fig. 48 (dovetail) can be done for the dovetail model with features to compare differences in the point of yield. Fig. 51(b) shows the stress concentrated locations within the substrate (from Fig. 50) plotted with separation values of the various models. Substrate yield is indicated with the horizontal red line, which shows that yielding in the substrate occurs at differing separation points amongst the models. This shows that the addition of imbalance due to coating features will cause yield to occur at a considerably lower separation compared to cases of more balanced separation depicted in Fig. 49(e). Again, yielding of the substrate does not indicate complete failure of the sample, but rather when breakage first occurs in the interface geometry.

It should be noted that the numeric values of pull strength (Fig. 51(a)) and separation at yield (Fig. 51(b) are just a relative comparison and not values to be considered since an unrealistic configuration of features is modelled. The study is only to show the effects on separation that features can cause and the corresponding stress distribution changes. The modelling is also aggressive as it is applied to a sub-size model which implies the features are repeated across the multitude of dovetails in a sample. Not only is this not the case, but some combination of features will also balance out the separation such that is it like the original model in Fig. 49(e). The sensitivity study confirms the degree of separation differences due to the coating microstructure can have a large effect on the pull strength: between 13 and 30 percent reduction in pull strength in the addition of these features. This along with the unmodelled irregularities of interface across the dovetails and through the depth of the row account for the discrepancies observed in the experimental and model pull strength values.

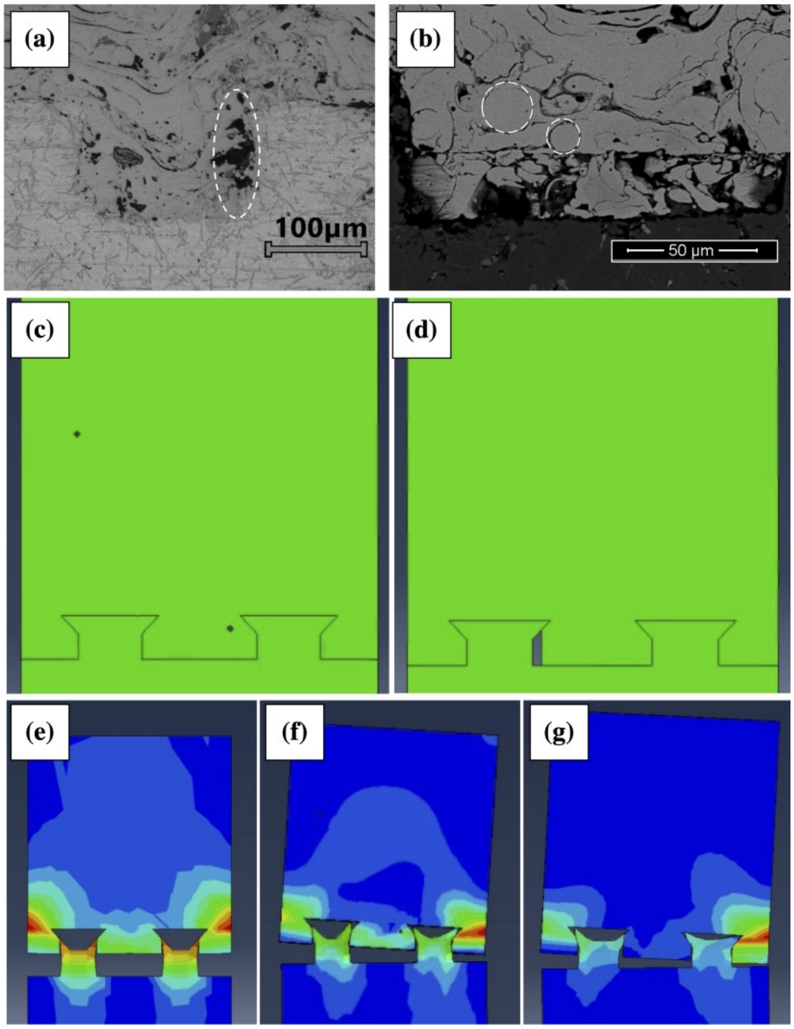

Fig. 49 SEM images showing common locations of (a) voids and (b) resolidified particles. Model representations of (c) particle inclusions and (d) void feature. Simulations showing the (e) original dovetail model, (f) model with particles, and (g) model with void.

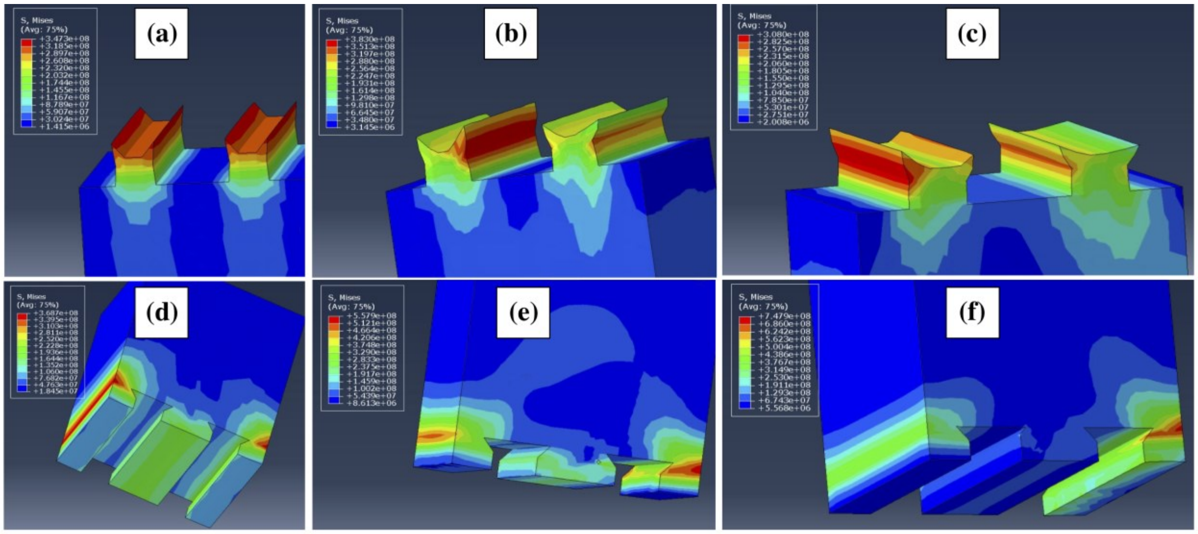

Fig. 50 Simulations showing the substrate side of the (a) original dovetail model, (b) model with particles, and (c) model with void. The simulations are also shown for the coating side of the (d) original dovetail model, (e) model with particles, and (f) model with void.

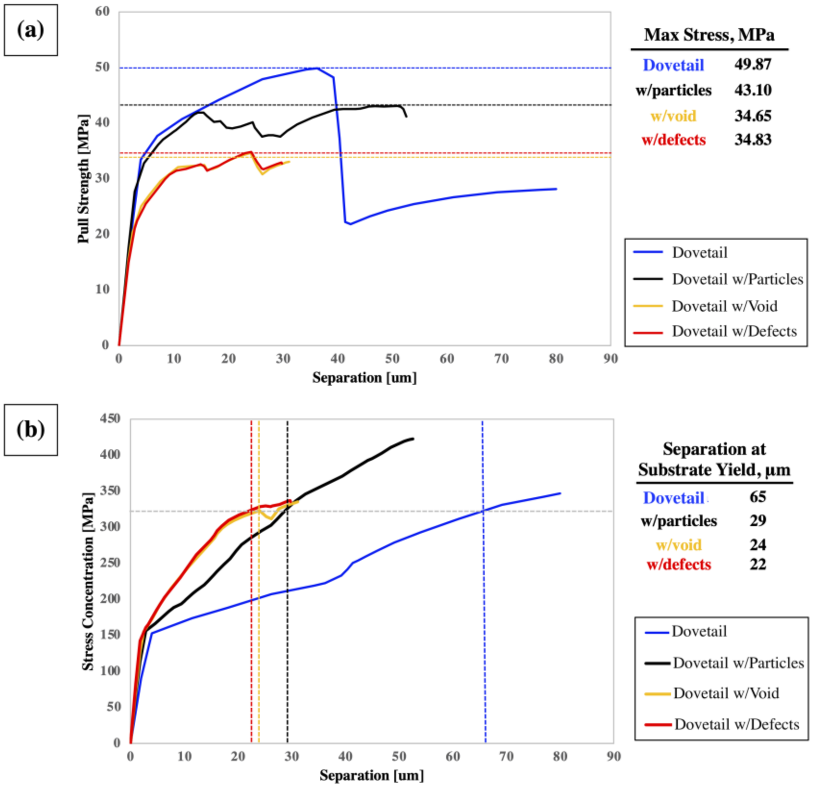

Fig. 51 Various models plotted against separation showing (a) pull strength, and (b) stress values at concentrated locations in the substrate.

Chapter 6

Quasi-Static Characteristics of PTWA Coating at Room and High Temperatures

6.1 Quasi-Static Properties of Cylinder Samples at Room Temperature

6.1.1 Quasi-Static Properties of Cylinder Samples

Three-point bending tests were performed and monitored by a DIC and video camera system. During the tests, the load-displacement data was recorded directly from the tensile frame and the corresponding strain distribution map across the sample along the x-direction was calculated using the GOM ARAMIS software, shown in Fig. 52(a) to (d). The images captured during the tests were also recorded; the side and bottom views of the sample at the time of failure are presented in Fig. 52(e) and (f). The strain distribution just prior to failure exhibited maximum strain at the bottom face (Fig. 52(c)) which corresponds to the coating surface and decreases towards the substrate surface. Multiple strain localization points were identified and may be correlated to surface defects resulting from post-processing of the coating (i.e., diahon or machining). The strain distribution at the fracture location is shown in Fig. 52(d) which is located exactly in the middle of the sample. The maximum bending strain at the coating surface was recorded to be over 1.5% before failure.

A sample of the calculated stress (equivalent section analysis method for composite beams) and recorded strain plots at the coating surface and both sides of the interface are shown in Fig. 53(a). A comparison of the calculated bending strength at the coating surface and both sides of the interface across all tested samples are shown in Fig. 53(b). Among the bending strengths at three different locations, the coating surface experienced a maximum strength with an average value of 1480 ± 108 MPa.

6.1.2 Quasi-Static Fracture Mechanisms of Cylinder Samples

SEM inspection of the fracture surface (Fig. 54) revealed that crack initiation occurred at the dovetail wall (as opposed to the coating surface where maximum bending stress is present as shown in Fig. 53(b)), and eventually propagated towards the coating surface. In some samples, the crack was transferred from one side of the dovetail wall to the other and coating delamination occurred on this sidewall, shown in Fig. 54. When the fracture surface (i.e., the dovetail wall) was observed from both the substrate (Al side) and coating (steel side) sides, it was found that the steel side contained a considerably large amount of re-solidified particles compared to the typical distribution throughout the coating. This finding is important in realizing: (1) a key incompetency of the coating deposition process regarding this type of surface roughening profile, and (2) key areas of weakness in the samples and the related microstructural features. Due to the presence of these re-solidified particles and their high-hardness oxide boundaries on the dovetail wall and the fact that crack initiation occurs at this location, this implies that there is inadequate bonding between the coating and substrate on these sidewall portions of the dovetail profile. Bonding occurs mainly on the top (Region a, Fig. 54) and bottom (Region b) sections of the dovetail. Recall that it has been observed during interface microstructure studies via TEM that there is barely any metallurgical bonding between steel coating and Al substrate.

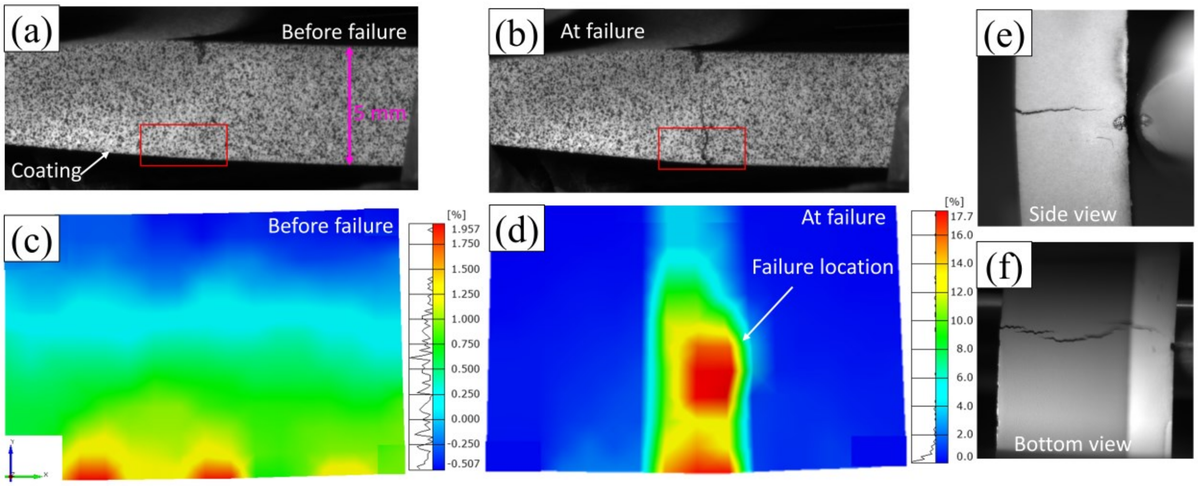

Fig. 52 Three-point bending tests using DIC and video camera system showing (a) the sample before failure, (b) the sample at the time of failure, (c) strain distribution along x-direction before failure, (d) strain distribution along x-direction at the time of failure, (e) side view of the fracture location, and (f) bottom view of the fracture location.

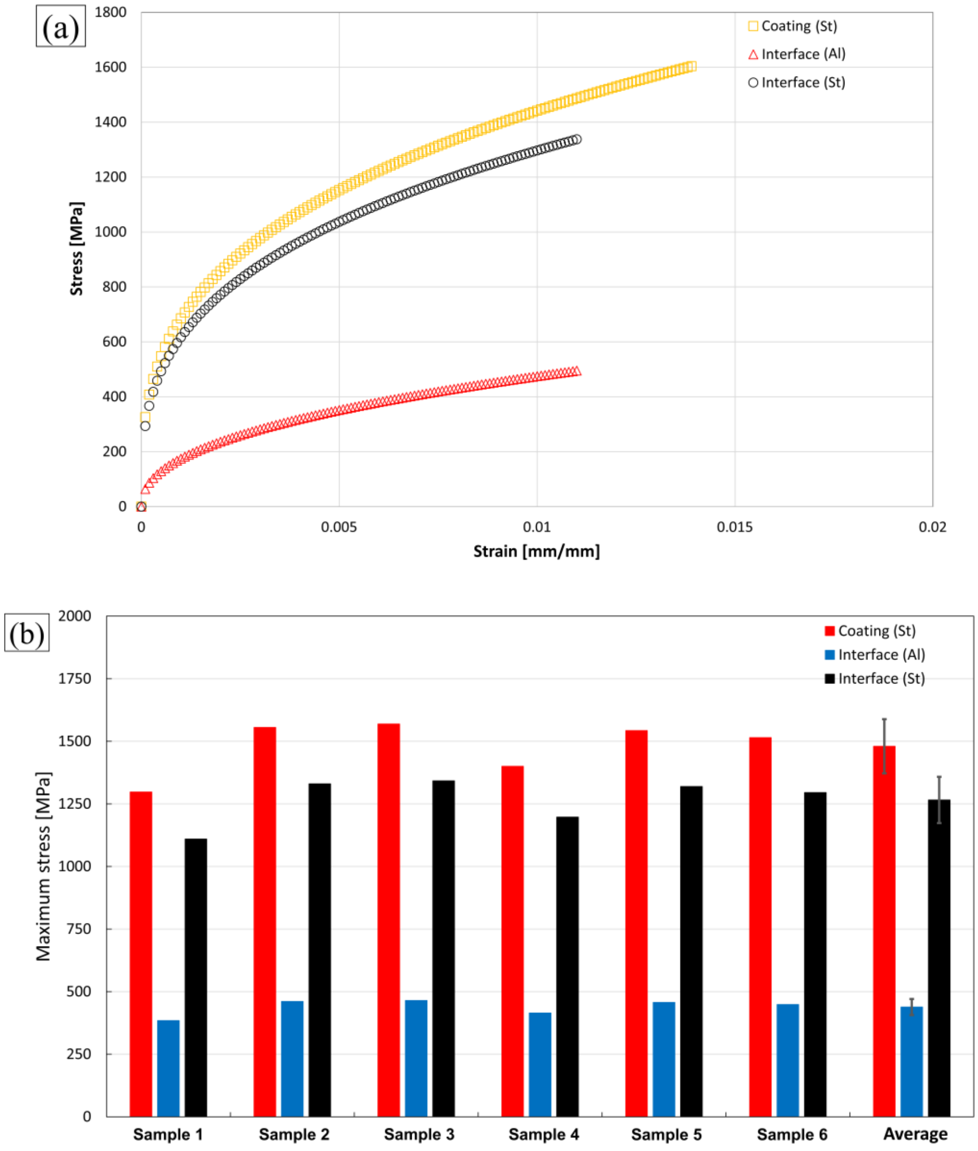

Fig. 53 Monotonic three-point bend test results showing (a) transformed bending stress vs. strain curves at three different locations (coating surface, interface at coating side, and interface at substrate side), and (b) maximum bending stress across six samples at three different locations.

A microstructural examination of the fracture surfaces was conducted using SEM as shown in Fig. 55. Based on the crack initiation and propagation sites identified on the fracture surfaces, three distinct failure modes are proposed and schematically presented in Fig. 55(a) with the corresponding failure load in Fig. 55(b). The schematic shown in Fig. 55(a) is the bottom facing side of the three-point bend fractured sample, and the monotonic load was applied on the top (i.e., opposite) surface.

Studies in literature observed coating delamination along the coating/substrate interface prominently on the fracture surface. Cracking of the coating was also a potential failure mechanism due to the inconsistent local coating properties (i.e., coating features and structure) [5]. These mechanisms are seen with greater detail in the bending tests that were performed: the failure modes can be categorized as complete sidewall delamination (Mode A) or partial sidewall delamination (Modes B and C). In Mode A, the crack path propagated along the dovetail sidewall, ensuring complete separation of coating from the Al. This is due to the lack of metallurgical bonding resulting from the excessive re-solidified particles shown in Fig. 54. In contrast, both Modes B and C showed partial dovetail sidewall separation. In Mode B, one dovetail in the coating experienced breakage and the crack moved through the coating to another sidewall. In Mode C, multiple dovetails broke which resulted in the crack path moving back and forth in a zigzagged manner between sidewalls. While crack initiation did not occur due to the varying hardness values amongst the features within the coating, in Modes B and C, the coating experiences breakages as the crack propagate. In Mode A, the bonding at the dovetail sidewalls poses weaker points than the corresponding hardness distribution within the coating. In Modes B and C, there are one or multiple points where the hardness distribution causes weaker locations than the bonding at the dovetail sidewalls, causing breakage through the coating. If this is the case in multiple locations as the crack travels, the breakage will occur at numerous points within the coating and the crack propagates in a zigzagged manner, as it does in Mode C. The hardness distribution in the coating (Section 3.5 Coating Hardness) is related to the composition and features within the microstructure (i.e., splats, oxides, re-solidified particles, boundaries), discussed in Section 4.1 Coating Characterization. Therefore, at areas of higher hardness within the coating (oxide-rich regions or oxide boundaries of splats and re-solidified particles) and depending on the degree of insufficient sidewall bonding, there is the potential that the crack will break through the coating (following areas of high hardness) instead of continuing a path of complete sidewall delamination.

Out of six three-point bend samples, four samples experienced Mode C failure, and one failed to each Modes A and B. When the mode of failure is compared with failure peak load, it was found that Mode C absorbed more load before fracture. This can be correlated to the fracture path which involves the breakage of multiple dovetails that will ultimately lead to the more absorbed energy. A shift of failure mode from A to B or C is dependent on the metallurgical bonding between coating and patterned Al substrate, the existence of limited re-solidified particles (related to the coating deposition parameters), coating features, and hardness. When the failure modes were compared with microstructural analysis, it was determined that Mode C is the preferred mode of failure.

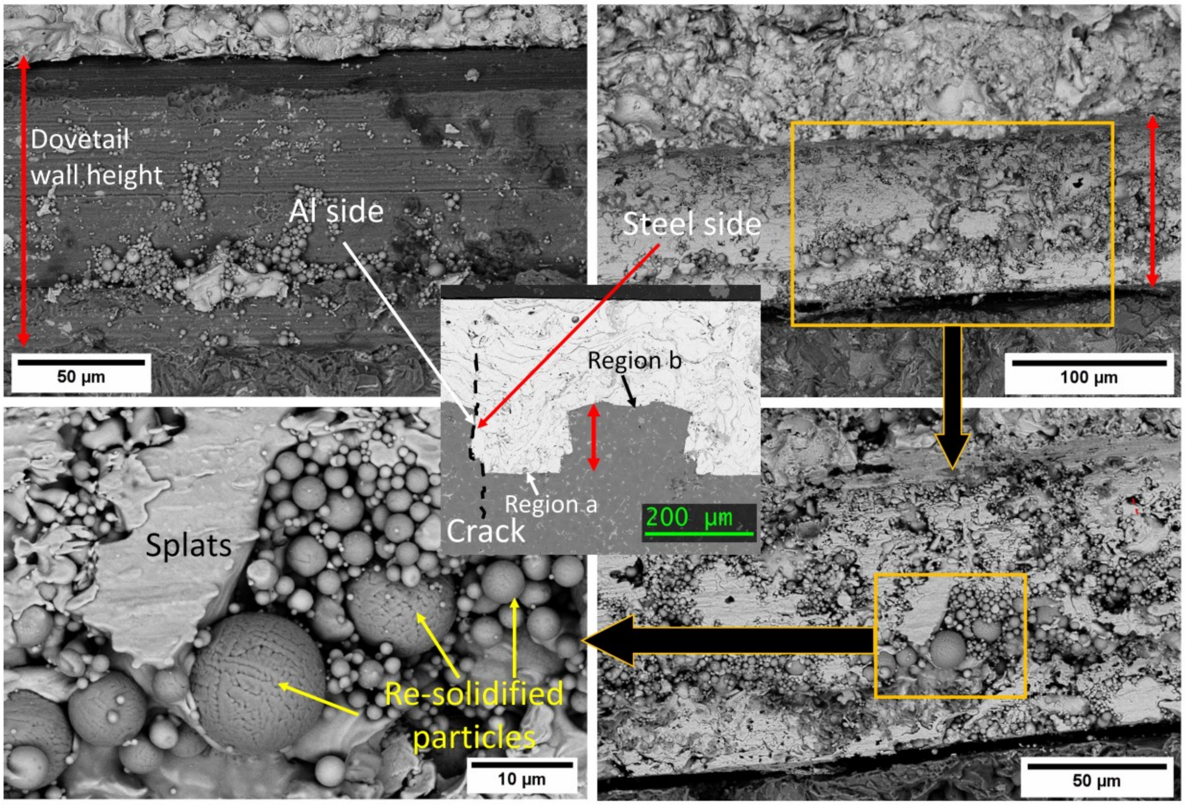

Fig. 54 Detailed view of the fracture surface on both Al substrate and steel coating sides.

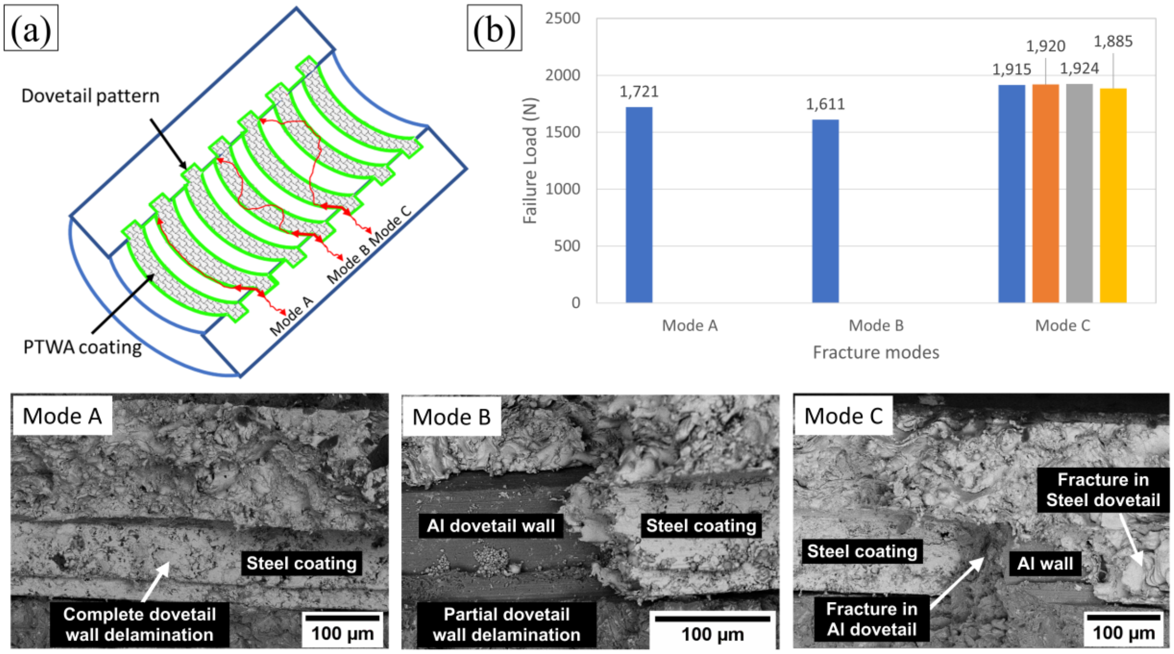

Fig. 55 The three-point bend test results showing (a) a schematic of three different failure modes identified in the fractured samples, (b) a plot of failure load as a function of fracture modes; and SEM micrographs of each mode of fracture.

6.2 Quasi-Static Properties of Flat Samples at Room and High Temperatures

6.2.1 Quasi-Static Properties of Flat Samples

The mechanical properties obtained from three-point bending testing at RT, 100°C, and 250°C for the four categories of samples are summarized in Table 5. In addition to the yield and ultimate strengths, the Ramberg-Osgood coefficients, strength coefficient (H) and strain hardening exponent (n) are calculated from the output data.

Table 5 Mechanical Properties from Quasi-Static Bending Testing

Mechanical Properties	A319-W RT	A319-W 100°C	A319-W 250°C	A319-H RT	A319-H 100°C	A319-H 250°C	A356-W RT	A356-W 100°C	A356-W 250°C	A356-H RT	A356-H 100°C	A356-H 250°C
Elastic Modulus, *E* [GPa]	214 Std. 41	191 Std. 81	118 Std. 7	272 Std. 24	203 Std. 10	167 Std. 21	219 Std. 74	149 Std. 41	100 Std. 20	285 Std. 28	112 Std. 30	129 Std. 22
Yield Strength[1] [MPa]	649 Std. 51	714 Std. 165	466 Std. 14	758 Std. 30	637 Std. 10	524 Std. 9	973 Std. 121	702 Std. 113	567 Std. 24	980 Std. 15	890 Std. 56	578 Std. 145
Engineering Ultimate Strength [MPa]	844 Std. 60	871 Std. 129	502 Std. 2	833 Std. 7	746 Std. 26	528 Std. 18	991 Std. 46	854 Std. 30	607 Std. 31	1041 Std. 12	942 Std. 28	590 Std. 122
True Ultimate Strength [MPa]	861 Std. 57	885 Std. 135	513 Std. 0	846 Std. 5	763 Std. 38	531 Std. 17	1004 Std. 55	869 Std. 34	616 Std. 28	1052 Std. 18	961 Std. 28	597 Std. 120
Engineering Fracture Strain [%]	7 Std. 1	2 Std. 1	6 Std. 5	3 Std. 2	4 Std. 1	2 Std. 2	2 Std. 2	2 Std. 0	6 Std. 1	1 Std. 1	7 Std. 6	5 Std. 6
Strength Coefficient[2], *H* [MPa]	2190 Std. 884	1378 Std. 134	595 Std. 19	1782 Std. 442	1227 Std. 77	637 Std. 34	2585 Std. 1329	1259 Std. 355	767 Std. 48	2331 Std. 419	1167 Std. 230	796 Std. 68
Strain Hardening Exponent[2], *n*	0.195 Std. 0.056	0.101 Std. 0.052	0.038 Std. 0.005	0.141 Std. 0.039	0.112 Std. 0.012	0.031 Std. 0.004	0.160 Std. 0.080	0.082 Std. 0.061	0.049 Std. 0.004	0.141 Std. 0.025	0.054 Std. 0.056	0.031 Std. 0.010

[1] 0.2% offset

[2] Ramberg-Osgood coefficients: $\varepsilon = \frac{\sigma}{E} + \left(\frac{\sigma}{H}\right)^{1/n}$

The true stress-strain are plotted for RT, 100°C, and 250°C and shown in Fig. 56(a), (b), and (c) respectively. When considering elastic modulus, yield strength, true ultimate strength, and engineering ultimate strength values, the A356 substrate (yellow and black plots) generally have higher yield strength values when compared to the corresponding A319 results (red and blue plots) in the same orientation, indicating that the A356 substrate is stronger for this type of loading. This can be directly related to the bulk substrate properties – A319 has a lower yield strength than A356, though they both have the same modulus value. The engineering fracture strain showed no obvious trends. *H* values are mostly higher in A356, except for the 100°C results, which are higher in A319 which correspond to the extrapolated value of the true stress at true strain of 1.0. Most values of *n* were higher at A319 apart from the A319-W-250 result (0.038), which was lower than A356-W-250 (0.049). This indicates that the A319 substrate is generally more elastic than A356.

The effects of orientation show that the A356 H-orientation consistently reports higher strength values compared to its W-orientation counterpart. This is generally due to the way the pattern rows run along the sample – the H-orientation can be likened to applying bending force perpendicular to the grain in wood where the force can be maximized in this configuration, where more energy is required for breakage through all the rows compared to delamination along one row. The effects of orientation are less evident in the A319 substrate. Most values of *n* were higher in the W-orientation apart from A319-W-100 (0.100), which was lower than A319-H-100 (0.112). While the same materials are involved, this may infer that the W-orientation is generally experiences more elasticity due to the orientation of the interfacial pattern than the H-orientation.

To best display the effects of temperature, all three temperatures for each of the four specimen types are shown in Fig. 57. The modulus and strength values are reduced as temperature is increased – a trend that is observed across all sample categories. Engineering fracture strain lacked a distinguishable trend with increasing temperature. *H* values also consistently decreased as temperature was increased. Finally, decreasing *n* values were observed increasing temperature, apart from A319-H results which showed values of 0.096, 0.112, and 0.031 for RT, 100°C, and 250°C. The trends observed in the results are better represented visually by the true stress strain curves for the six tests performed at RT, 100°C, and 250°C are shown in Fig. 56. For instance, when comparing true ultimate strength in these curves, all A356 values are larger than A319 plots in the corresponding temperature and orientation (except for the W-orientation at 100°C).

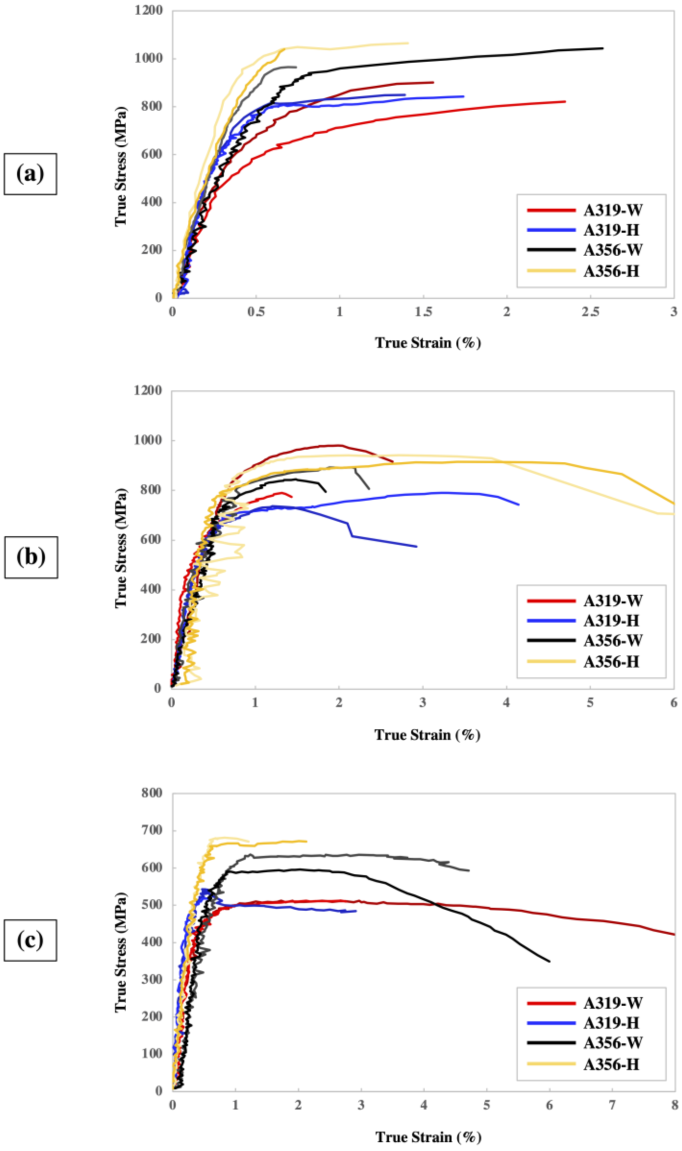

Fig. 56 True stress strain curves of RT quasi-static bending testing with A319-W in orange, A319-H in blue, A356-W in yellow, and A356-H in green at (a) RT, (b) 100°C, and (c) 250°C.

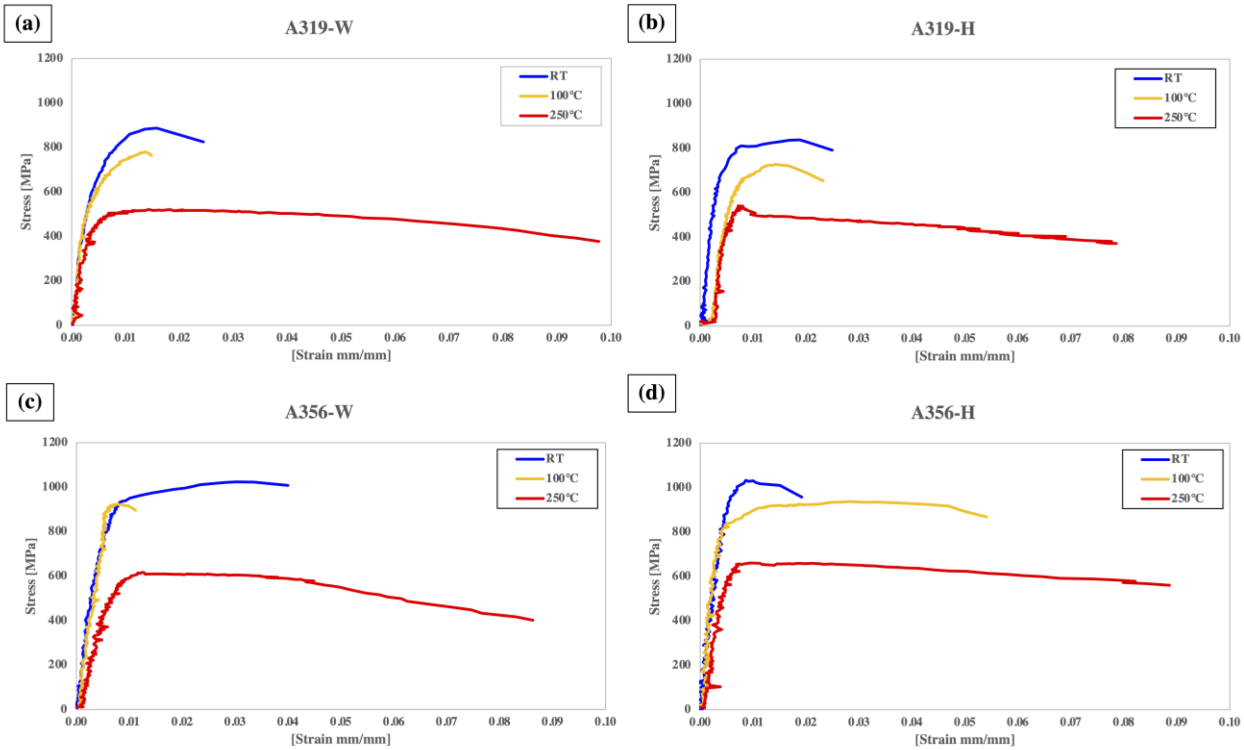

Fig. 57 Stress strain plot comparing the effects of three temperatures for (a) A319-W, (b) A319-H, (c) A356-W, and (d) A356-H.

6.2.2 Quasi-Static Failure Mechanisms of Flat Samples

The failure mechanisms of very similar testing were previously studied and reported to identify three different modes of failure. The difference in testing was that samples were extracted from coated cylinder sleeves instead of flat coated plates. As a result, prior test samples had a slight curvature to them and were only extracted in the W-orientation. The interface pattern geometry was different as it resembled the traditional dovetail [17]. The paths of the three failure modes involving various degrees of delamination and breakage within the coating are shown in Fig. 55(a) using red arrows. The failure modes can be categorized as complete sidewall delamination (Mode A), or partial sidewall delamination (Modes B and C). In Mode A, the crack path propagated along the dovetail sidewall, ensuring complete separation between the coating and substrate. In contrast, Mode B sees one dovetail in the coating experiences breakage and the crack path moves through the coating to another sidewall. Mode C shows multiple dovetails break which results in the path moving back and forth in a zigzagged manner between further sidewalls.

When it comes to the wave patterned samples, the SEM fracture surface images at RT are shown in Fig. 58 for all four categories. It can be noted that the wave pattern can be observed in the H-orientation fracture surfaces (A319-H in Fig. 58(b) and A356-H in Fig. 58(d)). The coating, and substrate regions are labelled, sandwiching the interface region that encompasses the height of the dovetail. The interface region is where the SEM analysis is focused and the main area of interest.

The W-orientation is similar to prior cylinder sleeve testing and the modes of failure can be compared. W-orientation samples experience areas of delamination down a row, as well as breakage through the coating to another row, where it delaminates again before breaking through the coating again. This is clearly seen in the W-orientation images, A319-W (Fig. 58(a)) and A356-W (Fig. 58(c)). At the interfacial region, breakage in the waved dovetails (Fig. 59(a)), coating cohesion failure (Fig. 59(b) and (c)), and interlocking breakage (Fig. 59(d)), are observed at RT. As a result, the W-orientation RT results represent Modes B failure. More breakage through the coating is seen at elevated temperatures, shown in Fig. 59(a), Fig. 61(a) and (c) for each of the temperatures. As a result, Mode C failure was identified at higher temperatures – 250°C fracture paths were more zigzagged in nature than the corresponding 100°C paths. Higher temperatures also resulted in more breakage at the interface which is highlighted in Fig. 59(d), and present in Fig. 61(a) and (c). At higher temperatures, it was observed that the substrate material has a prominent effect on the overall failure mechanism. The increase in temperature caused softening of the substrate material, making the coating/substrate interface more prone to fracture under the quasi-static loading.

Since the curved engine sleeve testing was not performed in the H-orientation, the previously observed failure modes are not applicable in this orientation. Coating cohesion failure (Fig. 60(a) and (d)), coating cohesion failure (Fig. 60(b) and (c)) are observed at RT. The abrupt cohesive coating breakage that occurred is due to the maximum stress at the coating surface. Failure in both substrates for this orientation was dominated by coating/substrate delamination at the interface. Individual coating features within each interfacial pattern wave are generally insignificant in terms of their effects on the overall failure mechanism. Samples at RT and 100°C did not show major failure mechanism differences; however, a significant coating/substrate delamination was observed at 250°C. Additionally, 250°C samples showed large degrees of separation at the interface due to the differences in thermal expansion of the coating/substrate materials at elevated temperatures. As a result, complete separation/delamination of the coating from the substrate was seen. At this temperature, the substrate material was also seen to fracture in a ductile manner, as identified by degree of dimple feature occurrence shown in Fig. 61(d), as opposed to the other temperatures (Fig. 60 and Fig. 61(b)).

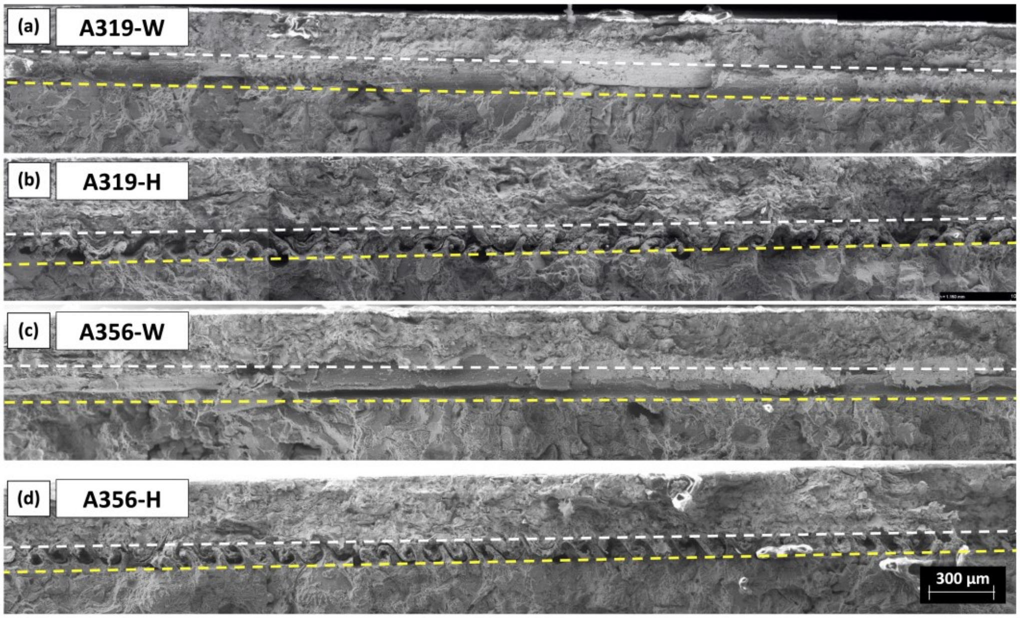

Fig. 58 SEM images of the RT fracture surfaces with the coating, region where interlock occurs (interface pattern height), and substrate for (a) A319-W, (b) A319-H, (c) A356-W, and (d) A356-H specimen.

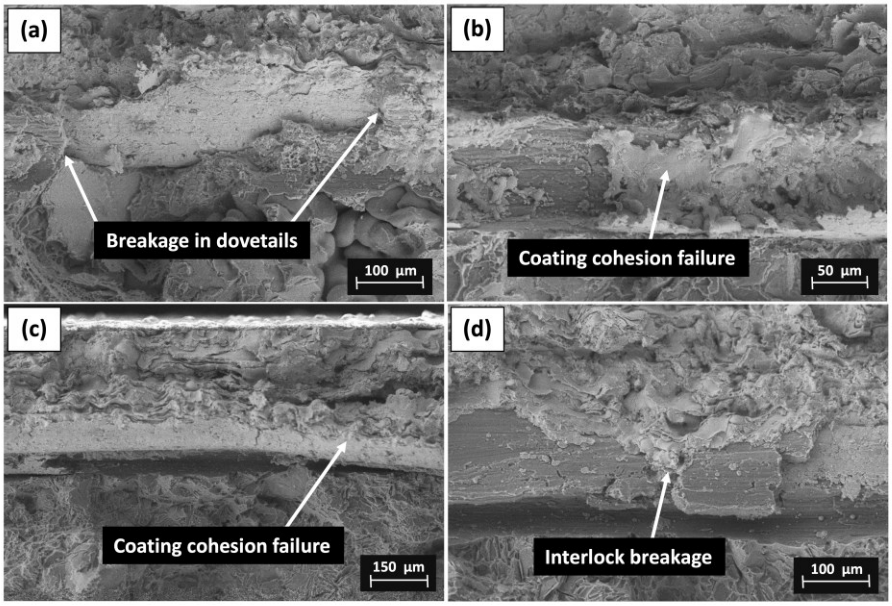

Fig. 59 SEM images of the RT fracture surfaces in the W-orientation showing (a) breakage in the A319-W pattern, (b) coating cohesion failure in A319-W, (c) coating cohesion failure in A356-W, and (d) interlock damage in A356-W specimen.

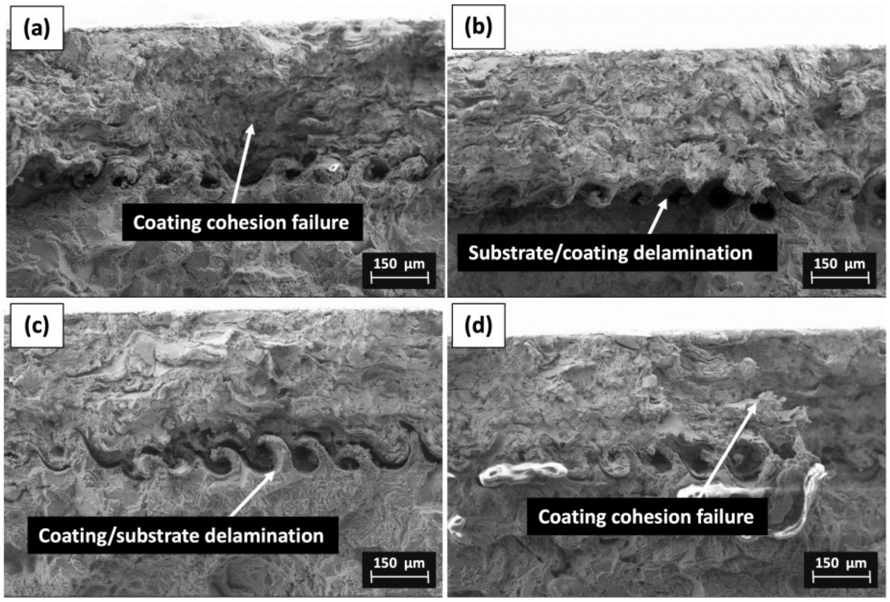

Fig. 60 SEM images of the RT fracture surfaces in the H-orientation showing (a) coating cohesion failure in A319-H, (b) delamination in A319-W, (c) delamination in A356-W, and (d) coating cohesion failure in A356-W specimen.

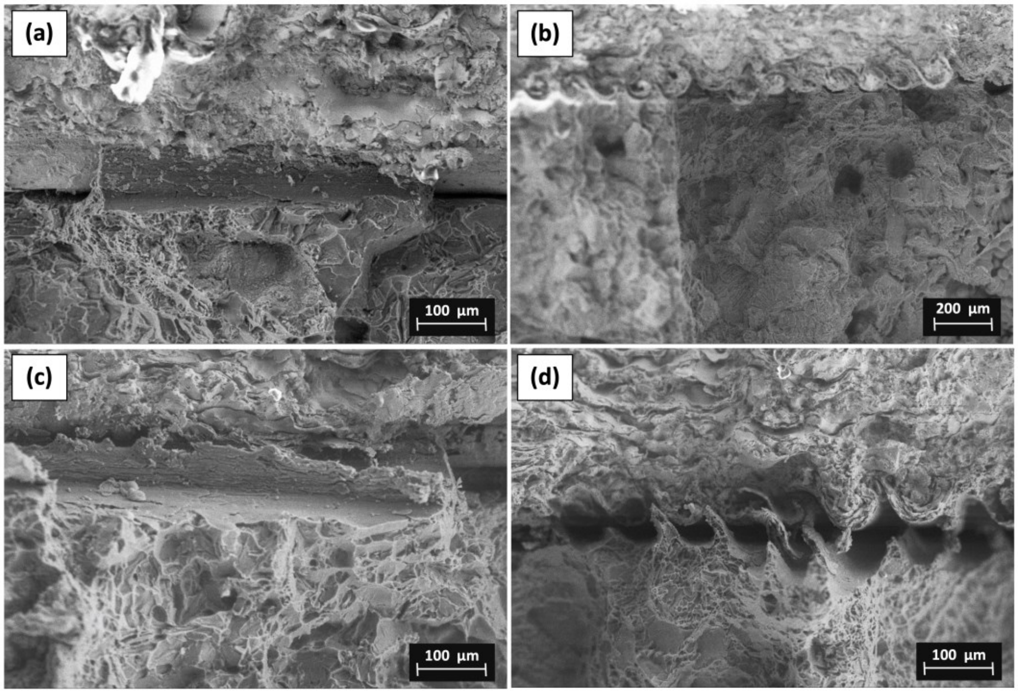

Fig. 61 Fracture surface SEM images of (a) A356-W at 100°C, (b) A356-H at 100°C, (c) A356-W at 250°C, and (d) A356-H at 250°C.

Chapter 7

Fatigue Behaviour and Fracture Mechanisms of PTWA Coating at Room and High Temperatures

7.1 Fatigue Properties

The fatigue properties obtained from cyclic three-point bending tests at RT, 100°C, and 250°C for the four material-orientation combinations (A319-W, A319-H, A356-W, A356-H) are shown in Fig. 62. Fig. 63(a) displays a sample of the uncorrected values where R = 0.1 (black) is plotted with the Morrow (blue) and SWT (red) corrected values where R = 1 for RT tests of A356-W samples. This visually shows the distinct difference between the uncorrected and corrected values, as well as the differences between the mean stress correction methods. When plotted on a log-log scale, the linear relationship between the corrected stress amplitudes and coating life is evident and shown in Fig. 63(b) for A356-W-RT samples. The Basquin parameters $\sigma_f{}'$ and b described by Equation 3 are reported in Table 6 for both methods. Using the corrected two S-N curves from Morrow and SWT methods, the corrected fatigue strength amplitude at 1,000,000 cycles, as predicted by the Basquin curves for each of the twelve sample conditions was obtained and stated in Table 6.

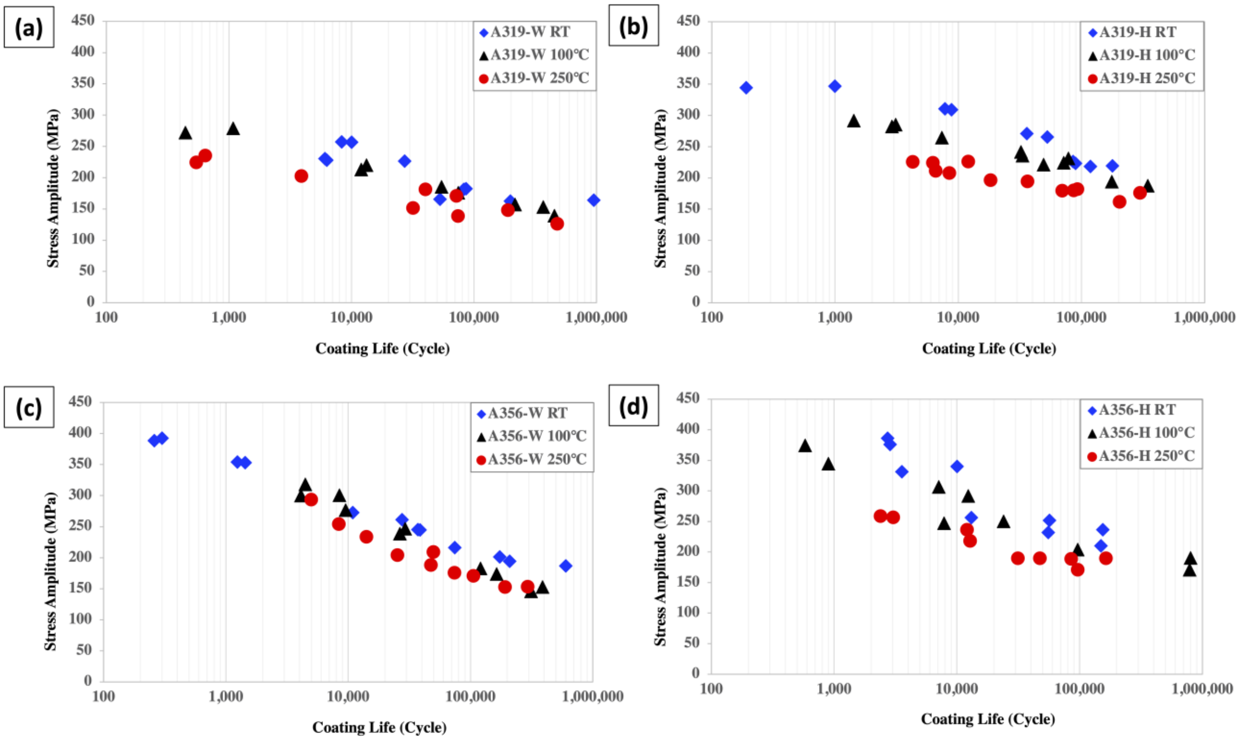

Fig. 62 S-N (stress amplitude and coating life) curves showing the RT, 100°C, and 250°C results for (a) A319-W, (b) A319-H, (c) A356-W, and (d) A356-H.

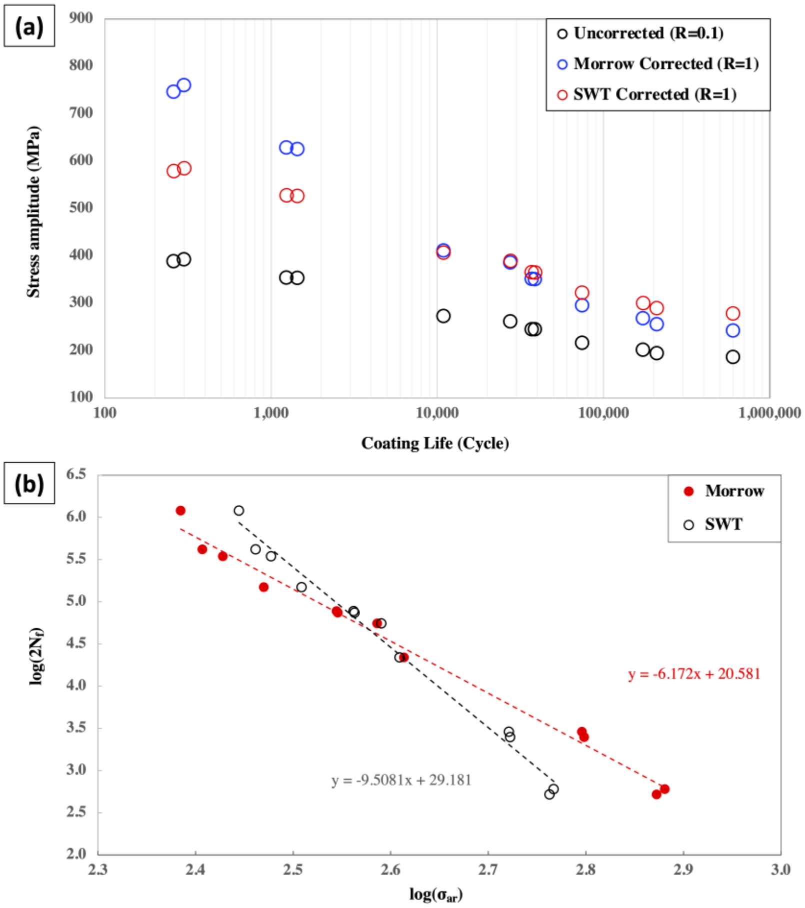

Fig. 63 Plots of A356-W RT sample results showing (a) the S-N (stress amplitude and coating life) curve with uncorrected (R = 0.1) and Morrow/SWT corrected values (R = 1), and (b) the linear relationship between the equivalent stress amplitude for fully reversed loading and coating cycles to failure on a log-log scale for both Morrow and SWT correction methods.

Table 6 Basquin Parameters (Morrow, SWT) from cyclic three-point bending tests

Basquin Property	A319-W			A319-H			A356-W			A356-H		
	RT	100°C	250°C	RT	100°C	250°C	RT	100°C	250°C	RT	100°C	250°C
Morrow: σ_f'	2345.49	1286.29	1774.82	2183.43	1775.92	1884.82	2160.35	6002.33	10109.10	4858.19	2306.93	2288.53
Morrow: b	-0.19	-0.14	-0.17	-0.15	-0.14	-0.15	-0.16	-0.26	-0.30	-0.23	-0.17	-0.18
SWT: σ_f'	1300.57	879.61	713.86	1031.17	890.03	715.44	1172.41	1786.90	1937.10	2035.33	1202.04	985.32
SWT: b	-0.13	-0.10	-0.10	-0.09	-0.08	-0.08	-0.11	-0.15	-0.17	-0.15	-0.11	-0.11
QS Failure Strength[1] [MPa]	841.66	870.84	510.97	846.05	746.47	527.94	991.19	836.10	601.20	1041.47	929.47	668.19
Morrow: Predicted Fatigue Strength Amplitude [MPa]	155.98	162.23	156.69	248.32	237.40	212.34	205.88	146.41	133.62	174.42	207.14	176.42
SWT: Predicted Fatigue Strength Amplitude [MPa]	196.27	200.66	176.28	279.70	260.27	218.75	254.90	197.77	175.74	234.12	250.25	208.63

[1] From quasi-static three-point bending experiments and analysis (Table 5)

The Basquin analysis results in Table 6 are more effective when considered visually. The curve described by the SWT Basquin parameters are plotted in Fig. 64, which shows plots comparing temperature for each of the four substrate-orientation combinations of specimen. The predicted fatigue strength amplitude occurs at the very right of the plot where cycles is at 1,000,000 (runout). The location of each of these curves at runout can be compared to the data points of experimental results that reached runout, which are also plotted. Note that some categories did not yield any runout samples, for example A356-W specimen at all three temperatures). However, in cases where experimental runout data is available, the points occur at a lower stress amplitude value than what is predicted by the corresponding curve. Since the staircase method was not performed to determine experimental fatigue strength, the experimental values that achieved runout have lives that greatly exceed 1,000,000 cycles. There is also a possibility that the fatigue strength predicted by the Basquin curve is more conservative than what was seen in experiment. For example, for the A319-H plot in Fig. 64(b), the 100°C (black) and 250°C (red) curves predict stress amplitudes of 260.27 and 218.75 MPa (Table 6), respectively. The experimental values show 167.80 (black) and 147.49 (red) MPa in

Fig. 64(b) which are 36% and 33% lower. Previous studies in fatigue found the coating to have a higher fatigue resistance at elevated temperatures (i.e., 300°C compared to room temperature) [35]. Based on the RT and 250°C seen in Fig. 64, this may be true for A319-W and A356-H specimen when considering lifespans that exceed 1,000,000. It is possible that the trends seen at 250°C will be further exasperated at 300°C.

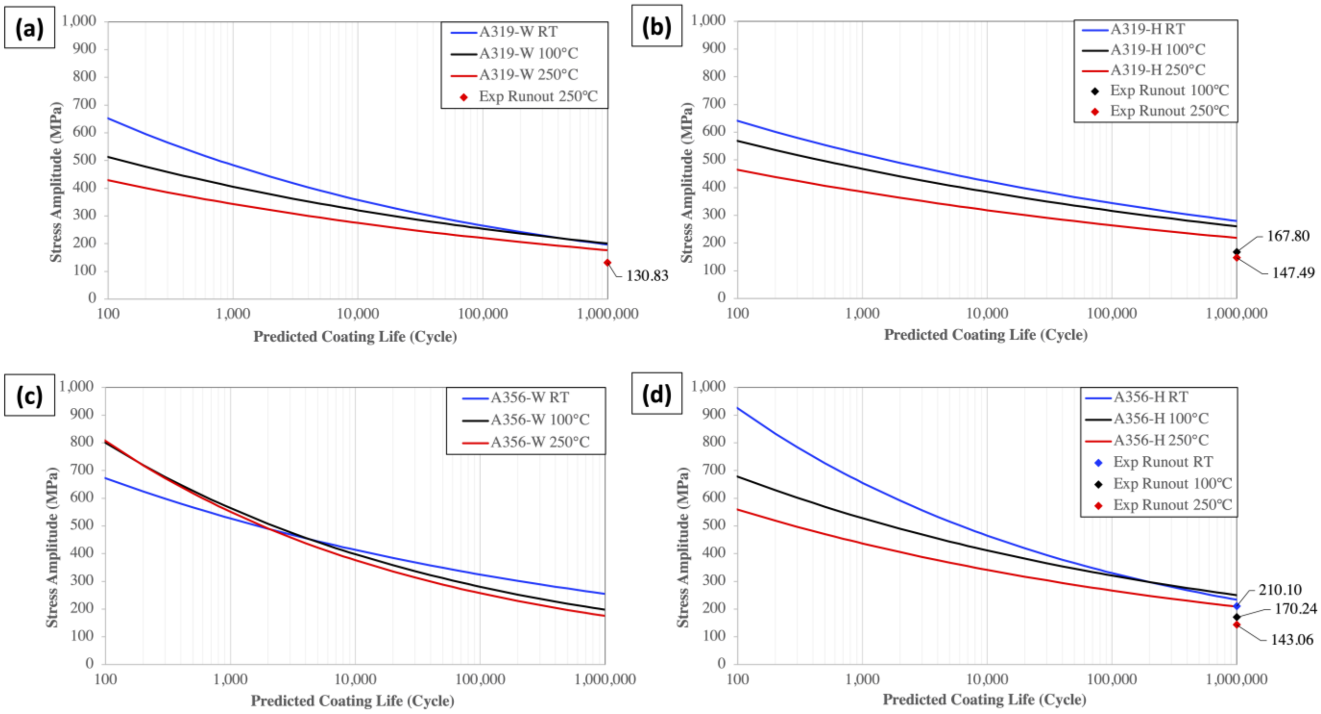

Fig. 64 S-N curves predicted by the Basquin equations showing the RT, 100°C, and 250°C results for (a) A319-W, (b) A319-H, (c) A356-W, and (d) A356-H. Specimen in experimental cyclic tests that reached runout at 1,000,000 cycles are included in the plots.

The three variables involved in analysis include (1) orientation of dovetail rows, (2) material of the substrate, and (3) temperature. To evaluate the effect of orientation, the substrate can be kept constant. Looking at the A319 substrate (Fig. 64(a) and (b)), the W-orientation has lower fatigue strength amplitudes at RT, 100°C, and 240°C (196.27, 200.66, 176.28 MPa) compared to the H-orientation (279.70, 260.27, 218.75 MPa). Note that the SWT correction values are considered for this analysis. W-orientation curves at the various temperatures also see more convergence as high cycles are reached than the H-orientation. Similar is true in the A356 substrate (Fig. 64(c) and (d)) except for A356-W RT results. Overall, the effects of orientation are mainly seen in the higher fatigue strength of the H-orientation samples as well as the slight difference in degree of convergence at high cycles when temperature is varied. This is generally due to the configuration of the rows (acting similarly to grains in wood) being perpendicular to the applied load and maximizing the strength. The friction that exists between the coating and substrate at the interface will also contribute towards the strength in the H-orientation, particularly at elevated temperatures where thermal effects are more prominent. The W-orientation sees less contributions from friction in comparison because breakage does not occur through all the dovetail rows – instead delamination is seen. Notable displacement between the two materials is not observed in the W-orientation like it is in the H-orientation.

To consider the effects of substrate material, the orientation can be kept constant. Comparing the two SWT W-orientation plots (Fig. 64(a) and (c)), the maximum stress at lower cycles of A319 samples is lower than A356 samples. For example, at N = 1,000 cycles, the stress amplitude of A319 samples at RT, 100°C, and 250°C (482.93, 405.55, 343.08 MPa) are lower than the corresponding A356 samples (527.11, 564.03, and 550.94 MPa) using the SWT method. The same is true at higher cycles: at N = 100,000 cycles, the stresses of A319 samples (264.97, 253.70, 220.09 MPa) is also lower than A356 (324.75, 280.47, 257.20 MPa), even with the cross-over of the RT curve in A356-W. The same is true in the H-orientation, where stress amplitude values at low and high cycles are consistently higher in A356 samples. Note that the difference between substrate stress amplitudes is greater at lower cycles than higher cycles. Overall, the A356 substrate is stronger than A319 but the effect of substrate is more prominent at lower cycles. Additionally, as the temperature increases, the difference between A319 and A356 decreases, and the effect of substrate is lessened at elevated temperatures. This falls in line with the previously stated expectation that the A356 may have superior performance at low to intermediate temperatures below 200°C, whereas the A319 may be more stable at higher temperatures but have lower ductility at room temperature. This fatigue study showed that while the superiority of the A356 substrate is most prominent at lower temperatures, even when approaching and briefly exceeding 200°C, the performance of the A356 is still notably better. Since the test temperature range falls within the operating range of the given application, the A356 substrate will perform better than A319 for the operating temperature range of typical consumer vehicle engines.

When considering the effects of temperature, the general trend from Fig. 64 plots show that the strength of the coating decreases with increasing temperature with some exceptions. This trend is also seen in the quasi-static bending study (values shown in Table 6). Like the impact of substrate material, the effects of temperature will be lessened at high cycles and lower stress levels. At higher stress levels that encounter low cycle fatigue, the difference in temperature is most prominent. In the case of A319-W (Fig. 64(a)) and A356-H (Fig. 64(d)), the RT and 100°C results overlap at high cycles where N > 100,000, showing an increase in fatigue strength amplitude from RT to 100°C of 2.19% and 6.45% respectively (SWT values). However, for A319-H and A356-W (Fig. 64(b) and (c)), there was a decrease in fatigue strength amplitude from RT to 100°C of 6.95% and 22.41% respectively. In all four categories, there was a decrease seen from RT to 250°C, which showed changes of A319-W: 10.18%, A319-H: 21.79%, A356-W: 31.06%, and A356-H: 10.89%. Overall, the A319-H and A356-W samples showed consistent decrease in fatigue strength with increasing temperature with A356-W showing the most prominent changes (22.41% to 100°C and 31.06% to 250°C). The increase in fatigue strength amplitude from RT to 100°C seen in A319-H and A356-W samples remain under 7%, which is relatively low. All samples saw a decrease in fatigue strength amplitude from RT to 250°C that exceeded 10%. If RT is assumed to be approximately 20°C, it can be said that the decrease in fatigue properties is most prominent with a more significant temperature change (i.e., RT to 250°C where ΔT = 230°C), whereas a smaller temperature change (i.e., RT to 100°C where ΔT = 80°C) has varying small effects. The decrease in amplitude from 100°C to 250°C in SWT values were more consistent and fell within the 11 to 17% range (A319-W: 12.15%, A319-H: 15.95%, A356-W: 11.14%, and A356-H: 16.63%).

7.2 Fatigue Failure Mechanisms

SEM analysis showed that the failure modes are determined by the orientation and temperature of the sample and has little to do with the substrate type – for that reason, only A356 substrate images are shown for comparison. The region of crack initiation is at the coating/substrate interface, which may be attributed to the poor metallurgical bonding at these regions due to a potential build-up of features such as resolidified particles. The particles are indicative of oxide-rich regions due to the surrounding oxide boundaries. This matches previous findings in literature showing that oxide-rich regions were more prone to fatigue crack initiation in coatings [35].

At 100°C, the mild steel coating structure and properties are not expected to change significantly from RT because it is below the tempering temperature of mild steel. RT to 100°C changes the properties of the substrate which was observed in milder degrees of rupture failure behaviour, interface delamination, and interlock breakage. The differences in temperature are more prominently seen between RT and 250°C test conditions. For both W- and H-orientations, the ductility of the substrate increases substantially with this increase of temperature, indicated by the dimpled fracture surface. The substrate is seen to play a major role in high temperature fatigue where fatigue cracks initiated at the coating/substrate interface and propagated abruptly to the substrate before coating breakage occurred in a rupture-like manner. The fracture path was seen to be more zigzagged for increased temperature. Specific to the W-orientation, the breakage through multiple dovetail rows is more prominent with increasing temperature and severe delamination is greater. Additionally, the randomness of the fatigue fracture path increases with increasing fatigue life cycles which is indicative of more damage.

For consistency, the A356 substrate SEM images of the W-orientation (i.e., no visible wave pattern at the fracture face) of all three temperatures are shown in Fig. 65 (low-cycle fatigue) and Fig. 66 (high-cycle fatigue). These images are constructed by combining several SEM images that span the entire width of the sample. The absence of the wave and direction of loading in this orientation make delamination particularly prominent as well as easy to view. The notable ductility of the substrate, delamination, and breakage across dovetail rows at 250°C is highlighted in Fig. 65(c). Previous bending studies raised the concern of significant Mode II shear from the thermal expansion mismatch between the coating and substrate [34]. This is seen specifically in Fig. 65 – as the temperature increases, the in-plane shear at the fracture surface is more prominent. Significant coating-substrate delamination at 250°C is due to the different thermal expansion properties of the aluminum substrate and steel coating.

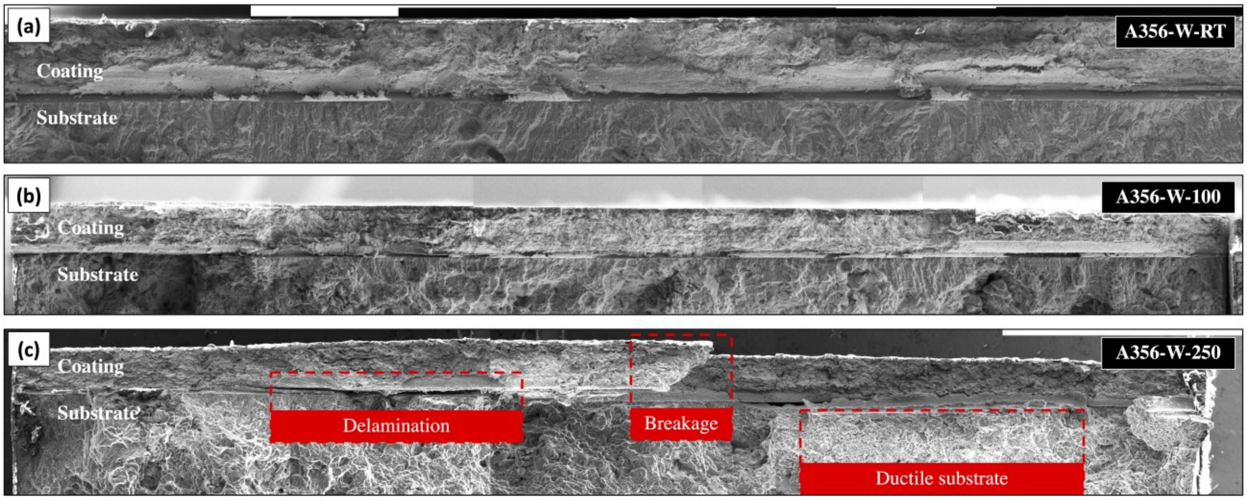

Fig. 65 Low-cycle fracture surface images of A356 substrate samples in the W-orientation at (a) RT (25,600 cycles), (b) 100°C (26,460 cycles), and (c) 250°C (25,300 cycles).

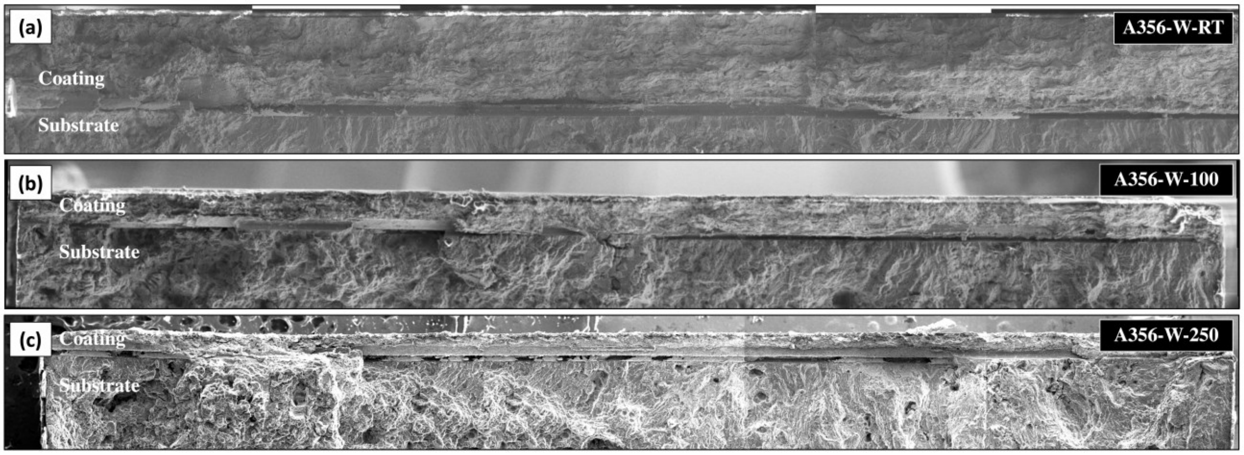

Fig. 66 High-cycle fracture surface images of A356 substrate samples in the W-orientation at (a) RT (209,200 cycles), (b) 100°C (164,000 cycles), and (c) 250°C (192,000 cycles).

SEM of A356 samples in the H-orientation (i.e., visible wave pattern at the fracture face) of all three temperatures are shown in Fig. 67 (low-cycle fatigue) and Fig. 68 (high-cycle fatigue). Due to the loading in this orientation, it makes coating and substrate breakage a more relevant failure mechanism than delamination. Compared to A356-W, the fracture faces are less flat in the H-orientation due to the fracture path not having a clean row to follow. The breakage along varying wave pattern row depths, resulting in a less flat fracture surface, is shown in Fig. 70(b). While breakage through the coating rows does occur in the W-orientation, delamination fracture path follows the straight dovetail rows. It can be seen in Fig. 67(b) (100°C) and Fig. 68(b) (250°C) that large portions of the coating will lift off the coating such that they have different fracture paths in the H-orientation. The mismatched displacement of the coating and substrate is more prevalent at higher temperatures and is also a result of the thermal expansion coefficient mismatch.

It was also noted that deformation and breakage of the interlocking pattern (Fig. 70(a) and Fig. 71(a)) occurs at earlier cycles and that subsequent cycles incur low degrees of further damage. For example, this is seen in the amount of separation seen in low cycle fatigue (7,850 cycles) at 100°C in Fig. 67(b) compared to high cycle fatigue (96,320 cycles) in Fig. 68(b) – the fracture surfaces are very similar. The amount of separation is dependent on the amount of applied load, resulting in either low- or high-cycle fatigue. At higher load levels (low-cycle fatigue), the separation is greater: Fig. 70(a) shows 130 μm of separation at 12,800 cycles (250°C). Lower load levels (high-cycle fatigue), shows comparatively lower separation: Fig. 71(a) shows 120 μm of separation at 163,950 cycles (250°C). The size of the separation gap also increases dramatically with an increase of temperature, which is seen at both low- and high-cycles. Coating/substrate interfacial separation (up to 130 μm) is a prominent failure mechanism in the H-orientation, whereas the W-orientation exhibits very small degrees of separation (10 μm in Fig. 69(a)). On the other hand, the H-orientation does not experience the effects of severe delamination that the W-orientation does.

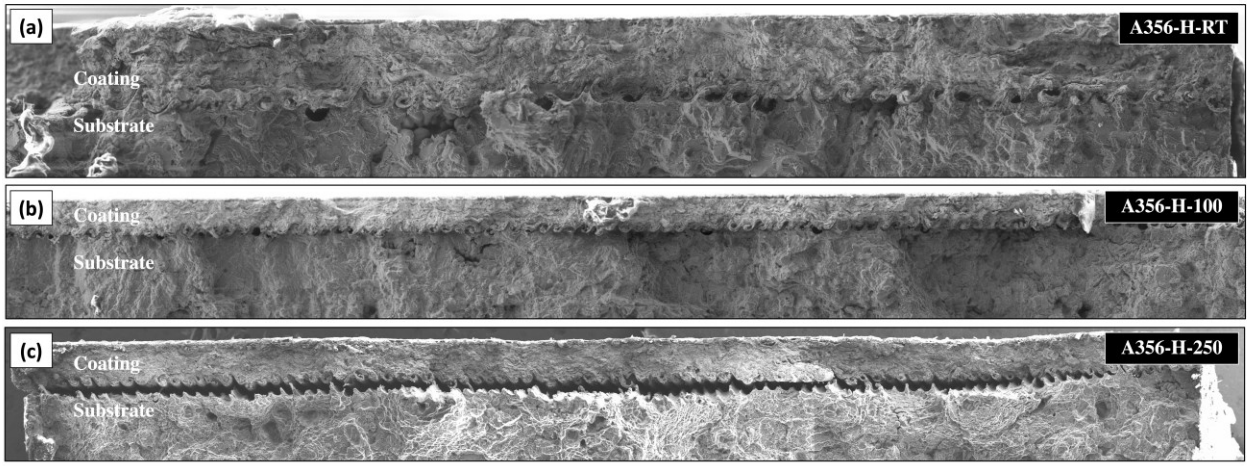

Fig. 67 Low-cycle fracture surface SEM images of A356 substrate samples in the H-orientation at (a) RT (10,050 cycles), (b) 100°C (7,850 cycles), and (c) 250°C (12,800 cycles).

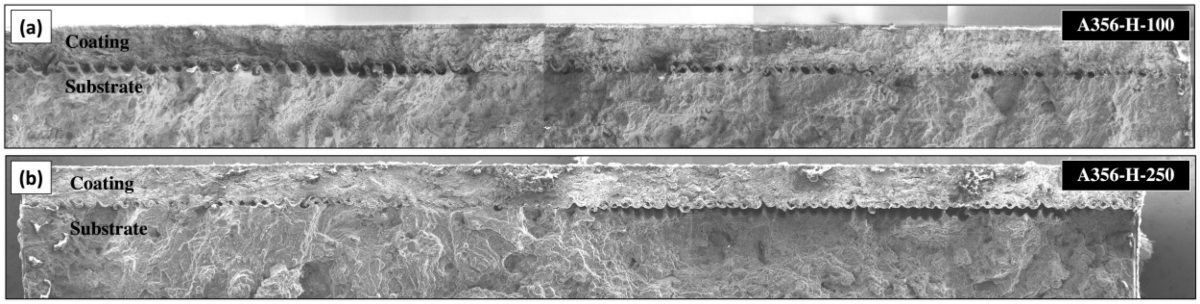

Fig. 68 High-cycle fracture surface SEM images of A356 substrate samples in the H-orientation at (a) 100°C (96,320 cycles) and (b) 250°C (163,950 cycles).

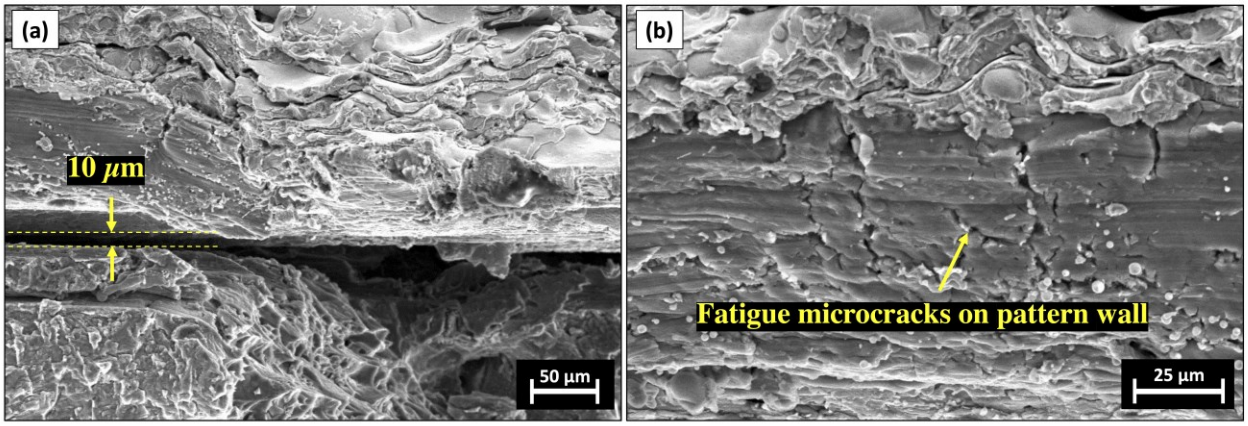

Fig. 69 Close-up SEM images of low-cycle fracture (25,300 cycles) surface of A356 substrate samples in the W-orientation at 250°C showing (a) the degree of coating/substrate interfacial separation, and (b) fatigue microcracks on the wave pattern wall surfaces.

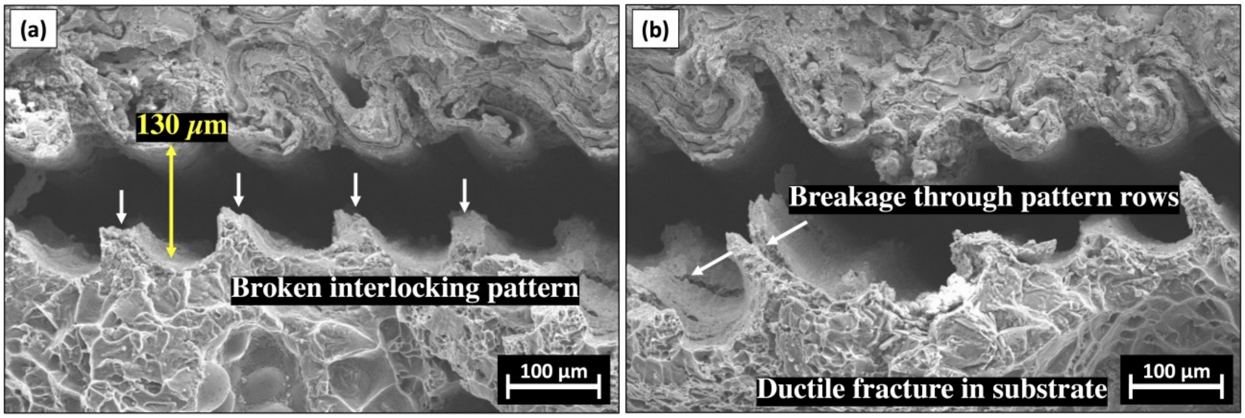

Fig. 70 Close-up SEM images of low-cycle fracture (12,800 cycles) surface of A356 substrate samples in the H-orientation at 250°C showing (a) the degree of coating/substrate interfacial separation and pattern deformation, and (b) breakage through pattern rows and the ductile nature of the substrate.

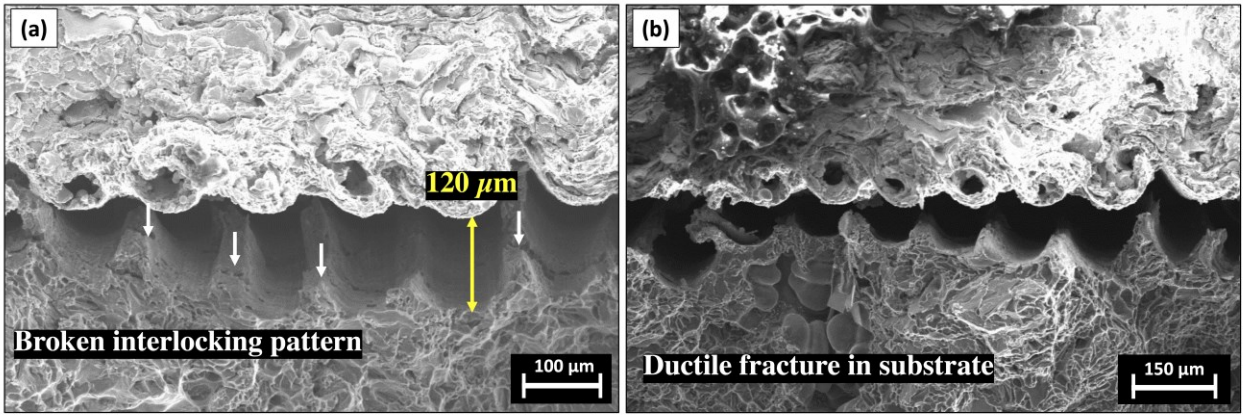

Fig. 71 Close-up SEM images of high-cycle (163,950 cycles) fracture surface of A356 substrate samples in the H-orientation at 250°C showing (a) the degree of coating/substrate interfacial separation and pattern deformation, and (b) the ductile nature of the substrate.

Chapter 8

Conclusions

8.1 Concluding Statements

PTWA sprayed steel coatings were evaluated to address the application towards replacing AlSi cylinder bore liners. The studies conducted served to characterize the microstructure and bonding mechanisms of the coating, substrate, and interface. Quasi-static and cyclic properties, including failure mechanisms, were obtained. The major findings of this work are summarized below.

8.1.1 Microstructural Characterization Conclusions

1. Microstructural studies revealed coating features including coating penetration into the substrate, voids and pores, microcracks, re-solidified particles, and oxides. As-deposited samples showed three regions of varying splat structure with inter-splat oxides. Re-solidified particles made up 2.03% area fraction of the coating and had oxide-rich boundaries. The differing splat arrangements and distribution of re-solidified particles contribute to the failure mechanisms of the coating. No visible intermetallic compounds were identified in the TEM study, indicating the absence of diffusional phase transformation due to the rapid solidification of the deposited coating.
2. Post-processed samples exhibited high compressive residual stress at the coating surface (-600 MPa) which approached zero at the interface, and low tensile stress (< 200 MPa) within the substrate. The lack of RS in as-deposited samples indicates that post-processing, which is necessary for appropriate surface roughness, induces a considerable amount of compressive RS at both the coating's surface and through its depth.
3. Micro-indentation revealed a large hardness deviation, ranging from 150 HV to 700 HV. Precise nano-indentation determined that oxides contributed to high hardness (400-500 HV), while splats had lower hardness (200-300 HV).

8.1.2 Bonding (Adhesion/Cohesion) Property Conclusions

1. Adhesion failure causes little to no coating remnants on the substrate fracture surface and higher severity of substrate interface pattern geometry deformation. Cohesion failure causes varying degrees of coating remnants on the substrate fracture surface and low substrate interface deformation.

2. Samples that experience more adhesion failure (and more substrate deformation) indicate that mechanical interlocking is present but not stronger than the cohesion within the coating. Samples that experience more cohesion failure indicate that interfacial interlocking surpasses bonding within the coat.
3. When failure is more so characterized by adhesion failure, the resulting pull strength is lower. This is seen within each experimental sample type (i.e., D319, W319, W356), as well as when comparing the three types. As a result, failure with higher degrees of cohesion more desirable to achieve higher pull strength.
4. The model shows stress concentrations in regions where breakage, separation, and deformation are expected. Varying degrees of deformation shown in the model are also observed in experimental sample fracture surfaces. Stress concentrations show that the coating and substrate yield at a similar point in the wave model, whereas only substrate yielding is imminent in the dovetail. Experimental results show a combination of coating/substrate breakage in the wave pattern, and mainly substrate yielding in the dovetail, which matches the simulations. Cases where coating experiences yielding can be attributed to the unmodelled geometric irregularities and coating microstructure.
5. The deformation in the wave model is a result of the three main types of fracture paths which are seen in experiment but not depicted by the model due to the lack of coating features included. A sensitivity analysis also shows that the effects of void features are more prominent than resolidified particles. Particles away from the interfacial region also contribute little effect to the initial yielding of the sample.

8.1.3 Quasi-Static Bending Conclusions

1. Three-point bend tests of curved samples extracted from cylinder bores reported a maximum average bending stress of 1480 ± 108 MPa at the coating surface. Stress at the interfaces on the coating-side and substrate-side were found to be 1265 ± 92 MPa and 438 ± 32 MPa, respectively. Crack initiation occurred at the interface sidewall and leads to either complete or partial dovetail wall delamination. This was due to the accumulation of re-solidified particles and implies that limited bonding occurs between the coating and substrate at these sidewalls. Three failure modes were observed involving varying degrees of delamination and breakage within the coating. The mode of failure with more instances of breakage within the

coating and less continuous delamination (Mode C) absorbed more load before fracture, making it the preferred failure mode. As a result, re-solidified particle distribution in the interfacial coating microstructure can cause insufficient bonding and pose issues related to crack initiation and delamination during bending. Breakage within the coating affects the fracture path and is also related to the coating microstructure, specifically the distribution of splats/re-solidified particles and oxides which cause local hardness variations.

2. The effects of substrate generally saw that A356 had higher elastic modulus, yield strength, and strength coefficient than A319 at the corresponding orientation and temperature. A319 strain hardening exponent values were generally higher. This means that the A356 substrate is more resistant to elastic deformation and can withstand higher loads before permanent deformation and failure. This may imply that the bonding of the PTWA coating performs more efficiently on the A356 substrate.
3. The effects of orientation show that the A356 H-orientation has higher elastic modulus and yield strength compared to its W-orientation counterpart. Engineering fracture strain values were lower in the H-orientation at RT and 250°C, whereas strength coefficient values were lower at RT and 100°C. Strain hardening exponent values were also generally lower in the H-orientation. This is ideal, as the H-orientation is the preferred and likely orientation in application to cylinder bores and will consequently be stronger until yield. Past the yield point, the lower strain hardening values in the H-orientation will result in failure strength in both orientations to be similar.
4. An increase of temperature showed a decrease in modulus, strength, and strength coefficient values across all substrate and orientation groups. Similarly, strain hardening exponent values generally decreased with the increase of temperature. Across the board, a decrease in mechanical properties is seen with increasing temperature, meaning that the coating is substantially weakened under these conditions.
5. The operating temperatures of the automotive engine falls within the range of testing considered in this study. Since a considerable decrease in mechanical properties is seen at elevated temperatures, to best accommodate the required conditions, the A356 substrate and H-orientation perform more effectively and may be more appropriate candidates in design when involving PTWA thermal sprayed coatings. Reducing the occurrence of resolidified

particle features within the coating, particularly at the interfacial boundary between the coating and substrate, may delay crack initiation.

6. W-orientation tests at RT showed failure to Mode B, whereas elevated temperatures saw Mode C failure which is characterized by an increase of breakage through the coating with increasing temperature. An increase in breakage at the interface pattern was also observed because of the prominent softening of the substrate material.
7. H-orientation tests saw abrupt cohesive coating breakage dominated by delamination and separation at the interface. The increase in temperature resulted in an increase of the separation due to the differences in thermal expansion of the two materials. The substrate was observed to fail in a ductile manner at elevated temperatures.

8.1.4 Fatigue Bending Conclusions

1. The fatigue strength amplitude predicted by the Basquin parameter curves produce more conservative results than what is seen in runout data from experiments.
2. The W-orientation sees lower fatigue strength as well as slightly more convergence at higher cycles. The A356 substrate material is stronger than A319, though the difference is more prominent at lower cycles and lower temperatures.
3. Fatigue stress amplitude generally decreases with an increase of temperature, though a larger difference is seen from RT to 250°C than RT to 100°C, where increase in stress amplitude was also seen at small degrees.
4. It was seen that the main failure mechanism in the W-orientation was delamination, predominantly following one pattern row, then breakage across multiple rows and the subsequent fracture path following another row. The main failure mechanism in the H-orientation was interface interlocking breakage and consequent separation of the coat and substrate.
5. The increase of temperature is mainly related to delamination: the degree of delamination in the W-orientation increases significantly with increasing temperature due to the thermal coefficient mismatch of the substrate and coating materials. The mismatch is also responsible for the mismatch in fracture path between the coating and substrate in H-orientation samples, as well as the increased degree of separation.

6. H-orientation interface separation and breakage occurs at earlier cycles and subsequent cycles incur low degrees of further damage. Degree of separation is dependent on the amount of applied load, resulting in either low- or high-cycle fatigue. Higher loads result in larger separation (low-cycle) than low loads (high-cycle).
7. The increased ductility of the substrate at elevated temperatures also affects both orientations as it is likely to pull away from the more brittle coating at the interface. This is exhibited by the delamination in the W-orientation and the differing fracture paths of the substrate and coating in the H-orientation.

8.2 Future Research

There are a few investigations that can be considered to further the findings that were found within the scope of this project. For instance, the presence of IMCs was not identified with the TEM study performed (Section 4.2 Interface Characterization), but signs of its existence were detected using EDX in pull testing where adhesion failure occurred (Fig. 40). TEM study images (i.e. Fig. 27) show that the scale of the investigation was within the hundred-nanometer range, but there is the possibility that IMCs cannot be identified at such a scale. Further TEM studies can be performed to investigate the presence of IMCs by reducing the range by a factor of ten such that the scale falls within a few tens of nanometers.

The wear performance of the coating under cyclic loading is extremely relevant to the piston action during engine bore operation. Fretting fatigue testing will provide an area contact with normal slip friction force to exam the local fatigue behaviour of the coating. ASTM E2789 can be followed to perform these tests under lubricated conditions. The results can be compared to the bending fatigue testing in the relevant temperature and orientation (i.e., RT, W-orientation), but preliminary tensile fatigue testing can be performed to quantify the effects of fretting on fatigue strength reduction and failure mechanisms. The fretting behaviour can also be correlated with the findings from the microstructural analysis to determine the effects of coating features and the coating surface roughness.

Other coating technologies, especially the fast-growing cold spray (CS) technology with similar mechanical interlocking adhesion properties, can be considered for comparison. The advantages of CS make it a viable candidate for consideration: it is a solid-state process with no need for surface activation, high throughput, and is a green coating technology [50]. It is suggested that an initial study, like the flat specimen studies of this work be performed of similar samples coated by CS and compared with the PTWA. Similar characterization studies featuring zinc coatings on AZ31B have been conducted to investigate the effects of single/multi-layer CS coatings [51]. Parametric studies have also targeted the topic of residual stress within the substrate during CS deposition [52]. Fatigue life for AA7075 CS coatings on AZ31B cast alloy have been studied to determine the cyclic properties of such coatings [38]. The work outlined in these studies can be considered for CS technology development towards the engine bore application.

Letter of Copyright Permission

The following is included in Elsevier copyright permissions policies:

> Authors can include their articles in full or in part in a thesis or dissertation for non-commercial purposes. No written permission from Elsevier is necessary. This right extends to the posting of your thesis to your university's repository provided that if you include the published journal article, it is embedded and not separately downloadable.

References

[1] Corporate Average Fuel Economy (CAFE) Standards, (2018).

[2] Greenhouse Gas Sources and Sinks in Canada, Natl. Invent. Rep. Greenh. Gas Sources Sink. Canada. (2018).

[3] G.F. Bolling, J. Cisse, Aluminum silicon alloys, 3,895,941, 1975.

[4] K. Bobzin, F. Ernst, K. Richardt, T. Schlaefer, C. Verpoort, G. Flores, Thermal spraying of cylinder bores with the Plasma Transferred Wire Arc process, Surf. Coatings Technol. 202 (2008) 4438–4443.

[5] J. Lenny, Replacing the Cast Iron Liners for Aluminum Engine Cylinder Blocks: A Comparative Assessment of Potential Candidates, 2011.

[6] G. et al. Wuest, The Key Advantages of the Plasma-Powder Spray Process for the Thermal Spray Coating of ylinder Bores in Automotive Industry, in: SAE Int. Congr. Expo., n.d.: pp. 33–43.

[7] K. Bobzin, F. Ernst, J. Zwick, T. Schlaefer, D. Cook, K. Kowalsky, K. Bird, D.H. Gerke, R.E. Sharp, K.R. Raab, S. Lindon, Thermal Spraying of Cylinder Bores With the PTWA Internal Coating System, in: ASME 2007 Intern. Combust. Engine Div. Fall Tech. Conf., ASME, 2007: pp. 697–704.

[8] Automotive Parts Remanufacturers Association: APRA, Remanufacturing as best practice of the Circular Economy, (2015) 1–2.

[9] J. Zou, Characterization of thermal spray coatings on aluminum engine bore, Mech. Adv. Testing, Surf. (2010) 1–4.

[10] G. Barbezat, Advanced thermal spray technology and coating for lightweight engine blocks for the automotive industry, Surf. Coatings Technol. 200 (2005) 1990–1993.

[11] J.B. K. Kowalsky, D. Marantz, D. Cook, Plasma transferred wire arc thermal spray apparatus and method (PTWA), 5.808.270, 1998.

[12] W. Guo, J. Zhang, Y. Wu, S. Hong, Y. Qin, Fabrication and characterization of Fe-based amorphous coatings prepared by high-velocity arc spraying, Mater. Des. 78 (2015) 118–124.

[13] G. Darut, H. Liao, C. Coddet, J.M. Bordes, M. Diaby, Steel coating application for engine

block bores by Plasma Transferred Wire Arc spraying process, Surf. Coatings Technol. 268 (2015) 115–122.

[14] V. Fachbereich Maschinenbau, V. Dipl-Ing Thorsten Kuhn, Measuring the Distortion of Cylinders in Aluminum Diesel Engine Blocks, Hannover University, 2001.

[15] B. Gérard, Application of thermal spraying in the automobile industry, Surf. Coatings Technol. 201 (2006) 2028–2031.

[16] H.-W. Hoffmeister, A.C. Schnell, Mechanical roughing of cylinder bores in light metal crankcases, (n.d.).

[17] H. Liborius, G. Paczkowski, A. Nestler, T. Grund, A. Schubert, T. Lampke, Influence of dovetail microstructures on adhesive tensile strength and morphology of thermally sprayed metal coatings, Procedia CIRP. 71 (2018) 299–304.

[18] D.A. Stephenson, Interpolated Selective Area Mechanical Roughening for Thermally Sprayed Engine Bores, SAE Int. J. Mater. Manuf. 10 (2017) 13–18.

[19] M. Hahn, R. Theissmann, B. Gleising, W. Dudzinski, A. Fischer, Microstructural alterations within thermal spray coatings during highly loaded diesel engine tests, Wear. 267 (2009) 916–924.

[20] G. Barbezat, Thermal spray coatings for tribological applications in the automotive industry, Proc. 2006 Int. Therm. Spray Conf. ASM Int. (2006).

[21] X.B. Zhao, Z.H. Ye, Microstructure and wear resistance of molybdenum based amorphous nanocrystalline alloy coating fabricated by atmospheric plasma spraying, (2013).

[22] S. Sampath, X.Y. Jiang, J. Matejicek, A.C. Leger, A. Vardelle, Substrate temperature effects on splat formation, microstructure development and properties of plasma sprayed coatings Part I: Case study for partially stabilized zirconia, 1999.

[23] L. Gao, H. Guo, L. Wei, C. Li, H. Xu, Microstructure, thermal conductivity and thermal cycling behavior of thermal barrier coatings prepared by plasma spray physical vapor deposition, Surf. Coatings Technol. 276 (2015) 424–430.

[24] B. Rajasekaran, S. Ganesh Sundara Raman, S. V. Joshi, G. Sundararajan, Effect of microarc oxidised layer thickness on plain fatigue and fretting fatigue behaviour of Al-Mg-Si alloy, Int.

J. Fatigue. 30 (2008) 1259–1266.

[25] M. Javidani, D. Larouche, Application of cast Al–Si alloys in internal combustion engine components, Int. Mater. Rev. 59 (2014) 132–158.

[26] P.L. Fauchais, J.V.R. Heberlein, M.I. Boulos, Thermal Spray Fundamentals, Springer US, Boston, MA, 2014.

[27] A. Edrisy, A.T. Alpas, Microstructures and sliding wear resistances of 0.2% carbon steel coatings deposited by HVOF and PTWA thermal spray processes, Thin Solid Films. 420–421 (2002) 338–344.

[28] R.H.U. Khan, A.L. Yerokhin, T. Pilkington, A. Leyland, A. Matthews, Residual stresses in plasma electrolytic oxidation coatings on Al alloy produced by pulsed unipolar current, (2005).

[29] R.T.R. McGrann, D.J. Greving, J.R. Shadley, E.F. Rybicki, T.L. Kruecke, B.E. Bodger, The effect of coating residual stress on the fatigue life of thermal spray-coated steel and aluminum, Surf. Coatings Technol. 108–109 (1998) 59–64.

[30] I.K. E Lugschedier, Thermal barrier coatings: powder spray process and coating technology, in: Mater. Eng. No. 13, 1999: pp. 267–306.

[31] B. Rajasekaran, S. Ganesh Sundara Raman, S. V. Joshi, G. Sundararajan, Effect of grinding on plain fatigue and fretting fatigue behaviour of detonation gun sprayed Cu-Ni-In coating on Al-Mg-Si alloy, Int. J. Fatigue. 31 (2009) 791–796.

[32] P. Sharma, J.D. Majumdar, Surface characterization and mechanical properties' evaluation of boride-dispersed nickel-based coatings deposited on copper through thermal spray routes, J. Therm. Spray Technol. 21 (2012) 800–809.

[33] C.J. Li, G.J. Yang, C.X. Li, Development of particle interface bonding in thermal spray coatings: A review, J. Therm. Spray Technol. 22 (2013) 192–206.

[34] P.S.M.G. P. Abachi, T.W. Coyle, Plasma Spraying of 316 Stainless Steel on Aluminum and Investigation of Coat/Substrate Interface, 10 (2016) 536–546.

[35] P.L. Liu, J.K. Shang, O.O. Popoola, Fatigue behavior of a thermally sprayed low carbon steel coating, Mater. Sci. Eng. A. 277 (2000) 176–182.

[36] S. Dallaire, Influence of Temperature on Bonding Mechanism of Plasma-Sprayed Coatings, (1982) 237–244.

[37] P.S.M.G. P. Abachi, T.W. Coyle, P. Abachi, T.W. Coyle, P.S.M. Gharavi, Plasma Spraying of 316 Stainless Steel on Aluminum and Investigation of Coat/Substrate Interface, Int. J. Mater. Metall. Eng. 10 (2016) 536–546.

[38] S.B. Dayani, S.K. Shaha, R. Ghelichi, J.F. Wang, H. Jahed, The impact of AA7075 cold spray coating on the fatigue life of AZ31B cast alloy, Surf. Coatings Technol. 337 (2018) 150–158.

[39] J.A.M. de Camargo, H.J. Cornelis, V.M.O.H. Cioffi, M.Y.P. Costa, Coating residual stress effects on fatigue performance of 7050-T7451 aluminum alloy, Surf. Coatings Technol. 201 (2007) 9448–9455.

[40] B. Rajasekaran, S. Ganesh Sundara Raman, S. V. Joshi, G. Sundararajan, Influence of detonation gun sprayed alumina coating on AA 6063 samples under cyclic loading with and without fretting, Tribol. Int. 41 (2008) 315–322.

[41] R. Alani, Ion beam milling system and method for electron microscopy specimen preparation (Patent), Google Patents, 2004.

[42] TWO-DIMENSIONAL X-RAY DIFFRACTION, 2018.

[43] D.D. Fuller, Theory and practice of lubrication for engineers, John Wiley and Sons, New York, 1966.

[44] J.T. DeWolf, D. Mazurek, F.P. Beer, E.R. Johnston, Mechanics of Materials, 8th ed., McGraw-Hill Education, 2019.

[45] J. Zhang, D.C. Saha, H. Jahed, Microstructure and mechanical properties of plasma transferred wire arc spray coating on aluminum cylinder bores, Surf. Coatings Technol. 426 (2021) 127757.

[46] P. Fauchais, A. Vardelle, B. Dussoubs, Quo Vadis thermal spraying?, J. Therm. Spray Technol. (2001).

[47] G. Espie, A. Denoirjean, P. Fauchais, J.C. Labbe, J. Dubsky, O. Schneeweiss, K. Volenik, In-flight oxidation of iron particles sprayed using gas and water stabilized plasma torch, Surf. Coatings Technol. (2005).

[48] F. Fanicchia, X. Maeder, J. Ast, A.A. Taylor, Y. Guo, M.N. Polyakov, J. Michler, D.A. Axinte, Residual stress and adhesion of thermal spray coatings: Microscopic view by solidification and crystallisation analysis in the epitaxial CoNiCrAlY single splat, Mater. Des. 153 (2018) 36–46.

[49] S. Kuroda, T.W. Clyne, The quenching stress in thermally sprayed coatings, Thin Solid Films. 200 (1991) 49–66.

[50] J. Villafuerte, Modern Cold Spray: materials, process, and applications, Cham : Springer, 2015.

[51] B. Marzbanrad, E. Toyserkani, H. Jahed, Characterization of single- and multilayer cold-spray coating of Zn on AZ31B, Surf. Coatings Technol. 416 (2021) 127155.

[52] B. Marzbanrad, H. Jahed, E. Toyserkani, On the evolution of substrate's residual stress during cold spray process: A parametric study, Mater. Des. 138 (2018) 90–102.

Appendix A

Anton Paar Data

Note that due to the unsatisfactory accuracy of indentation at the "interfacial region", only the results for the coating and substrate regions were considered during analysis.

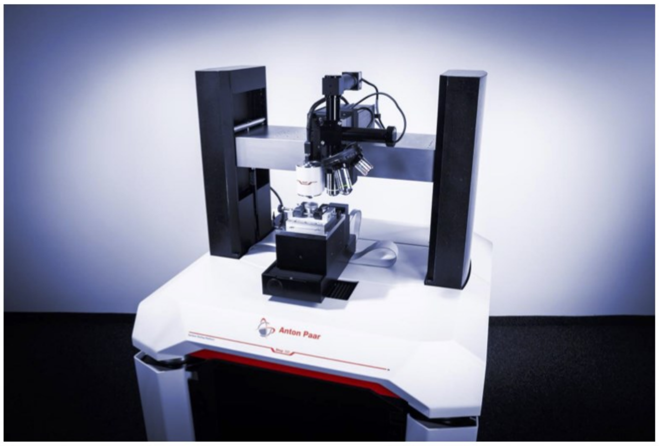

Anton Paar

Method : **Nanoindentation Tester (NHT^3)**
Related to ISO 14577

Indenter Type	Sphéro-conical	
Indenter Radius	20	[µm]
Loading Type	Sinus	
Maximum Load	100	[mN]
Pause at Max Load	10	[s]
Loading/Unloading Rate	200	[mN/min]
Sinus Frequency	5	[Hz]
Sinus Max Amplitude	10	[mN]

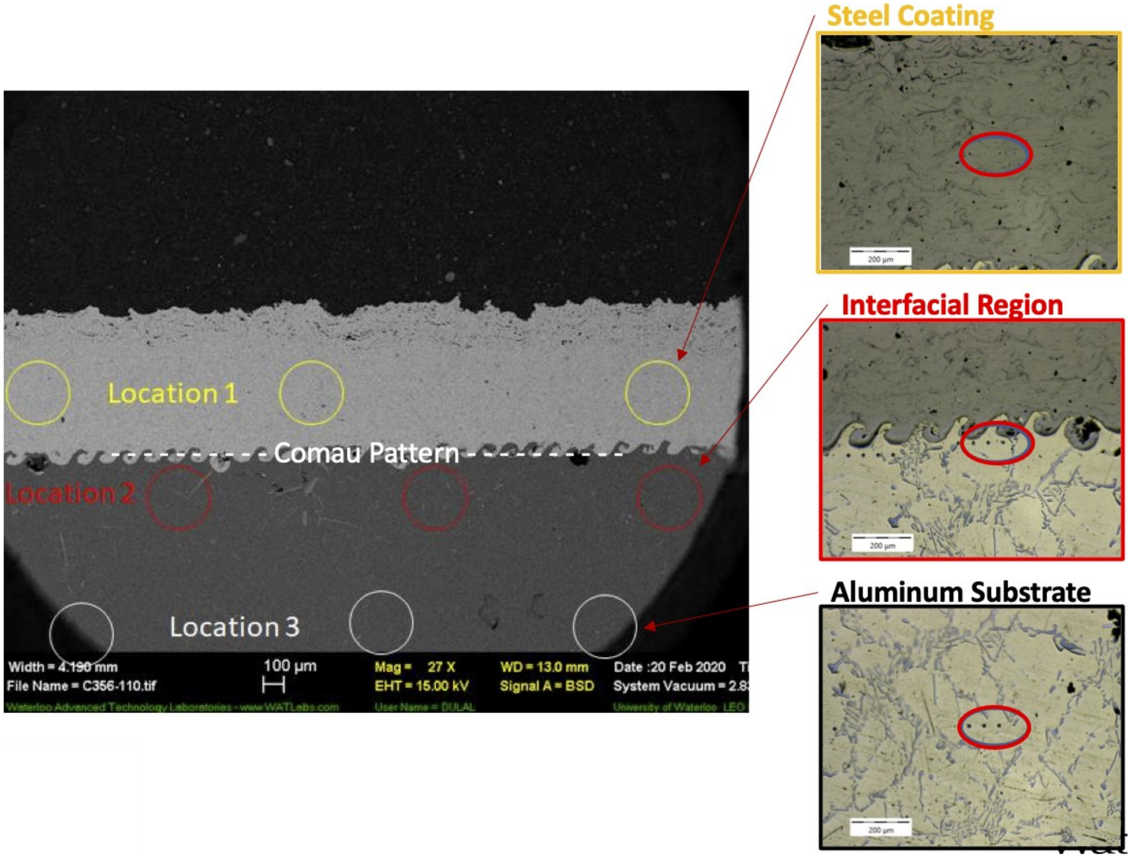

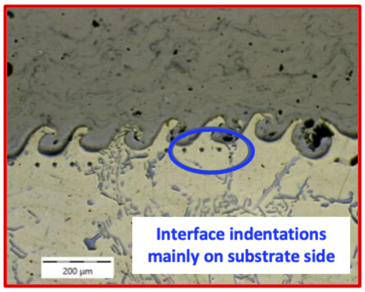

Sample 1

ANTON PAAR				
	E [GPa]	Stdev	YS [MPa]	Stdev
Substrate	**91.817**	**1.50**	**285.0366667**	**60.69**
Interface	92.094	4.19	270.155	5.30
Coating	**126.2325**	**23.94**	**773.2475**	**142.34**

BULK PROPERTIES		
	E [GPa]	YS [MPa]
Substrate	**73.8**	**153.5**
4130 Steel	205	435

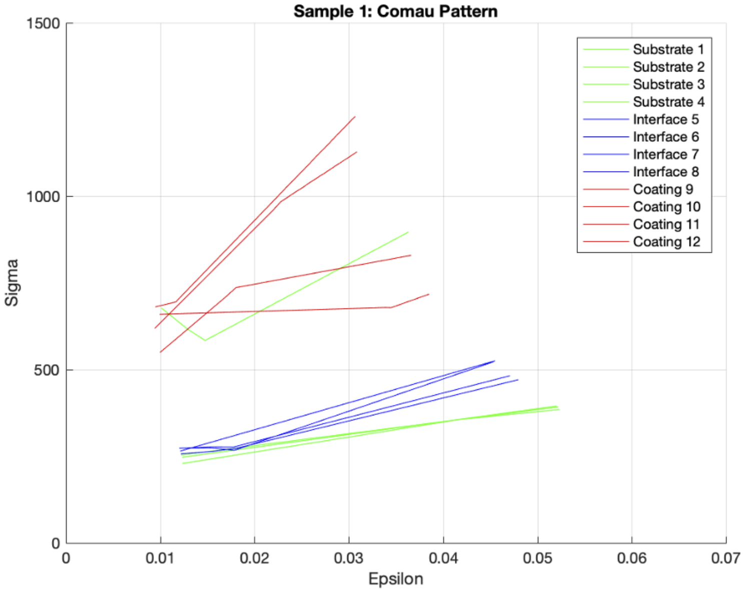

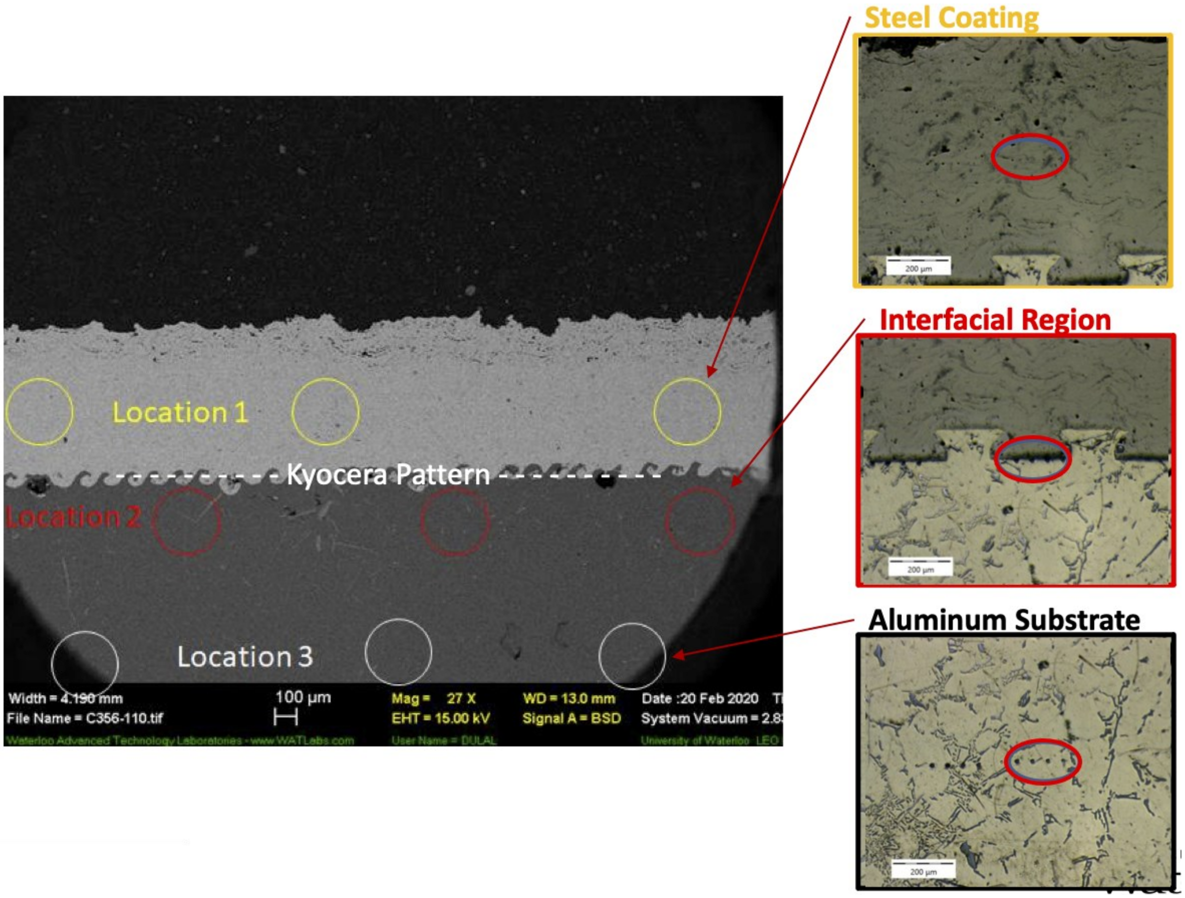

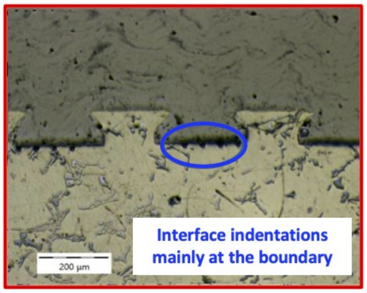

Sample 2

ANTON PAAR				
	E [GPa]	**Stdev**	**YS [MPa]**	**Stdev**
Substrate	**87.9545**	**0.97**	**358.0875**	**72.76**
Interface	73.5915	4.10	266.5825	50.89
Coating	**124.365**	**19.41**	**797.7075**	**232.52**

BULK PROPERTIES		
	E [GPa]	**YS [MPa]**
Substrate	**73.8**	**153.5**
4130 Steel	205	435